NASA/TM—2001–209982

In Situ Aerosol Optical Thickness Collected by the SIMBIOS Program (1997–2000): Protocols, and Data QC and Analysis

Giulietta S. Fargion and Robert Barnes
SAIC General Sciences Corp., Beltsville, Maryland

Charles McClain
NASA Goddard Space Flight Center, Greenbelt, Maryland

National Aeronautics and
Space Administration

Goddard Space Flight Center
Greenbelt, Maryland 20771

March 2001

Available from:

NASA Center for AeroSpace Information
7121 Standard Drive
Hanover, MD 21076-1320
Price Code: A17

National Technical Information Service
5285 Port Royal Road
Springfield, VA 22161
Price Code: A10

Preface

The purpose of this technical report is to provide current documentation of the Sensor Intercomparison and Merger for Biological and Interdisciplinary Oceanic Studies (SIMBIOS) Project Office activities on *in situ* aerosol optical thickness (i.e., protocols, data QC and analysis). This documentation is necessary to ensure that critical information is related to the scientific community and NASA management. This critical information includes the technical difficulties and challenges of validating and combining ocean color data from an array of independent satellite systems to form consistent and accurate global bio-optical time series products. This technical report is not meant as a substitute for scientific literature. Instead, it will provide a ready and responsive vehicle for the multitude of technical reports issued by an operational project.

Table of Contents and Author List

(2)/-12/12/48

Chapter 1

SIMBIOS Sun Photometer Program

Charles R. McClain[1] and Giulietta S. Fargion[2]

[1]*NASA, Goddard Space Flight Center, Greenbelt, Maryland*

[2]*SAIC General Sciences Corporation, Beltsville, Maryland*

1.1 INTRODUCTION

Aerosol optical thickness (AOT) values determined from the satellite ocean color data provide useful information on the spatial and temporal distributions of aerosols and are by-products of the atmospheric corrections required to estimation of water-leaving radiances. The SIMBIOS Project is using *in situ* atmospheric data, primarily from sun photometers, for several purposes including:

1. validation the SeaWiFS and other ocean color mission aerosol optical products, e.g., AOT and Ångström exponent, as in (Wang et al., 2000),

2. evaluation of the aerosol models currently used for atmospheric corrections, e.g., Gordon and Wang (1994), and

3. development of vicarious sensor calibration methodologies, e.g., Evans and Gordon (1994), especially for the near-infrared bands where in-situ water-leaving radiance data in the visible from sites like the Marine Optical Buoy (MOBY: Clark et al., 1997) cannot be used.

The principal source of *in situ* aerosol observations was the Aerosol Robotic Network (AERONET). AERONET is a network of ground-based automated sun photometers owned by national agencies and universities (Holben et al. 1998). AERONET data provides globally distributed, near-real time observations of aerosol spectral optical depths, aerosol size distributions, and precipitable water. Because the majority of the AERONET stations are at continental locations, SIMBIOS augmented the network with 12 additional island and coastal sites, including the Hawaiian Islands (Lanai and Oahu), Ascension Island, Bahrain, Tahiti, Wallops Island (mid-Atlantic U.S. east coast), South Korea, Turkey, Argentina, Azores and Australia (Perth). Deploying instruments in foreign locations usually requires a memorandum of understanding between NASA and the institution tending the instrument, a process that can take many months. The SIMBIOS Project has invested considerable effort in modifying the CIMEL system to be more durable for extended deployments in marine environments.

The SIMBIOS Project also has a number of other sun photometers including hand-held MicroTops, ship-stablilized PREDE's, and SIMBAD/SIMBADA radiometers. The SIMBAD/SIMBADA radiometers collect optical thickness data as part of the surface reflectance measurement. The Project also has a micropulse lidar which can be deployed on a vessel that provides information on the vertical distribution of aerosols. The lidar custodian is Dr. Jim Spinhirne, the instrument designer, at GSFC who operates a network of lidar sites. The radiometers are calibrated in collaboration with the AERONET Program which maintains an open-air calibration facility and a sphere calibration laboratory at NASA Goddard Space Flight Center (GSFC). The calibration capability includes a French-built polarization adapter for the integrating sphere for calibration of polarized bands in some CIMEL instruments. The shipboard instruments are available to U.S. SIMBIOS investigators during research expeditions.

The purpose of this technical memorandum is to summarize the end-to-end sun photometer data processing and analysis. This includes data acquisition, calibration, quality control, and match-up comparisons with satellite data. These analyses have been standardized across the various types of radiometers and also includes analysis of shadow-band radiometer data provided by Dr. Mark Miller of the Brookhaven National Laboratory (BNL).

REFERENCES

Clark, D., H. R. Gordon, K. J. Voss, Y. Ge, W. Broenkow, and C. Trees, 1997: Validation of atmospheric correction over the oceans, J. Geophys. Res., 102, 17,209-17217.

Evans, R. H. and H. R. Gordon 1994: CZCS "system calibration": A retrospective examination, *J.* Geophys.Res., 99(C4), 7293-7307.

Gordon, H.R. and M. Wang, 1994: Retrieval of water-leaving radiance and aerosol optical thickness over the oceans with SeaWiFS: A preliminary algorithm, Appl. Opt., 33, 443-452.

Holben, B.N., T.F. Eck, I. Slutsker, D. Tanre, J.P. Buis, A. Setzer, E. Vermote, J.A. Reagan, Y.J. Kaufman, T. Nakajima, F. Leaven, I. Jankowiak, and A. Smirnov, 1998: AERONET – a federated instrument network and data archive for aerosol characterization. Remote Sens. Environ., 66, 1-16.

Wang, M., S. W. Bailey, C. M. Pietras, and C. R. McClain, 2000: SeaWiFS aerosol optical thickness match-up analyses, In SeaWiFS Postlaunch Calibration and Validation Analyses, Part 2, NASA/TM-2000-206892, Vol. 10., S. B. Hooker and E. R. Firestone (eds.), NASA Goddard Space Flight Center, Greenbelt, Maryland, 39-44.

(2) / TM / M / 35

Chapter 2

Characteristics of the SIMBIOS Atmospheric Instruments

Christophe Pietras[1], Mark Miller[2], Robert Frouin[3], Ellsworth J. Welton[4], & Ilya Slutsker[5]

[1]*SAIC General Sciences Corporation, Beltsville, Maryland*

[2]*Department Environmental Science, Earth System Science Division, Brookhaven National Laboratory, Upton, New York*

[3]*Scripps Institution of Oceanography, University of California, San Diego, California*

[4]*GESTC, University of Maryland Baltimore County, Baltimore, Maryland*

[5]*Science Systems and Applications, Inc., Lanham, Maryland*

2.1 INTRODUCTION

The SIMBIOS pool of instruments is composed of three types of equipment. These instruments are used by the SIMBIOS Project and the SIMBIOS Science Team to enhance the overall quality of atmospheric aerosol validation data sets provided to the SeaBASS archive. The first type is composed of sun/sky photometers that measure the solar irradiance and the sky radiance. The second type is the shadow-band radiometer that measures the diffuse and global (upper hemispheric) sky radiance. The third type is the Micropulse Lidar (MPL), which measures the vertical and horizontal distribution of aerosol backscatter, extinction, and optical depth. The photometers and radiometers generally have several channels, with center wavelengths from 0.3 μm to 1.0 μm and with narrow bandwidths (0.01μm). Their characteristics are briefly summarized in Table 2.1. The instruments are deployed by SIMBIOS or NASA Principal Investigators on cruises and provide data to the SeaBASS archive for SIMBIOS ocean color validation research. Deployment policy and procedures are available on the SIMBIOS home page (http:// simbios.gsfc.nasa.gov). This chapter reviews each type of instrument, its characteristics, and its advantages for the project. A description of the protocols for the operation of these instruments and for their data analysis is given in Chapter 3.

2.2 HAND-HELD SUN PHOTOMETERS AND RADIOMETERS

Hand-held sun photometers are the simplest and the most cost-effective instruments to measure aerosol optical thickness. They are highly appreciated for their portability, their low cost, and their ease of use (Figure 2.1). The SIMBIOS Program maintains a pool of twelve MicroTops sun photometers, manufactured by Solar Light, Inc. (Morys, 1998), and three SIMBAD instruments (one SIMBAD and two SIMBADA), built by the University of Lille (Deschamps, 2000). The acronym for SIMBAD translates from the French as: Satellite Validation for Marine Biology and Aerosol Determination. The SIMBAD instruments can be used to measure the upwelling radiances from the ocean, as well as the solar irradiance and the sky radiance. These hand-held sun photometers are used during ocean-color evaluation cruises to provide aerosol optical thickness measurements for comparison with values derived from satellite algorithms. The MicroTops and SIMBAD instruments have five channels, with center wavelengths between 0.4 μm and 1.0 μm, according to specifications given by the World Meteorological Organization. The center wavelengths and bandwidths for the instrument are given in Table 2.2. The optics of the SIMBAD instruments are fitted with a polarizer to reduce reflected skylight when the instrument is operated in its ocean-viewing mode (Fougnie et al., 1999). Both the MicroTops and SIMBAD instruments use photodiode detectors and interference filters. Collimators mounted in front of the optics allow a 2.5° full field of view for the MicroTops and a 3° full field-of-view for SIMBAD. Auxiliary pressure and temperature are provided by the instruments, and Global Positioning Sensors are used to obtain the position and time. Dark count measurements are made by the MicroTops, using a cover for the optics, and by the SIMBAD, using a specific dark count mode. The dark counts allow corrections for instrument temperature effects. The measurement frequency for both instruments is 10 Hz. The highest intensities measured are stored and used to

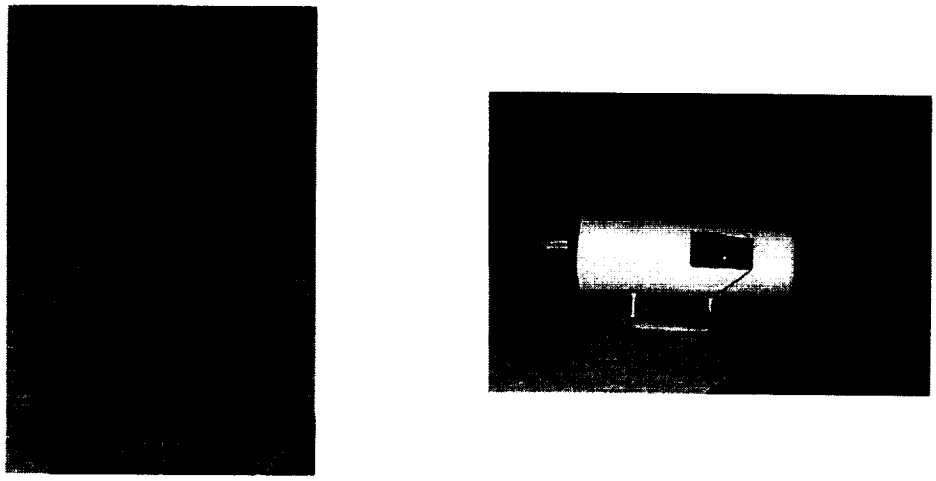

Figure 2.1 Microtops sun photometer (left) and SIMBAD radiometer (right).

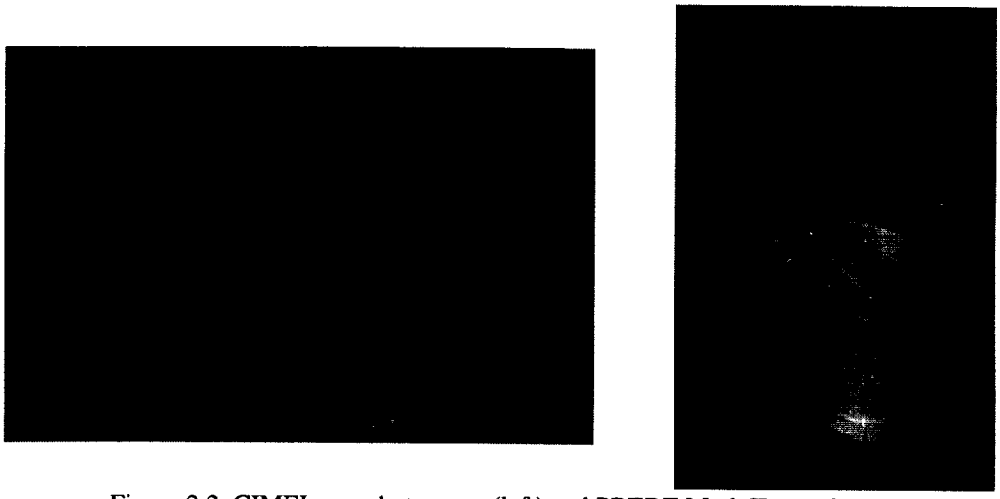

Figure 2.2 CIMEL sun photometer (left) and PREDE Mark II sun photometer (right).

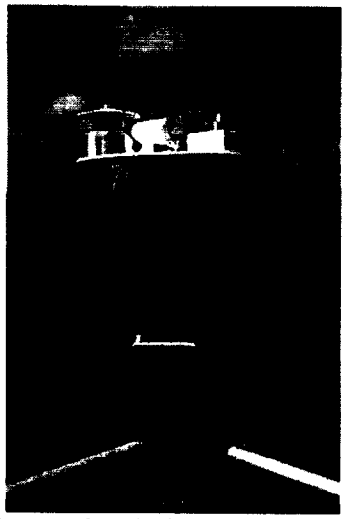

Figure 2.3 Fast rotating shadow-band radiometer (FRSR)

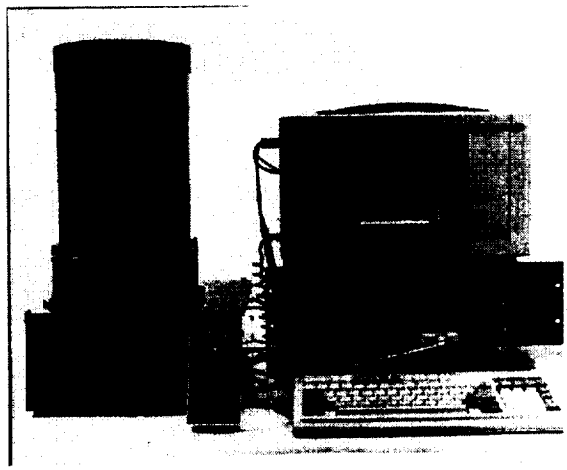

Figure 2.4 Micropulse Lidar (MPL)

avoid-pointing errors. The MicroTops is powered with alkaline batteries allowing 50 hours of operation between changes. SIMBAD is equipped with rechargeable batteries that a allow 6 hours of continuous use.

The MicroTops is also equipped with a microprocessor that calculates the aerosol optical depth, integrated water vapor, and air mass in real time, and displays these values on a LCD screen. The techniques for marine reflectance measurements using the SIMBAD radiometer are given in Deschamps et al. (2000), and those for ship board measurements using the MicroTops sun photometer are given in Porter et al. (2000). The operation and maintenance protocols for the SIMBAD and MicroTops instruments are described in Chapter 4.

2.3 AUTOMATIC SUN PHOTOMETER AND SKY RADIANCE SCANING SYSTEMS

Automatic sun photometers and sky radiometers are more complex than their hand-held counterparts. They allow the retrieval of aerosol and water vapor column amounts from direct sun measurements and the retrieval of aerosol properties from sky radiance measurements. The automatic instruments are often heavy and bulky because of their power requirements, which are generally provided by large batteries. Since they are designed for independent, automatic operation, they need to be weather resistant. As a consequence, they are often expensive to buy. The CIMEL and PREDE instruments (Fig. 2.2), manufactured in France and Japan, respectively, are two sun and sky scanning spectral radiometers used by the SIMBIOS Project.

The CIMEL instruments are used in the AERONET network to globally monitor the aerosol optical properties over land (Holben et al, 1998). Since 1998, the network has grown considerably (Holben et al., 2000). It includes 12 instruments owned by SIMBIOS project, maintained by the AERONET group, and deployed in coastal and island regions to monitor aerosol optical properties over ocean. The CIMEL Electronique 318A, manufactured in Paris, is a multi-spectral radiometer powered by solar panels and batteries. The silicon photodiode detectors in the CIMEL are not temperature-controlled, and a thermistor measures the temperature of the detector, which is used to correct the temperature dependence of the detectors. The PREDE POM Mark II, manufactured in Tokyo, is a multi-spectral radiometer that uses temperature-controlled silicon photodiode detectors (Nakajima et al., 1996). Both instruments have their sensor heads mounted on a robot, allowing zenith and azimuthal motion. A collimator located in front of the entrance optics and an instrument designed for 10^{-5} stray-light rejection allows measurements of the sky aureole 3° from the sun. The CIMEL and the PREDE have approximately 1.2° and 1.5° full fields-of-view, respectively, at each measurement wavelength. The components of the sensor heads are sealed from moisture and desiccated to prevent damage to the electrical components and interference filters. Ion assisted deposition (IAD) interference filters are used by each of the instruments. Their spectral characteristics are given in Table 2.3. When idle,

the CIMEL and the PREDE sensor head are pointed downward (PARK mode) to prevent optical window deterioration from rain or particles. A wetness sensor in the CIMEL detects rain events and initiates the park mode. For the PREDE, a wide field of view camera on top of the robot allows the radiometer to make measurements when sky is cloud free. In addition, the PREDE is equipped with a sophisticated tracking system, including fast responding motors and a narrow field camera coupled with the sensor head, allowing measurements onboard a ship, or other moving platform. A polarization model of the CIMEL is used by the SIMBIOS Project to make measurements of the polarization of the sky radiance at 0.87 μm.

2.4 FAST ROTATING SHADOW-BAND RADIOMETERS

The shadow-band radiometer, equipped with an occulting apparatus, measures the diffuse and global (upper hemispheric) irradiance and computes the solar irradiance as the difference between the two. The device gets its name from the hemispherical metal strip that rotates around the detector and blocks the direct solar beam to yield a signal that is from the sky only (after the effect of the arm is included). The multiple wavelength rotating shadow-band radiometer Harrison et al. (1994) uses independent interference-filter-photodiode detectors and an automated rotating shadow-band technique to make spatially resolved measurements at seven wavelengths. The accuracy of the direct-normal spectral irradiance measurements made with this type of sun photometer is comparable with those made by narrow-beam tracking devices. A significant advantage of the shadow-band technique is that the global and diffuse irradiance measurements can be used to study the solar radiation budget and the fractional cloud cover at the time of the measurement. The latter capability is particularly important for satellite validation studies.

A marine version of the multiple wavelength rotating shadow-band radiometer (Fig 2.3) has been developed at the Brookhaven National Laboratory (BNL) and is operated by Dr. Mark Miller. The BNL marine version uses a slightly modified version of the detector used for continental applications. It has seven channels: one broadband and six 10-nm wide channels at 415, 500, 610, 660, 870, and 940 nm. For shipboard measurements, modifications to the detector circuitry used for continental applications are necessary because the response time of this circuitry is too slow for use on a moving ship. If the response time of the detector is too slow, wave action may cause the orientation of the radiometer to change appreciably during the time the shadow-band is occulting the sun. The rotation of the shadow-band itself must be sufficiently fast for the same reason. The marine version of the shadow-band radiometer (Reynolds et al., 2000) is generally referred to as the BNL Fast-Rotating, Shadow-band Radiometer (FRSR). The response of the silicon cell in the detector used for continental applications is faster than one millisecond, yet the internal preamplifiers have integrating low-noise amplifiers that slow the overall response. For the FRSR, the response time of the detector is made faster by reducing the magnitude of the low-pass filter capacitors. Laboratory tests do not show additional noise in the measurements as a result of this modification. The processing algorithms, which incorporate pitch, roll and heading measurements, are key to the instrument's ability to derive direct-normal beam irradiance without gimbals and a gyro-stabilized table.

A correction for the amount of sky that is blocked by the occulting band is essential for an accurate measurement. For the FRSR shadowband, this correction is possible through measurement of "edge" irradiance in the same manner as the land version of the radiometers. The shadow irradiance occurs when the sun is completely covered by the shadowband, but a portion of the diffuse irradiance is also blocked. The edge irradiance is measured when the band is just to one side of the solar disk and provides a good estimate of the global irradiance minus the portion of sky that is blocked by the shadowband at the time it blocks the solar disk. In practice the edge irradiance is selected from two measurements taken when the shadow is on one side or the other of the diffuser. Generally an average is taken, but in some cases in the early morning or late evening, only one of the edges is acceptable

2.5 MICRO-PULSE LIDAR SYSTEM (MPL)

The MPL (Fig. 2.4) is a compact and eye-safe lidar system capable of determining the range of aerosols and clouds by firing a short pulse of laser light at 523 nm and measuring the time-of-flight from pulse transmission to reception of the returned signal (Spinhirne, 1993). The returned signal is retrieved as a function of time, converted into range using the speed of light, with a magnitude

proportional to the amount of light backscattered by atmospheric molecules (Rayleigh scattering), aerosols, and clouds. The MPL achieves ANSI eye-safe standards by using low output energies (micro Joules, μJ) and beam expansion to 20.32 cm in diameter. The MPL laser pulse duration is 10 ns with a pulse repetition frequency (PRF) of 2500 Hz and output energies range from 1 to 6 μJ depending upon system performance and operational settings. The high PRF allows the system to average many low energy pulses in a short time to achieve a good signal-to-noise ratio. The main characteristics of the MPL are summarized in Table 2.4.

The MPL transmitter-receiver consists of a black, 20.32 cm diameter Cassegrain telescope with optics and electronics mounted directly below the telescope. The laser supply and scalar (data binning unit) are connected to the transmitter-receiver, along with a control computer. The MPL must be operated inside a climate controlled housing. The laser supply contains a diode pumped Nd:YLF laser with a fundamental pulse output wavelength of 1046 nm that is converted to 523 nm by passage through a frequency doubling crystal prior to transmission by the telescope. Signals are received using the same telescope and are recorded with a Geiger mode avalanche photodiode.

Over the years, the MPL design has been fully characterized, and its various strengths, limitations, and nuances are now well understood. The MPL systems are reasonably easy to deploy to the field, are eye-safe, have the capability to operate continuously for extended periods of time, and can detect and analyze various cloud and aerosol layers (including thin cirrus and low concentration aerosol layers). The MPL system is limited by having only one channel for analysis purposes, and a small field-of-view that creates a long overlap range. However, the small field-of-view also eliminates multiple scattering effects present in many other lidar systems.

Procedures have been developed to correct the raw MPL data for afterpulse detector noise (induced by the laser pulse itself), and near-range signal falloff caused by the telescope overlap function. Data analysis algorithms have been written to calibrate the MPL systems and to analyze the resulting data. Successful analysis of the MPL data requires aerosol optical depth measurements from a sun photometer co-located with the lidar. The sun photometer is used to calibrate the MPL and is essential for completion of the data processing routines. MPL data products include: aerosol and cloud layer heights for each layer detected; optical depth; extinction profile; and extinction-backscatter ratio (sr). Optical depth profiles for each layer can be generated by integrating the extinction profile. An overview of MPL data processing techniques is given in Welton et al. (2000). Further information on MPL systems, data processing, and current available data can be found at the MPL-Net web site (http://virl.gsfc.nasa.gov/mpl-net/).

REFERENCES

Deschamps, P. Y., B. Fougnie, R. Frouin, P. Lecomte and C. Verwaerde, 2000: SIMBAD: An advanced field radiometer to measure aerosol optical thickness and marine reflectance, Appl. Opt. in press.

Fougnie, B., R, Frouin, P. Lecomte, and P-Y. Deschamps, 1999: Reduction of skylight reflection effects in the above-water measurement of marine diffuse reflectance. Appl. Opt. 38, 3844-3856.

Harrison, L., J. Michalsky, and J. Berndt, 1994: Automated multi-filter rotating shadow-band radiometer: An instrument for optical depth and radiation measurements, Appl. Opt. 33, 5126-5132.

Holben, B. N., T. F. Eck, I. Slutsker, D. Tanre, J. P. Buis, A. Setzer, E. Vermote, J. A. Reagan, Y. Kaufman, T. Nakajima, F. Lavenu, I. Jankowiak, and A. Smirnov, 1998: AERONET - A federated instrument network and data archive for aerosol characterization, Rem. Sens. Environ. 66, 1-16.

Holben, B. N., D. Tanre, A. Smirnov, T. F. Eck, I. Slutsker, N. Abuhassan, W. W. Newcomb, J. Schafer, B. Chatenet, F. Lavenue, Y. J. Kaufman, J. Vande Castle, A. Setzer, B. Markham, D. Clark, R. Frouin, R. Halthore, A. Karnieli, N. T. O'Neill, C. Pietras, R. T. Pinker, K. Voss, and G. Zibordi, 2000: An emerging ground-based aerosol climatology: Aerosol optical depth from AERONET, J. Geophys. Res. in press.

Morys, M., F. M. Mims, and S. E. Anderson, 1998: Design calibration and performance of MICROTOPS II hand-held ozonemeter, http://www.solar.com/ftp/papers/mtops.pdf, 12pp.

Nakajima T., G. Tonna, R. Rao, P. Boi, Y. L. Kaufman, and B. Holben, 1996: Use of sky

brightness measurements from ground for remote sensing of particulate polydispersions, Appl. Opt. 35, 2672-2686.

Porter, J. N., M. Miller, C. Pietras, and C. Motell, 2000: Ship-based sun photometer measurements using MicroTops sun photometers, J. Atmos. Ocean. Technol. in press.

Reynolds, M., M. A. Miller, and M. J. Bartholomew, 2000: Design, operation, and calibration of a shipboard fast-rotating shadowband spectral radiometer, J. Atmos. Ocean. Technol. in press.

Spinhirne, J. D., 1993: Micro pulse lidar, IEEE Trans. Geosci. Remote Sensing , 31, 48-55.

Welton, E. J., K. J. Voss, H. R. Gordon, H. Maring, A. Smirnov, B. Holben, B. Schmid, J. M. Livingston, P. B. Russell, P. A. Durkee, P. Formenti, M. O. Andreae, 2000: Ground-based lidar measurements of aerosols during ACE-2: Instrument description, results, and comparisons with other ground-based and airborne measurements, Tellus B 52, 635-650.

Table 2.1 Characteristics of the SIMBIOS instruments

Channels nanometers	MicroTops	SIMBAD	CIMEL	PREDE	SHADOW-BAND	MPL
315				✔		
340			✔			
380			✔			
400				✔		
415					✔	
440	✔	✔	✔			
490		✔				
500	✔		✔	✔	✔	
523						✔
560		✔				
610					✔	
660					✔	
670		✔				
675	✔		✔	✔		
870	✔	✔	✔	✔	✔	
940	✔		✔	✔	✔	
1020			✔	✔		
FOV	2.5	3	1.2	1.5	180	0.00573

Table 2.2 Center wavelengths (CWL) and bandwidths (BWL) of the channels of each MicroTops and SIMBAD radiometer.

MicroTops	Ch1		Ch2		Ch3		Ch4		Ch5	
Units #	CWL	BWL	CWL	BWL	CWL	BWL	CWL	BWL	CWL	BWL
03755	440.6	10.1	499.7	10.4	674.3	10.8	869.7	10.1	936.2	10.0
03765	440.4	10.1	499.7	10.3	674.0	10.8	870.1	10.1	935.7	9.5
03766	440.6	10.2	499.7	10.4	674.8	10.7	865.5	10.1	935.6	9.4
03767	440.7	10.0	499.6	10.4	674.0	10.7	870.3	10.2	937.2	10.8
03768	440.6	101	499.5	10.3	674.5	10.8	870.2	10.1	936.3	9.3
03769	440.7	10.0	499.5	10.3	674.3	10.9	869.5	9.8	935.9	9.3
03770	440.6	10.1	499.7	10.4	674.5	10.9	869.9	10.2	937.1	10.8
03771	440.4	10.2	499.6	10.4	674.1	10.8	870.1	10.1	936.5	10.9
03772	440.7	10.2	499.6	10.4	674.3	10.8	870.0	10.2	935.9	10.9
03773	440.6	10.0	499.6	10.4	674.1	10.8	870.2	10.2	937.1	10.8
03774	440.5	10.1	499.8	10.4	674.4	10.8	870.6	10.0	935.9	9.3
03775	440.7	10.1	499.8	10.4	674.4	10.7	870.0	10.1	934.9	9.3
SIMBAD Unit #										
972306	442.7	11.6	491.9	11	562.2	9.0	672.0	10.0	875.2	12.7
972309	441.6	11.7	491.9	11	562.7	9.1	670.8	10.3	872.4	11.4

Table 2-3. Center wavelength (CWL) and Bandwidth (BWL) of the channels of PREDE and CIMEL sun photometers.

PREDE	Ch1		Ch2		Ch3		Ch4		Ch5		Ch6		Ch7	
Units #	CWL	BWL	CWL	BWL	CWL	BWL	CWL	BWL	CWL	BWL	CWL	BWL	CWL	BWL
PS 090063	314.5	3.0	400.3	9.6	501.0	9.6	676.0	10.1	868.8	10.3	940.4	10.2	1019.2	8.9
PS 090064	314.8	3.0	400.1	9.4	500.9	9.7	675.7	10.1	869.7	10.5	940.2	10.2	1019.3	9.0

CIMEL	Ch1		Ch2		Ch3		Ch4		Ch5		Ch6		Ch7		Ch8	
Unit #	CWL	BWL	CWL	BWL	CWL	BWL	CWL	BWL	CWL	BWL	CWL	BWL	CWL	BWL	CWL	BWL
93	339.9	1.7	379.4	3.9	440.6	9.3	500.6	10.0	675.6	8.6	870.1	10.7	936.1	10.0	1021.4	10.2
106	340.0	1.8	379.4	3.9	440.4	9.9	499.0	9.8	674.4	8.6	869.6	10.6	936.1	8.7	1019.1	9.9
107	339.7	1.8	379.4	3.8	440.6	9.8	500.7	10.0	674.8	10.3	870.0	10.7	935.7	9.9	1019.5	9.8
108	339.8	1.8	379.6	3.8	NA	NA	499.4	9.9	675.8	9.0	870.4	10.7	935.0	10.3	1018.8	9.9
109	339.7	1.7	379.6	3.9	440.7	9.5	500.4	9.9	674.4	8.6	869.1	10.5	935.9	9.8	1019.4	9.8
151	339.9	1.8	379.4	3.9	440.5	9.9	676.0	9.6	499.4	9.8	869.6	10.5	935.5	9.8	1020.6	10.4
155	340.1	1.9	380.2	1.9	440.7	8.5	501.0	9.9	674.8	10.3	869.3	10.5	935.8	8.7	1020.5	9.9
159	339.8	1.9	380.2	1.9	440.5	8.3	501.0	9.9	674.9	10.2	869.3	10.6	936.8	10.5	1020.1	9.7
160	339.9	1.8	380.2	1.9	439.8	8.5	501.3	9.9	674.9	10.2	869.7	10.5	936.3	8.8	1020.4	9.8
161	339.9	1.8	380.2	1.9	440.2	9.2	501.2	9.8	674.9	10.3	869.2	10.6	935.4	8.8	1020.2	9.7
162	440.6	9.0	674.6	10.3	869.8	9.2	869.8	9.2	868.6	9.2	869.8	9.2	935.1	8.7	1019.7	9.6
191	440.5	8.3	674.9	10.3	870.0	9.3	869.8	9.3	869.7	9.2	870.1	9.2	936.0	8.7	1020.3	9.8

Table 2.4 MPL System Specifications

Parameter Name	Parameter Value
Wavelength	523 ± 0.12 nm
Output Pulse Energy	< 10 μJ
Pulse Duration	10 ns
Pulse Repetition Frequency	2500 Hz
Field of View	100 μrad (0.00573°)
APD Detector Quantum Efficiency	40%
APD Detector Dark Count Rate	< 250 counts per second
Vertical Resolution	75 m
Temporal Resolution	1 minute

(3) TR NN/35

Chapter 3

Calibration of Sun Photometers and Sky Radiance Sensors

Christophe Pietras[1], Mark Miller[2], Robert Frouin[3], Tom Eck[4] and Brent Holben[5], John Marketon[4]

[1]*SAIC General Sciences Corporation, Beltsville, Maryland*
[2]*Department Environmental Science, Earth System Science Division, Brookhaven National Laboratory, Upton, New York*
[3]*Scripps Institution of Oceanography, University of California, San Diego, California*
[4]*Raytheon ITSS Corporation, Lanham, Maryland*
[5]*Biospheric Sciences Branch, NASA Goddard Space Flight Center, Greenbelt, Maryland*

3.1. INTRODUCTION

The main source of error in retrieving aerosol optical thicknesses using sun photometry comes from the determination of the TOA voltages. The degradation of interference filters is the most important source of the long-term changes in the cross-calibrations. Although major improvements have been made in the design of the filters (interference filters fabricated using ion-assisted deposition), the filters remain the principal factor limiting performance of the sun photometers. Degradation of filters necessitates frequent calibration of sun photometers and frequent measurements of the filter transmission or the relative system response (Schmid et al., 1998). The degradation of the filters mounted on the CIMEL sun photometers have been monitored since 1993 by the AERONET Project. The decay reported by Holben et al. (1998) for the first 2 years of a CIMEL's operation is between 1 and 5%. Nevertheless, the filters mounted on CIMEL instruments are regularly replaced after 2 years of use. The cross-calibration technique consists of taking measurements concurrently with the uncalibrated and the reference sun photometers. While analyzing measurements, the quality of the calibration has to be checked, using the following considerations:

1. any cirrus clouds suspected to be masking the sun, during the calibration period, need to be reported and the corresponding data set removed; and
2. the stability of the day needs to be checked.

Then, the average and standard deviation of TOA voltages are computed during the entire period of each calibration. If the standard deviation is higher than 1%, the calibration is rejected and will not be part of the data processing.

Absolute calibration of the sky radiometers depends on the accuracy of the calibration of the reference integrating sphere. The NIST-traceable calibration of the integrating sphere at GSFC is considered to be accurate at better than 5%. The calibration history of SIMBAD shows a stability of the calibration within ±5% over three years. The calibration of radiometers during a field experiment is possible using a plaque, but higher uncertainties are expected (as shown on Figure 3.4) because of the uncertainty of the determination of the reflected signal from the plaque.

Absolute calibration depends also on the relative size of the entrance aperture of the sphere, on the field-of-view of the radiometer, and on the distance between the sphere and the radiometer. The first absolute calibration performed at GSFC (August 1999) was performed with the radiometer placed one meter from the sphere. The calibration coefficients, as shown on Figure 3.4, are higher than those derived from later calibrations performed using a distance reduced to 0.1 meter. The Hardy sphere has a large aperture and allows a flexibility in the distance setting of the radiometer. However, the reflection of the light from the optical bench, the wall of the room, or the edge of the sphere may explain the higher signal measured by the radiometer and the resulting calibration coefficients.

This chapter will describe calibration techniques, facilities, and protocols used for calibrating sun photometers and sky radiometers.

Measurements and data analyses are discussed in Chapter 6.

3.2 CALIBRATION FACILITIES

GSFC Roof Platform

A platform has been built by the AERONET Group on the roof of the Earth Sciences building at GSFC (Figure 3.1) which has a nearly clear unobstructed horizon. The roof platform allows sun photometer cross-calibrations during every clear (low AOT) days. Absolute calibrations using lamp standards are generally not recommended for the retrieval of aerosol optical thickness (AOT). However, in the case of an instrument with a large decrease in sensitivity over time, it may be advisable to combine the standard lamp calibration with solar calibration (Schmid et al., 1998). All AERONET automatic sun photometers are set up on this platform for cross-calibration. The roof platform is equipped with one or more CIMEL reference sun photometers, calibrated at Mauna Loa Observatory (Hawaii, altitude 3400m). The reference sun photometers are used to transfer the calibration to field instruments by making measurements simultaneously. After cross-calibration, these sun photometers are shipped to designated monitoring sites or for field experiments. The roof platform has been built at GSFC primarily for the calibration of CIMEL instruments, but the facility is also used to cross-calibrate other sun photometers (MicroTops, SIMBAD, PREDE).

Radiance Calibration Facility

The instruments were calibrated in the Code 920.1 Radiance Calibration Facility (RCF), located at NASA's GSFC. The RCF maintains instruments and NIST-traceable calibrated sources to calibrate, monitor, and assess the performance of remote sensing instrumentation. To reduce the effects of particulate contamination, the RCF is located in an ISO Class 7 (M5.5, 10000) contamination controlled suite. The main RCF source is a 1.8m diameter fiberglass integrating sphere named Hardy (Figure 3.2). The sphere interior is coated with BaSO4 in a Poly-Vinyl Alcohol (PVA) binder over a Krylon flat white base coat (GSFC WI 1998). Sixteen 200W Quartz Tungsten Halogen lamps, arranged around the 25.4cm primary exit aperture internally illuminate the sphere. The lamps are baffled so that radiation does not directly exit through the aperture. Two baffled 20cm ports are used for air circulation, with a blower drawing on the hot air exhaust vent. Located directly above the primary exit aperture is a 5cm diameter monitor port with a bracket for securing a source monitor. A source monitor was not installed for the calibrations described in this paper. A constant current power system (Walker et al., 1994) is used to drive the lamps. The power system permits up to sixteen sphere output levels by supplying power to the appropriate number of lamps.

The Hardy sphere source is calibrated on a monthly basis against NIST FEL irradiance standard lamps in the visible and near-infrared spectral region (0.4 and 2.4μm). The FEL irradiance calibration is transferred to the integrating radiance source using a transfer radiometer with an integrating sphere irradiance collector (Mueller, et al., 1993 and Walker, et al. 1991). Overall calibration uncertainty (Figure 3.3) is about 1.5% in the visible region and generally under 2.5% across the calibrated region. The greatest contributor to the uncertainty is the FEL lamp itself.

3.3 TECHNIQUES AND PROTOCOLS

The ongoing calibration of sun photometers is a necessary to account for instrument changes, including changes in the sensitivity of detectors and changes in the transmittances of the interference filters. Since the time of the pioneering work of Voltz (1959), several papers have discussed various methods to improve the solar calibration. Schmid et al. (1998) used lamp and solar calibrations in conjunction with each other; O'Neill et al. (1984) combined solar aureole and solar beam extinction measurements; and Soufflet et al. (1992) and Holben et al. (1998) used well-calibrated reference sun photometers.

Calibration of the Reference Sun Photometers

Three AERONET reference sun photometers are calibrated at Mauna Loa Observatory (MLO, 3400m) at 1-3 months intervals. The reference instruments have the same characteristics as the CIMEL sun photometers deployed in the field. These MLO calibrated CIMELs are used by the AERONET network to cross-calibrate the other CIMELs and by the SIMBIOS Project to cross-calibrate other types of sun photometers (MicroTops, SIMBAD, PREDE). A three month cycle is maintained to keep one or two MLO calibrated CIMELs on the GSFC roof platform, one

at the Mauna Loa Observatory for calibration, and one in transit at times between locations.

The Langley-Bouguer technique is used to determine the top-of-the-atmosphere (TOA) signals (signals at zero airmass) for each channel of each reference sun photometer. Holben et al. (2000) have reported the calibration history of the MLO calibrated instruments #101. Table 3.4 presents the TOA signals this reference CIMEL, derived from the successive calibrations performed at Mauna Loa Observatory since September 1997. Since then, the percent changes in V_0, the TOA signal at zero airmass, are -1.73 % yr^{-1}, -0.69 % yr^{-1}, -4.23 % yr^{-1}, 0.05 % yr^{-1}, 0.71 % yr^{-1}, and 0.37 % yr^{-1} at 440, 500, 675, 870, 940, and 1020 nm, respectively.

Sun Photometer Cross-Calibration

The cross-calibration technique applied by Holben et al. (1998) to the reference CIMEL instruments has been extended to the complete pool of SIMBIOS sun photometers. The reference sun photometers are calibrated, using the Langley-Bouguer technique, in high altitude conditions at

Figure 3.1 Roof platform at Goddard Space Flight Center used for transferring calibration to sun photometers.

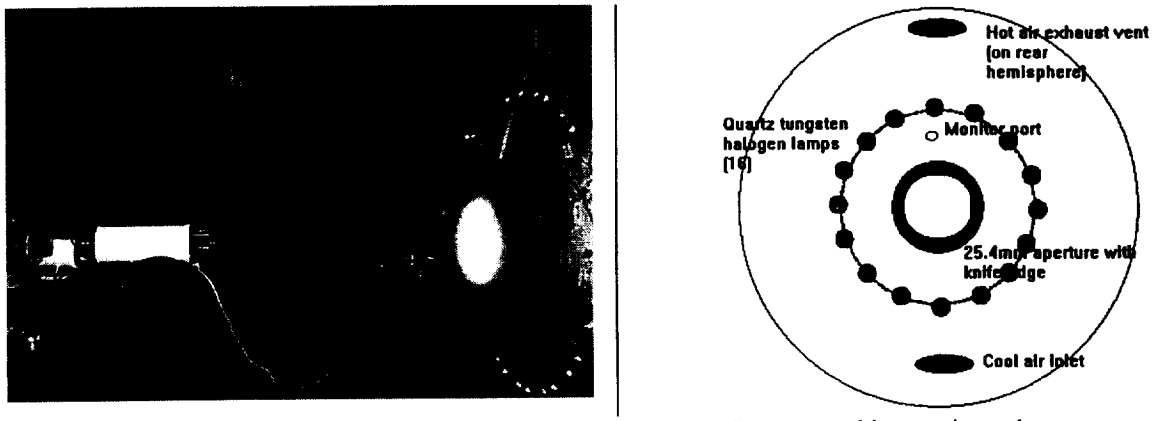

Figure 3.2 Integrating Sphere Hardy used to calibrate the SIMBAD radiometer and integrating sphere source.

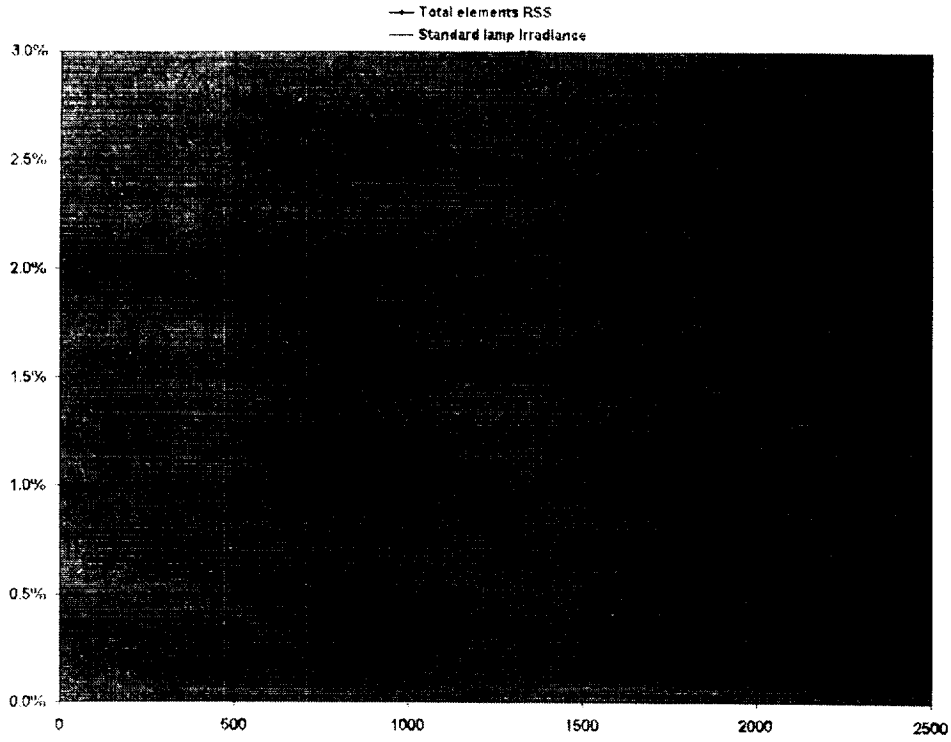

Figure 3.3 Integrating Sphere Calibration uncertainty.

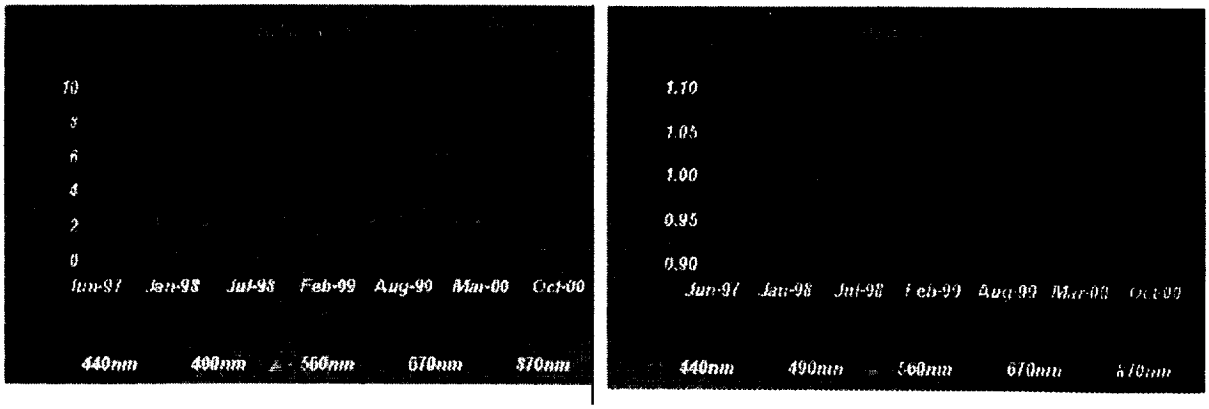

Figure 3.4 Absolute calibration of the SIMBAD radiometer at GSFC and at LOA. Top figure presents the historic calibration coefficients since March 1997. The bottom figure presents the ratio of the calibration coefficient C_i to the coefficient C_i^1 obtained the first calibration (March 1 1997).

Mauna Loa (Hawaii). The Langley-Bouguer technique and its limitations are described in chapter six of Fargion et al. (2000). The cross-calibration technique consists of taking concurrent measurements with the reference and the uncalibrated sun photometers. Since the time difference is less than one minute and since the solar zenith angle is lower than 70°, the TOA voltage from the uncalibrated instrument is calculated relative to the ratio of the voltages from the reference instrument,

$$V_0(\lambda_i) = V_0^{ref}(\lambda_i) * \frac{V(\lambda_i)}{V^{ref}(\lambda_i)}, \qquad (3.1)$$

where $V_0^{ref}(\lambda_i)$ is the TOA signal for channel λ_i of the reference CIMEL and $V(\lambda_i)$ and $V^{ref}(\lambda_i)$ are the signals measured by the uncalibrated and reference sun photometers. Some sun photometers have channels (λ_i's) which are slightly different from any of those in the reference instrument. In this case, the closest channel of the reference sun photometer is used in the calculations, and the TOA voltages are obtained using

$$V_0(\lambda_i) = V_0^{ref}(\lambda_j) * \frac{V(\lambda_i)}{V^{ref}(\lambda_j)} * \exp\left[M(\theta_0) * \left(\tau_R(\lambda_i) - \tau_R(\lambda_j)\right)\right] * \exp\left[m(\theta_0) * \left(\tau_o(\lambda_i) - \tau_o(\lambda_j)\right)\right] * \exp\left[m(\theta_0) * \tau_a(1\mu m)\left(\lambda_i^{-\alpha} - \lambda_j^{-\alpha}\right)\right] \qquad (3.2)$$

where λ_j is the wavelength of the channel in the reference instrument. In Equation (3.2), the first exponential term gives the difference in the Rayleigh optical thickness between wavelengths λ_i and λ_j, the second exponential term is the difference in the ozone optical thickness, and the third term gives the difference in the aerosol optical thickness. In the equation, α and $\tau_a(1\ \mu m)$ are the Angström coefficient and the aerosol optical thickness at 1 μm determined from CIMEL reference measurements using the Angström law:

$$\tau_a(\lambda) = \tau_a(1\mu m) * \lambda^{-\alpha} \qquad (3.3)$$

According to Table 3.1, most of the sun photometers have channels that are common with those in the reference CIMEL reference, allowing a simple application of the cross-calibration technique in Equation (3.1). The stability of the aerosol extinction is not critical when the wavelengths of the of the reference and field instruments are slightly different. However, in this case, the standard deviations of the TOA voltages need to be determined over time. The protocols of the cross-calibration are summarized below:

1. set the GMT time on both calibrated and uncalibrated sun photometers;
2. initiate measurements as soon as the calibrated sun photometer starts working;
3. take measurements concurrently with the calibrated sun photometer, between 10 a.m. and 3 p.m. local time to have suitable airmass;
4. measure the dark current to avoid temperature effects;
5. record the sky condition in case of clouds or thin cirrus occurrences (cloud coverage and cloud positions in the sky); and
6. stop when the airmass reaches 3 or when the sky condition changes.

The SIMBIOS sun photometers are routinely cross-calibrated at least every three months or before each field campaign. Calibrations are performed during days with clear and stable atmospheric conditions (AOT at 0.44 μm typically lower than 0.15). The uncertainties of the cross-calibration combine the uncertainties of the calibrated reference sun photometer and the uncalibrated sun photometer. The calibration transfer from the reference sun photometers to uncalibrated instruments using the cross-calibration technique at least doubles the uncertainty of derived $V_0(\lambda)$ for instruments of the same design. According to Holben et al. (1998), the uncertainties in AOTs obtained for cross-calibrated CIMEL instruments are estimated to be 0.01 to 0.02 in AOT. The uncertainties are greater when the cross-calibrated sun photometer is not of the same design as the reference sun photometer.

Sky Radiometer Calibration

Sky radiance scanning systems are automated instruments dedicated to measure sky radiances in the aureole and in the principal plane of the sun. Radiative properties of aerosols are retrieved using an inversion algorithm of the sky radiances (Dubovik et al., 2000, Nakajima et al., 1996) and of the polarized component of the sky radiances (Vermeulen et al., 2000). This section is dedicated to the description of calibration techniques for retrievals of sky radiances.

Radiometers, such as CIMEL and PREDE, are calibrated for sky radiances using an integrating sphere. The radiometer is aligned in front of the sphere, and ten measurements are taken for each channel. Radiances from the integrating sphere are then integrated over the spectral responses of each

channel of the radiometer. As a result, ratios of raw radiometer voltages to the integrated sphere radiances are obtained. These ratios give radiometer calibration parameter C_i (also called the instrument responsivity)

$$C_i = \frac{V_i}{\int L(\lambda) R_i(\lambda) d\lambda}, \quad (3.4)$$

where V_i is the voltage measured by channel i, $R_i(\lambda)$ is the spectral response of the channel, and $L(\lambda)$ is the spectral radiance of the integrating sphere. The accuracy of the radiometer calibration is dependent on the calibration of the integrating sphere, the sphere's size, the clarity of the calibration protocols, and the precision of the calibration process. A two-meter integrating sphere is available and managed by NASA GSFC Calibration Facility (http://spectral.gsfc.nasa.gov/). The uncertainty of the radiances provided by this integrating sphere is estimated to be less than 5%. The protocols for doing the absolute calibration are summarized below:

1. align the optical axis of the radiometer with the optical axis of the integrating sphere;
2. turn on the integrating sphere using the maximum numbers of lamps, and wait at least 30 minutes before starting any measurements;
3. control the signal from the radiometer (If the signal is saturated, decrease the intensity of the light source by turning off an even number of lamps, and wait a couple of minutes for stabilization);
4. cover the aperture output of the sphere, the aperture entrance of the radiometer, and take dark measurements;
5. uncover the exit aperture of the integrating sphere and take measurements for each channel;
6. start again with a reduced number of lamps; and
7. record the data and the radiances from the calibrated integrating sphere.

3.4 CALIBRATION HISTORY

Cross-Calibration History

The cross-calibration of the SIMBIOS sun photometers has been performed at GSFC since 1998. Each sun photometer in the SIMBIOS instrument pool has been cross-calibrated using the same technique. Several SIMBIOS CIMELs (serial numbers 94, 37, 27 and 101) have been used as reference instruments and have been calibrated at Mauna Loa. The cross-calibration is considered complete when:

1. enough simultaneous measurements are selected;
2. time difference is lower than 40 seconds; and
3. TOA standard deviation over the calibration period is less than 1%.

Table 3.3 shows the TOA voltages for each sun photometer cross-calibrated with a reference Cimel. The average values for the TOA voltages and their standard deviations are given for each spectral channel.

Sphere Calibration History

Absolute calibration of sky and above water radiometers have been performed at GSFC since 1998 (see Table 3.2). Figure 3.4 shows the calibration history for SIMBAD number 972306. Calibrations were performed on August 1999, January 2000, and March 2000. They are compared with calibrations performed at LOA (Lille, France) on November 1997, March 1998, and June 1999. The top panel of Figure 3.5 gives the calibration coefficients (C_i) in all channels. The bottom panel gives the ratios of the coefficients (C_i's)to the value from the first calibration (C_i^1). The plots show that the variations are within ±5%. Only the calibration using the plaque has greater variations because of the higher uncertainties in determining the radiances from the plaque. A greater variation is also found in the first calibration at GSFC. This difference may have been caused by a greater distance between the instrument and the sphere during the calibration (1 meter) than the distance chosen for other calibrations (0.1 meter). Unexpected light flux from the room or from the edges of the sphere may have contributed to the measurement results and may explain the higher calibration coefficient on this date. Comparable results have been retrieved with the other SIMBAD (number 972309) and with the CIMEL instruments. Calibration of polarized radiometers, using the integrating sphere Hardy, are described in a separate chapter.

3.5 CONCLUSIONS

The techniques for calibrating the sun photometers and sky radiometers in the SIMBIOS pool of instruments have been developed. The protocols for taking accurate measurements and

allowing accurate calibration are in place as well. Sun photometers and sky radiometers calibrations have been performed successfully by the SIMBIOS Project since 1998. The calibration facilities have been designed to accurately calibrate any instrument. Protocols to use these facilities have been refined to minimize the uncertainties in the measurements. Many calibrations have been performed since 1998, and the history has shown long-term stability of the cross-calibrations (better than 3%) and the absolute calibration using integrating spheres (within ±5%). However, refinements of the protocols should help reduce the calibration uncertainties. The clean room where the sphere is located is now contamination controlled for particulates in the air. This may improve the stability of the calibration of the integrating sphere. In addition, a device (a single channel radiometer mounted in the back of the sphere) has been added to monitor fluctuations in the sphere intensity during calibrations. The device will help determine the contribution of variations in the sphere output to the results of the calibration measurements. The calibration of the reference sun photometer at Mauna Loa is well known. The long-term stability of the SIMBIOS cross-calibrations has been monitored for three years. However, a detailed study of the uncertainties propagated through the calibration transfer has yet to be conducted. Effects caused by different fields-of-view, filters, and detectors need to be accounted for as well.

REFERENCES

Dubovik, O., and M.D. King, 2000: A flexible inversion algorithm for retrieval of aerosol optical properties from Sun and sky radiance measurements, J. Geophys. Res. (submitted).

Fargion, G., J.L. Mueller, and C.R. McClain, 2000: Ocean Optics Protocols For Satellite Ocean Color Sensor Validation, Revision 2. NASA Tech. Memo, NASA Goddard Space Flight Center, Greenbelt, Maryland, 147 pp.

Goddard Space Flight Center (GSFC) Work Instruction 545-WI-8072.1.22, 1998: Procedure for Formulation/Application of MS-125, A Barium Sulfate Optical Coating Standard.

Holben, B.N., T.F. Eck, I. Slutsker, D. Tanre, J.P. Buis, A. Setzer, et al., 1998: A federated instrument network and data archive for aerosol characterization, Remote Sens. Environ., 66, 1-16.

Holben, B.N., D.Tanre, A.Smirnov, T.F.Eck, I.Slutsker, N.Abuhassan, et al., 2000: An emerging ground-based aerosol climatology: Aerosol Optical Depth from AERONET, J. Geophys. Res., In press

Mueller, J., C. Johnson, et al., 1993: The Second SeaWiFS Intercalibration Round-Robin Experiment, SIRREX-2, SeaWiFS Technical Report Series, NASA Technical Memorandum 104566, 16, 3-4, 23-24.

Nakajima, T., G. Tonna, R. Rao, P. Boi, Y.L. Kaufman, B. Holben, 1996: Use of Sky brightness measurements from ground for remote sensing of particulate polydispersions, Appl. Opt., 35, 15, 2672-2686.

O'Neill, N.T., and J.R. Miller, 1984: Combined solar aureole and solar beam extinction measurement, 1: Calibration considerations, Appl. Opt., 23, 3691-3696.

Schmid, B., P.R. Spyak, S.F. Biggar, C. Wehrli, J. Sekler, T. Ingold, C. Mätzler, and N. Kämplr, 1998: Evaluation of the applicability of solar and lamp radiometric calibrations of a precision Sun photometer operating between 300 and 1025 nm, App. Opt., 37, 18, 3923-3941.

Soufflet, V., C. Devaux, D. Tanre, 1992: A modified Langley Plot method for measuring the spectral aerosol optical thickness and its daily variations, Appl. Opt., 31, 2154-2162.

Vermeulen, A., C. Devaux., and M. Herman, 2000: Retrieval of the scattering and microphysical properties of aerosols from ground-based optical measurements including polarization, Appl.Opt. (submitted).

Volz, F., 1959: Photometer mit selen-photoelement zur spectralen messung der sonnenstrahlung und zur bestimmung der wellenlangenabhangigkeit der dunsttrubung, Arch. Meteor. Geophys. Bioklimatol. Ser., B10, 100-131.

Walker J., C. Cromer, J. McLean, 1991: A technique for improving the calibration of large-area sphere sources, SPIE Vol. 1493 Calibration of Passive Remote Observing Optical and Microwave Instrumentation, 224-230.

Walker, J. and A. Thompson, 1994: Improved Automated Current Control for Standard Lamps, J. Res. Natl. Inst. Stand. Technol. 99, 255-261.

CIMEL #101

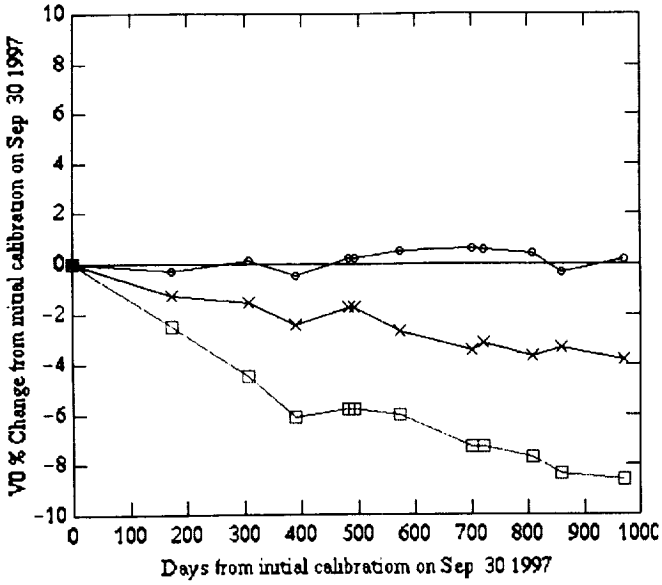

CIMEL# 108

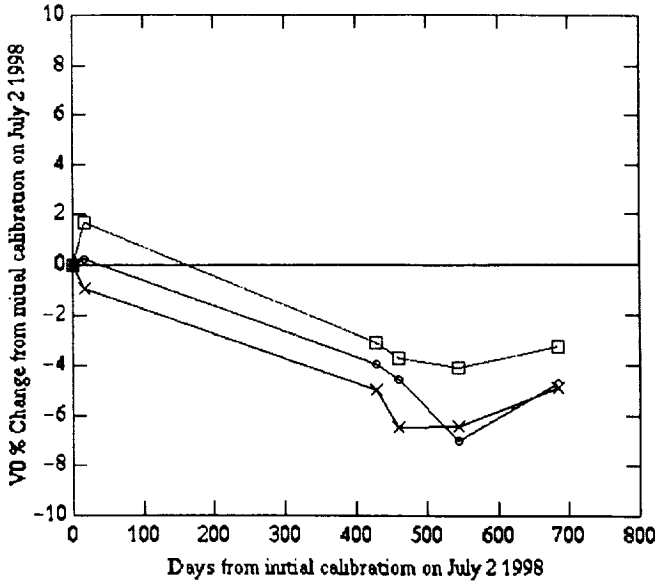

MicroTops #3772

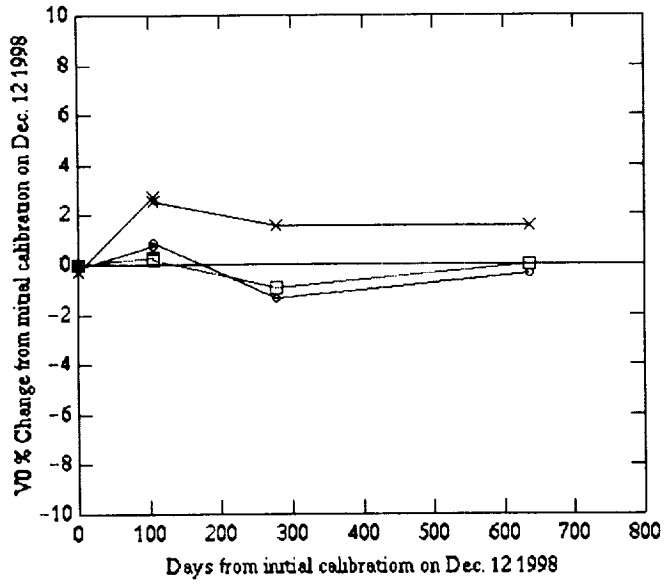

SIMBAD #972306

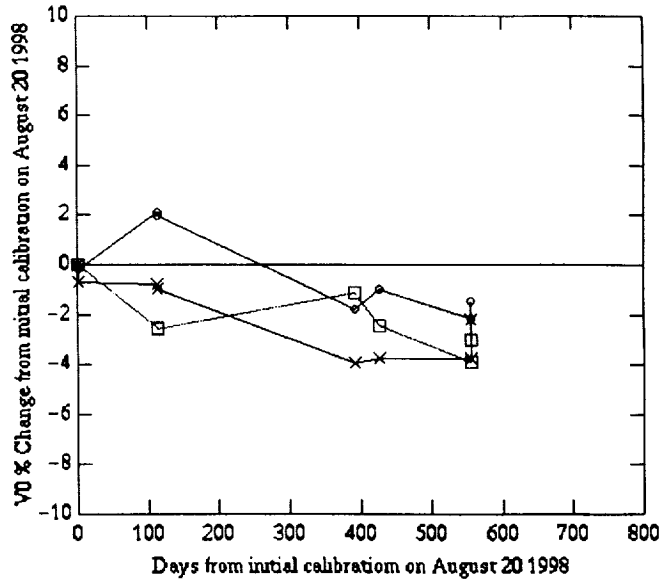

Figure 3.5 Calibration history for Cimel MLO calibrated #101, Cimel in the filed #108, MicroTops 3772, and Simbad #972306

Table 3-1 Calibration history of the CIMEL #101 at Mauna LOA (Hawaii) since 1997.

Date	440 nm	500 nm	675 nm	870 nm	940 nm	1020nm
1997-09-30	13843	15695	17281	13576	17189	14960
1998-03-23	13671	15626	16852	13535	17322	14973
1998-08-08	13628	15615	16525	13598	16969	15069
1998-10-29	13508	15505	16262	13514	17921	14975
1999-02-03	13605	15620	16313	13610	17194	15043
1999-02-13	13605	15620	16313	13610	17194	15043
1999-05-04	13479	15511	16270	13647	17022	15097
1999-09-11	13374	15453	16064	13660	17207	15089
1999-10-02	13416	15497	16064	13654	17578	15123
1999-12-29	13343	15405	16002	13635	17512	15019
2000-02-19	13388	15505	15894	13533	17916	15025
2000-06-11	13324	15448	15855	13605	17445	15017

Table 3.2 Calibration activities conducted at GSFC since 1998

Date	Instruments	Calibration Type
1998-08-20	MicroTops 3769, 3773; Simbad 972306; Prede PS090063	Sun cross calibration
1998-08-21	MicroTops 3769, 3773; Simbad 972306; Prede PS090063	Sun cross calibration
1998-10-16	MicroTops 3765, 3766, 3773; Simbad 972306; Prede PS090064	Sun cross calib
1998-11-12	MicroTops 3765, 3766, 3768, 3770	Sun cross calibration
1998-11-24	MicroTops 3772, 3773; Simbad 972306; Prede PS090064	Sun cross calibration
1998-12-14	MicroTops 3755, 3765, 3768, 2770, 3772; Simbad 972306; Prede PS090064	Sun cross calibration
1999-01-08	Polorized Cimel 25, 92, 111	Sphere calibration
1999-01-19	Polorized Cimel 14, 43, 45	Sphere calibration
1999-03-30	MicroTops 3755, 3767, 3768, 3772	Sun cross calibration
1999-05-29	Polorized Cimel 191	Sphere Calibration
1999-06-09	MicroTops 3768, 3769, 3773, 3775	Sun cross calibration
1999-08-12	Simbad 972306, 972309	Sphere Calibration
1999-09-23	MicroTops 3765, 3768, 3772; Simbad 972306, 972309	Sun cross calibration
1999-10-28	MicroTops 3767; Simbad 972306	Sun cross calibration
2000-01-04	Simbad 972303, 972306, 972307, 972308, 972309	Sphere calibration
2000-01-14	MicroTops 3767, 3768, 2770, 3775; Simbad 972309	Sun cross calibration
2000-03-06	Simbad 972301, 972306, 972307, 972309, 972310	Sphere calibration
2000-03-06	MicroTops 3766, 3773; Simbad 972306, 972309	Sun cross calibration
2000-07-03	Polorized Cimel 188	Sphere calibration
2000-08-18	Simbad 972303, 972306, 972308	Sphere calibration
2000-09-20	MicroTops 3755, 3765, 3767, 3768, 3772, 3773	Sun cross calibration

Table 3.3 Cross-calibration history conducted at GSFC since 1998 for the MicroTops and SIMBAD sun photometers. The average values of the TOA voltages and the standard deviation are given for each sun photometer. The reference CIMEL units used for each calibration are indicated as well as the time difference (Δt) of measurements taken by the reference CIMEL and the corresponding sun photometer.

MicroTops Units #	CIMEL Units #	Δt s	Date	440 nm	500 nm	675 nm	870 nm	940 nm
						V_0+/-ΔV_0		
03755								
factory	-	-	-	800	915	836	786	1400
	94	14	1998-12-14	765+/-2	872+/-2	668+/-2	742+/-3	2113+/-12
	101	14	1998-12-14	764+/-2	872+/-2	668+/-2	741+/-3	1970+/-12
	37	20	1999-03-30	806+/-1	880+/-1	644+/-1	782+/-2	1868+/-4
	94	19	1999-03-30	807+/-1	885+/-3	643+/-1	781+/-2	2234+/-9
	37	16	2000-09-20	788+/-4	884+/-3	566+/-2	777+/-3	1852+/-21
03765								
factory	-	-	-	1263	990	1147	831	1454
	27	71	1998-10-16	1105+/-8	916+/-6	1246+/-8	801+/-3	1722+/-7
	27	17	1998-11-12	1036+/-5	884+/-5	1350+/-13	797+/-6	1739+/-16
	94	63	1998-12-14	1226+/-3	987+/-4	1148+/-6	825+/-2	2334+/-11
	101	63	1998-12-14	1224+/-3	987+/-3	1148+/-6	824+/-2	2176+/-10
	94	50	1999-09-23	1235+/-3	978+/-4	1150+/-3	827+/-3	2373+/-7
	37	17	2000-09-20	1237+/-5	982+/-3	1156+/-3	825+/-2	2001+/-12
03766								
factory	-	-	-	1224	992	1191	807847	1546
	27	80	1998-10-16	1054+/-7	906+/-9	1312+/-7	811+/-2	1820+/-14
	27	18	1998-11-12	1011+/-22	866+/-24	1389+/-22	803+/-9	1857+/-35
	37	13	2000-03-06	1226+/-4	983+/-11	1195+/-10	838+/-4	2113+/-18
	106	18	2000-03-06	1212+/-13	977+/-10	1185+/-14	833+/-12	1552+/-17
03767								
	37	13	1999-03-30	1157+/-4	982+/-5	1190+/-4	794+/-2	2472+/-15
	94	11	1999-03-30	1160+/-4	989+/-5	1190+/-3	793+/-2	2957+/-21
	101	22	1999-10-28	1108+/-9	976+/-6	1183+/-6	789+/-4	2712+/-19
	94	16	2000-01-14	1084+/-8	997+/-4	1209+/-2	797+/-4	2939+/-17
03768								
factory	-	-	-	1236	989	1195	807	1616
	27	14	1998-11-12	882+/-5	873+/-5	1390+/-10	766+/-8	1564+/-9
	94	26	1998-12-14	1017+/-20	987+/-2	1203+/-4	802+/-4	2628+/-15
	101	26	1998-12-14	1016+/-20	986+/-2	1202+/-4	801+/-4	2450+/-14
	94	17	1999-03-30	978+/-49	988+/-4	1200+/-3	799+/-3	2644+/-14
	37	21	1999-03-30	972+/-54	982+/-3	1201+/-3	800+/-3	2212+/-10
	101	23	1999-06-09	894+/-17	980+/-1	1204+/-2	807+/-1	2419+/-6
	94	45	1999-09-23	826+/-18	982+/-6	1206+/-6	784+/-4	2547+/-26
factory	-	-	1999-11-11	1263	990	1147	831	1454
	37	12	2000-09-20	1247+/-6	981+/-4	1205+/-5	802+/-4	2200+/-24
03769								
factory	-	-	-	1220	979	1157	791	1419
	37	15	1998-08-20	1166+/-3	977+/-5	1189+/-3	801+/-3	1902+/-17
	37	26	1998-08-21	1171+/-8	982+/-4	1188+/-2	801+/-2	1904+/-11
	101	28	1999-06-09	1203+/-5	975+/-4	1167+/-5	798+/-3	2198+/-16
03770								
factory	-	-	-	1225	1002	1176	830	1819
	27	44	1998-11-12	1024+/-4	892+/-3	1389+/-3	801+/-1	2146+/-12

	94	30	1998-12-14	1213+/-3	993+/-6	1165+/-9	821+/-5	2835+/-7
	101	28	1998-12-14	1210+/-4	993+/-6	1166+/-8	820+/-5	2642+/-6
03772								
factory	-	-	-	1194	1000	1180	806	1843
	27	14	1998-11-24	942+/-8	868+/-4	1398+/-14	767+/-6	2166+/-31
	94	63	1998-12-14	1160+/-8	994+/-2	1166+/-6	804+/-3	2897+/-13
	101	62	1998-12-14	1157+/-8	994+/-1	1166+/-6	803+/-3	2700+/-10
	94	15	1999-03-30	1192+/-5	998+/-3	1169+/-4	810+/-2	3002+/-29
	37	10	1999-03-30	1190+/-5	991+/-3	1168+/-4	811+/-1	2508+/-23
	94	62	1999-09-23	1178+/-3	981+/-3	1155+/-4	793+/-2	2920+/-11
03773								
factory	-	-	-	1245	991	1195	818	1443
	37	18	1998-08-20	1238+/-7	988+/-4	1219+/-5	825+/-3	1929+/-11
	37	25	1998-08-21	1244+/-8	988+/-12	1218+/-10	824+/-7	1919+/-13
	27	81	1998-10-16	1099+/-17	912+/-12	1315+/-14	803+/-5	1745+/-19
	27	25	1998-11-24	993+/-2	862+/-2	1441+/-4	785+/-3	1757+/-6
	101	28	1999-06-09	1238+/-4	987+/-4	1198+/-3	827+/-2	2178+/-13
03775								
	101	37	1999-06-09	1179+/-5	982+/-4	1212+/-5	818+/-3	2578+/-22

SIMBAD Unit #				**440 nm**	**490 nm**	**560 nm**	**670 nm**	**870 nm**
972306						V_0+/-ΔV_0		
	37	13	1998-08-20	391290+/-719	477288+/-2026	404124+/-165	420995+/-2039	305421+/-414
	37	82	1998-08-21	388591+/-1703	479121+/-3755	406870+/-1305	421086+/-529	304820+/-388
	27	107	1998-10-16	346025+/-3581	449951+/-1968	383534+/-6934	454057+/-2460	300166+/-1816
	94	122	1998-12-14	388269+/-3922	473101+/-1242	394874+/-935	410455+/-2597	311944+/-702
	101	122	1998-12-14	387413+/-3911	472637+/-1195	394399+/-823	410233+/-2198	311458+/-681
	94	81	1999-09-23	376205+/-2369	464224+/-815	391526+/-854	416182+/-933	300000+/-2204
	101	56	1999-10-28	376820+/-4872	462637+/-1326	387034+/-1614	410887+/-1868	302475+/-1715
	106	16	2000-03-06	376901+/-1870	459570+/-1825	377800+/-1559	404798+/-1410	298829+/-1531
	37	10	2000-03-06	382815+/-2311	465574+/-2362	382168+/-1231	408538+/-961	301005+/-469
972309								
	94	12	2000-01-14	271780+/-946	385589+/-1000	331527+/-2112	402221+/-2603	315555+/-2890
	106	16	2000-03-06	287566+/-6927	413058+/-2193	342878+/-2870	411053+/-4870	294097+/-3823
	37	14	2000-03-06	297359+/-13257	418699+/-3152	344590+/-3315	415921+/-6602	298063+/-6980

(4/TP/NP76

Chapter 4

Variance Equations and Uncertainty Analysis for the Langley Technique

Mark Miller, Mary Jane Bartholomew, and R.M Reynolds

Department Environmental Science, Earth System Science Division, Brookhaven National Laboratory, Upton, New York

4.1 INTRODUCTION

To accurately interpret aerosol optical thickness (AOT) data, it is necessary to understand the sources of measurement uncertainty and their impact on the geophysical values produced by the radiometer. A preliminary analysis of the variance in the measurements of aerosol optical thickness, τ_λ, and the Angstrom exponent, α, is given in this report.

4.2 CALCULATION OF UNCERTAINTIES

From Beer's Law:

$$\ln(I_{\lambda N}) = -\tau_\lambda m + \ln(I_{\lambda T}) \qquad (4.1)$$

where $\tau_\lambda = \tau_{\lambda A} + \tau_{\lambda R} + \tau_{\lambda O}$. The subscripts A,R, and O indicate the contributions to the optical thickness made by aerosols, molecular scattering (Rayleigh) and ozone absorption. $I_{\lambda N}$ is the measured irradiance of the solar beam referenced to a plane that is normal to the solar beam and excluding all scattered diffuse light. $I_{\lambda T}$ is top-of-the-atmosphere irradiance referrenced to a plane along the normal to the solar beam. With the exception of m (under typical conditions), each term in (4.1) is wavelength dependent, as indicated by the subscript λ. The irradiance at the top of the atmosphere can be written as $I_{\lambda T} = I_{\lambda 0}\left(\frac{r_0}{r}\right)^2$, where $I_{\lambda 0}$ is the measured irradiance on a particular day of the year during which r_0 is the earth-sun distance and r is the current earth-sun distance. Substituting this relationship into (4.1) and solving for $\tau_{\lambda A}$:

$$\tau_{\lambda A} = \frac{1}{m}\left[\ln(I_{\lambda 0}) - 2\ln\left(\frac{r_0}{r}\right)\right] - \tau_{\lambda R} - \tau_{\lambda O} \qquad (4.2)$$

Using the Lambertian or Langley method (Shaw 1983; Harrison and Michalsky 1994a), a plot of m versus $\ln(I_{\lambda N})$ can be extrapolated to m=0 to derive $\ln(I_{\lambda T})$. The negative of the slope of the line is τ_λ. A power-law formalism is typically used to quantify the relationship between $\tau_{\lambda A}$ at different wavelengths. This power law is written as

$$\tau_{\lambda 1} = \tau_{\lambda 2}\left(\frac{\lambda_1}{\lambda_2}\right)^{-\alpha} \qquad (4.3)$$

where α is termed the angstrom exponent.

The variance associated with the measurement of τ using the Langley method can be expressed in the form of a variance equation for (4.2), which is given by

$$\sigma^2_{\tau_{\lambda A}} = \left(\frac{1}{m}\right)^2\left[\sigma^2_{\ln(I_{\lambda 0})} + \sigma^2_{\ln(I_{\lambda T})} + 2\sigma^2_{\ln\left(\frac{r_0}{r}\right)}\right] + \sigma^2_{\tau_{\lambda R}} + \sigma^2_{\tau_{\lambda O}} \qquad (4.4)$$

It is assumed that $2\sigma^2_{\ln\left(\frac{r_0}{r}\right)} \cong 0$ since these values do not fluctuate on the same scale as $\tau_{\lambda A}$. Furthermore, $\sigma^2_{\tau_{\lambda R}}$ depends on surface pressure measurements and is at least an order of magnitude less than other variance terms and can be neglected. The ozone optical thickness variance, $\sigma^2_{\tau_{\lambda O}}$, is only important in the vicinity of 660 nm and will be neglected here. This leaves

$$\sigma^2_{\tau_{\lambda M}} = \left(\frac{1}{m}\right)^2 \left[\sigma^2_{\ln(I_{\lambda 0})} + \sigma^2_{\ln(I_{\lambda N})}\right], \qquad (4.5)$$

which suggests that $\sigma^2_{\tau_{\lambda M}}$ is the largest at small zenith angles (when the sun is highest in the sky and m approaches unity). It can be shown that

$$\sigma_{\ln(x)} = \frac{\sigma_x}{x} \qquad (4.6)$$

so (4.5) can be written as

$$\sigma^2_{\tau_\lambda} = \left(\frac{1}{m}\right)^2 \left[\left(\frac{\sigma^2_{I_{\lambda 0}}}{I_{\lambda 0}}\right)^2 + \left(\frac{\sigma^2_{I_{\lambda N}}}{I_{\lambda N}}\right)^2\right] \qquad (4.7)$$

Hence, the variance in the measurement of τ is a result of the sum of the variances in the measurements of $I_{\lambda 0}$ and $I_{\lambda N}$. Similarly, the variance equation for α is

$$\sigma^2_\alpha = \frac{\left[\left(\frac{\sigma^2_{\tau_{\lambda 1}}}{\tau_{\lambda 1}}\right)^2 + \left(\frac{\sigma^2_{\tau_{\lambda 2}}}{\tau_{\lambda 2}}\right)^2\right]}{\left(\ln\left(\frac{\lambda_1}{\lambda_2}\right)\right)^2} \qquad (4.8)$$

which shows that σ^2_α is inversely proportional to the square of the difference between the two wavelengths that bound the calculation of α. The greater the separation between these two wavelengths, the less the varaince, or uncertainty, in the determination of α.

These variances are the result of several instrument-related factors, which are detailed below. These factors typically contribute variance as a percentage of the absolute measurement, so

$$\sigma_{\lambda x} = C_{I_{\lambda x}} I_{\lambda x} \qquad (4.9)$$

where C_{I_x} is the estimated percent accuracy of the measurement of I_x. Accordingly, (4.8) can be written as

$$\sigma^2_\tau = \left(\frac{1}{m}\right)^2 \left[C^2_{I_{\lambda 0}} + C^2_{I_{\lambda N}}\right] \qquad (4.10)$$

Thus, the variance in measurements of τ results from the sum of the squares of the percentage accuracy in measurements of $I_{\lambda 0}$ and $I_{\lambda N}$ and is inversely proportional to the square of the air mass, m. This suggests that measurements made at higher values of air mass have inherently less variance and are more accurate. Of course, (4.10) can be substituted into (4.8) to yield

$$\sigma^2_\alpha = \frac{\left[\left(\frac{C^2_{I_{\lambda 0}} + C^2_{I_{\lambda N}}}{\tau^2_{\lambda 0}}\right) + \left(\frac{C^2_{I_{\lambda 0}} + C^2_{I_{\lambda N}}}{\tau^2_{\lambda 2 N}}\right)\right]^{1/2}}{\left(m^2 \ln\left(\frac{\lambda_1}{\lambda_2}\right)\right)^2} \qquad (4.11)$$

which can be used to evaluate the uncertainty of angstrom exponent measurements.

The variance equations (4.10) and (4.11) represent a rough estimate of the uncertainties associated with the measurements of τ and α, since they include the assumption $\sigma_{\lambda x} = C_{I_{\lambda x}} I_{\lambda x}$, which is simplistic. Strictly speaking, (4.7) and (4.8) must be used to provide the best possible estimates of variance, although (4.10) and (4.11) are useful to illustrate how the variance analysis technique be used as a quality control metric for sun photometers, both shadow-band and oriented varieties. Placing a threshold on the allowable uncertainties of τ and α reduces the scatter of data points by eliminating observations for which the uncertainty associated with the Langley technique or instrument deficiencies is unacceptably large. The terms in (4.10) and (4.11) can be computed from the data, as can the terms in (4.7) and (4.8) for a more rigorous analysis, and each individual data point can be scrutinized to ensure that its uncertainty is not so large as to make the measurement meaningless.

An example of the use of (4.10) and (4.11) as quality control metrics is shown in Figures (4.1) and (4.2). These plots show τ versus α in several different aerosol regimes over the ocean. Note that α is computed for different wavelength ranges. These data were collected with the Brookhaven National Laboratory fast-rotating, shadow-band radiometer and the nature of the aerosol determined by chemical analysis. The difference between Figures (4.1) and (4.2) is that the latter has been subject to data rejection on the basis of equations (4.10) and (4.11). In Figure (4.2), the variance (uncertainty) in τ must be less than 0.05 and the variance (uncertainty) in α must be less than 0.3. These thresholds are determined subjectively based on experience. Note that the impact of the uncertainty threshold is to greatly reduce the scatter of the data in Figure (4.2) by eliminating points

with unacceptably large error bars. Most importantly, the various aerosol regimes are clearly separable in Figure (4.2) while they are not in Figure (4.1). It should be emphasized that these error bars include the inherent uncertainty in Langley technique itself, as well as instrument uncertainty. The magnitude of the latter, the instrument uncertainty, is being further bounded by field and laboratory measurements at the time of this report.

In essence, the atmospheric correction algorithm attempts to infer the results of Figure (4.1a) from Figure (4.1b). That is, the power-law extrapolation of the data in Figure (4.1b), using 660 nm as a surrogate for the 765 nm channel in the SeaWiFS sensor, should ideally produce the results in Figure (4.1a). It is clear that application of a power-law extrapolation to the data in Figure (4.1b) would not appear to produce a graph that looks like Figure (4.1a). The basic shape and configuration of Figure (4.1b) is different the Figure (4.1a), although this difference is largely due to measurement uncertainty. When data points that contain unacceptable uncertainty are rejected, the basic shape and configuration of Figure (4.2b) is actually quite similar to that in Figure (4.2a), which implies that a power-law atmospheric correction is possible when the measurement uncertainty is minimized. In summary, these analyses show that the uncertainty in the Langley technique itself must be considered if satellite atmospheric correction validation data are collected with traditional sun photometers and shadow-band radiometers.

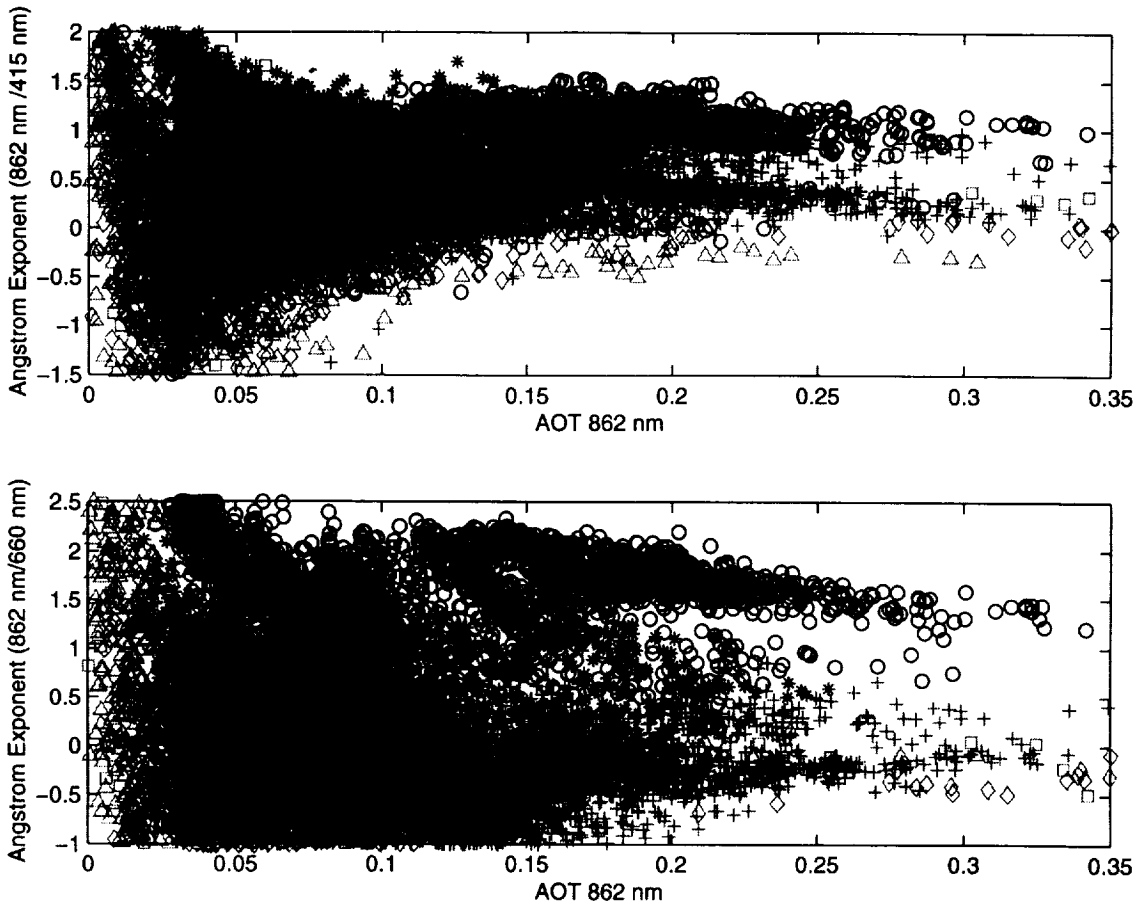

Figure 4.1. Shadow-band radiometer data showing the aerosol optical thickness at 865 nm versus the Angstrom exponent for the two wavelengths listed on the y-axis. Several different aerosol regimes are depicted.

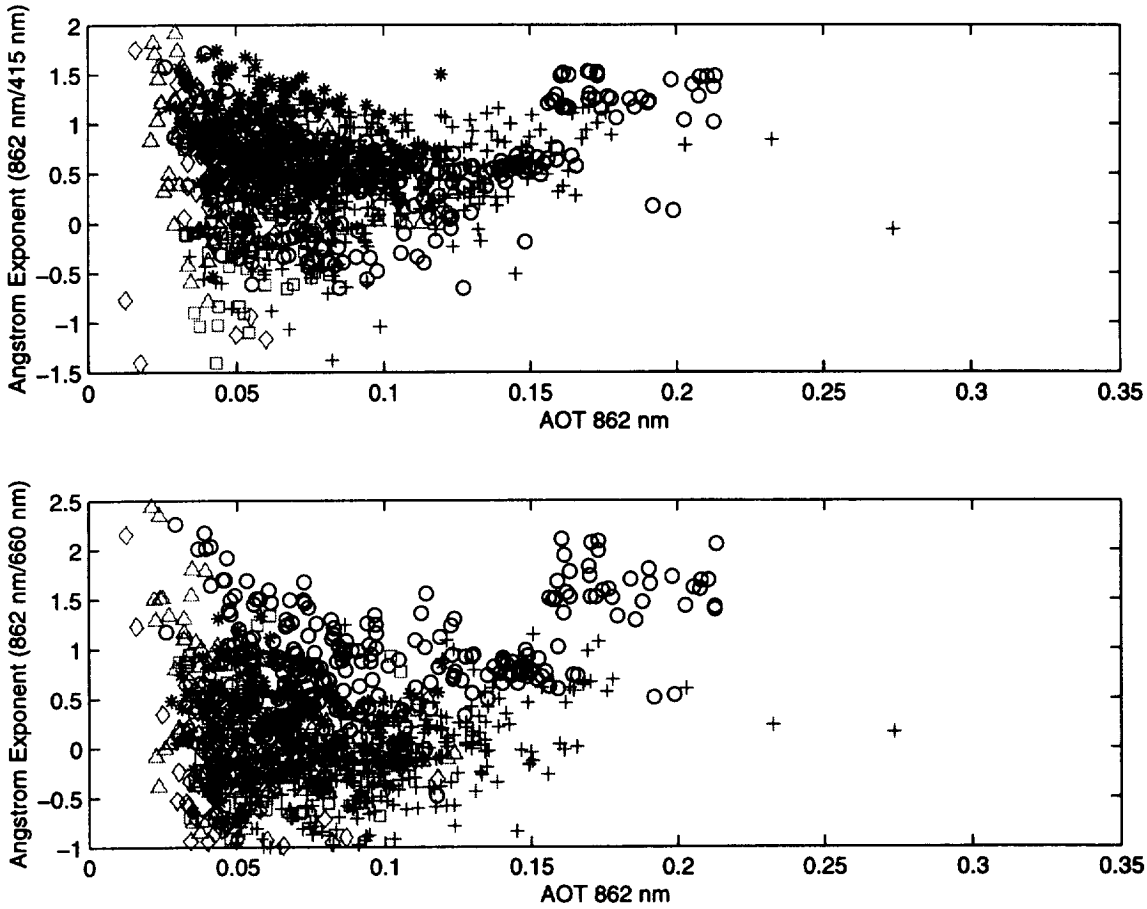

Figure 4.2. As in Figure 4.1, but after filtering on the basis of measurement uncertainty.

Chapter 5

Sun and Sky Radiance Measurements and Data Analysis Protocols

Robert Frouin[1], Brent Holben[2], Mark Miller[3], Christophe Pietras[4], John Porter[5] and Ken Voss[6]

[1]*Scripps Institution of Oceanography, University of California, San Diego, California*
[2]*Biospheric Sciences Branch, NASA Goddard Space Flight Center, Greenbelt, Maryland*
[3]*Department Environmental Science, Earth System Science Division, Brookhaven National Laboratory, Upton, New York*
[4]*SAIC General Sciences Corporation, Beltsville, Maryland*
[5]*School of Ocean & Earth Science & Technology, University of Hawaii, Hawaii*
[6]*Physics Department, University of Miami, Florida*

5.1 INTRODUCTION

This chapter is concerned with two types of radiometric measurements essential to verify atmospheric correction algorithms and to calibrate vicariously satellite ocean color sensors. The first type is a photometric measurement of the direct solar beam to determine the optical thickness of the atmosphere. The intensity of the solar beam can be measured directly, or obtained indirectly from measurements of diffuse global upper hemispheric irradiance. The second type is a measurement of the solar aureole and sky radiance distribution using a CCD camera, or a scanning radiometer viewing in and perpendicular to the solar principal plane.

From the two types of measurements, the optical properties of aerosols, highly variable in space and time, can be derived. Because of the high variability, the aerosol properties should be known at the time of satellite overpass. Atmospheric optics measurements, however, are not easy to perform at sea, from a ship or any platform. This complicates the measurement protocols and data analysis. Some instrumentation cannot be deployed at sea, and is limited to island and coastal sites. In the following, measurement protocols are described for radiometers commonly used to measure direct atmospheric transmittance and sky radiance, namely standard sun photometers, fast-rotating shadow-band radiometers, automated sky scanning systems, and CCD cameras. Methods and procedures to analyze and quality control the data are discussed, as well as proper measurement strategies for evaluation of atmospheric correction algorithms and satellite-derived ocean color.

5.2 AUTOMATIC SUN PHOTOMETER AND SKY RADIANCE SCANNING SYSTEMS

The technology of ground-based atmospheric aerosol measurements using sun photometry has changed substantially since Volz (1959) introduced the first hand-held analog instrument almost four decades ago. Modern digital units of laboratory quality and field hardiness collect data more accurately and quickly and are often equipped for onboard processing (Schmid et al., 1997; Ehsani, 1998, Forgan, 1994; and Morys et al., 1998). The method used remains the same, i.e., a detector measures through a spectral filter the extinction of direct beam solar radiation according to the Beer-Lambert-Bouguer law:

$$V(\lambda) = V_o(\lambda)\left(\frac{d_o}{d}\right)^2 \exp\left[-\left(\tau(\lambda)M\right)\right]t_g(\lambda), \quad (5.1)$$

where $V(\lambda)$ is the measured digital voltage, $V_0(\lambda)$ is the extra-terrestrial voltage, M is the optical air mass, $\tau(\lambda)$ is the total optical depth, λ is wavelength, d and d_o are respectively the actual and average earth-sun distances, and $t_g(\lambda)$ is the transmission of absorbing gases. The total optical

depth is the sum of the Rayleigh and aerosol optical depth.

The earth-sun distance correction is calculated using the approximation

$$\left(\frac{d_o}{d}\right)^2 = 1 + 0.034\cos\frac{2\pi \cdot J}{365} \qquad (5.2)$$

where J is the number of the day of the year (Iqbal 1983).

Air mass is a function of the sun zenith angle. Currently, the same value of air mass is used for Rayleigh, ozone, and aerosol factors. Air mass is calculated as

$$M = \left\{\cos\frac{\pi\theta_o}{180^o} + 0.15*(93.885-\theta_o)^{-1.253}\right\}^{-1}, \quad (5.3)$$

where the sun zenith angle θ_o is expressed in degrees.

Sky-scanning spectral radiometers that measure the spectral sky radiance at known angular distances from the sun have expanded the aerosol knowledge base. They provide, through inversion of the sky radiance, aerosol physical properties, such as size distribution, and optical properties, such as the aerosol scattering phase function (Nakajima et al., 1983, 1996; Tanré et al., 1988; Shiobara et al., 1991; Kaufman et al., 1994; Dubovik et al., 2000; and Dubovik and King, 2000). The inversion technique to calculate these aerosol properties requires precise aureole measurements near the solar disk and good stray-light rejection. Historically these systems are cumbersome, not weather hardy and expensive. The CIMEL and PREDE (French and Japanese manufacturers respectively) sun and sky scanning spectral radiometers overcome most of such limitations, providing retrievals of aerosol and water vapor abundance from direct sun measurements, and of aerosol properties from spectral sky radiance measurements. Since the measurements are directional and represent conditions of the total column atmosphere, they are directly applicable to satellite and airborne observations, as well as to studies of atmospheric processes. Owing to a sophisticated tracking system with fast responding motors, the PREDE can be installed onboard a ship, or other moving platform, to monitor aerosol optical properties at sea. In the following, we focus on the CIMEL system, since the measurement protocols are similar for both CIMEL and PREDE systems.

Description

The CIMEL Electronique 318A spectral radiometer, manufactured in Paris, France, is a solar powered, weather hardy, robotically pointed sun and sky spectral radiometer. At each wavelength, this instrument has approximately a 1.2° field-of-view (full angle) and filtered solar aureole and sky radiance. The 33 cm collimators were designed for 10^{-5} stray-light rejection for measurements of the aureole 3° from the sun. The robot mounted sensor head is pointed at nadir when idle to prevent contamination of the optical windows from rain and foreign particles. The sun/aureole collimator is protected by a quartz window, allowing observation with a ultraviolet enhanced silicon detector with sufficient signal-to-noise for spectral observations between 300 and 1020 nm. The sky collimator has the same 1.2° field of view, but uses an order of magnitude larger aperture-lens system to improve dynamic range for measuring the sky radiance. The components of the sensor head are sealed from moisture and desiccated to prevent damage to the electrical components and interference filters. Eight ion assisted deposition interference filters are located in a filter wheel rotated by a direct drive stepping motor. A thermistor measures the temperature of the detector, allowing compensation for any temperature dependence in the silicon detector.

A polarization model of the CE-318 is also used in SIMBIOS. This version executes the same measurement protocol as the standard model, but makes additional hourly measurements of polarized sky radiance at 870 nm in the solar principal plane (Table 5.1 and 5.2).

Installation

The installation procedures for the CIMEL instrument are summarized below. More detailed information is available from the AERONET web page (http://aeronet.gsfc.nasa.gov).

The site should have a clear horizon and be representative of the regional aerosol regime. The basic assembly is relatively simple to mount. The cables are labeled clearly and most fit only in one place. Once the robot is assembled, it should be oriented so the zenith motor casing is pointing roughly east (the metal claw to which the sensor head is attached, then points to the west). The round connector end of the data cable should be attached to the sensor head, and the flat connector should be plugged into the white CIMEL control box. Strap the sensor head to the robot metal claw using the silver metal band. Make sure that the face of the

sensor head is flush with the edge of the metal claw. Also, ensure that the long axis of the collimator cross-section is perpendicular to the axis of the zenith motor casing and claw. Verify that the robot itself is level. Do not use the embedded bubble level on top of the robot. Place the supplied bubble level on top of the flat ledge of the central robot tubular body (below the sensor head motor) This should be level in both the N/S and E/W axes. Verify that the CIMEL control box "TIME" and "DATE" are correct, i.e., that they agree with the VITEL transmitter clock. If the Time or Date is wrong, the CIMEL will not find the sun on a "GOSUN" command.

Next, put the CIMEL in manual mode using the white control box display screen. In Manual mode, the main screen reads: "PW MAN SCN VIEW". Do a "PARK" procedure. When "PARK" is complete the sensor head collimator should be pointing down, perpendicular to the ground. Place the bubble level on the top of the metal claw arm and verify that this is level. If not, loosen the zenith bolt's hex nut (below the permanent bubble level on the top of the robot) and level it by rotating the zenith motor casing with your hand. Re-tighten the zenith nut tightly. Important: Perform another "PARK" procedure, or two, and make sure it is in fact level.

Using the right 2 buttons, change the display to read "GOSUN". Select "GO" to initiate. The sensor head should point to the sun. The hole at the top of the collimator should allow the sunlight to illuminate the marker spot at the base of the collimator. When the bright spot is on the mark, the instrument is aligned. If it is off to the left or right, rotate the robot base to align it. After you rotate the robot, you will need to verify that the robot is still level as before. Park the instrument and perform another "GOSUN" to check that the alignment is still good. If not, ensure that the robot is level, and that the sensor head is level when manually parked. One note: when you level the sensor head and do a "GOSUN", repeat this process a few times to be sure of the alignment. The first "GOSUN" after leveling is often not correct, because moving the sensor head while leveling can temporarily offset the robot's zeroing point. Re-parking the sensor and doing a second "GOSUN" should yield a more accurate alignment. Repeat this procedure until the alignment remains accurate and consistent on repetition.

Press "PW" then increment to 4, and place the instrument in "AUTO" mode. The main "AUTO" mode display should read: "PW AUTORUN VIEW". The CIMEL should be left in this mode in order to perform automatic measurement sequences. The VITEL transmitter has a multi-level menu with "TIME DATE" etc in top level, and sub categories below each top-level item. The exact menu structure varies with software version (2.01, 2.9, and 2.11). Refer to the version most similar to your particular transmitter. One may operate the VITEL display by using the control buttons. To initiate an action, press the "SET-UP" button, then press the "SCROLL" button repeatedly to view the categories in the current menu level. To choose any subcategory, press the "SELECT" button when the desired feature is shown in the display window. To change a parameter use the right 2 buttons "CHANGE" and "ENTER"'. At any time, one may return to the previous (higher) menu level by pressing the "SET-UP" button.

Measurement Protocols

The radiometer makes only two basic measurements, either direct solar flux, or sky radiance. Each type of measurement involves several programmed sequences.

Direct sun measurements are made in eight spectral bands distributed between 340 and 1020 nm (440, 670, 870, 940 and 1020 nm are standard). Each measurement requires approximately 10 seconds. A sequence of three such measurements are taken 30 seconds apart creating a triplet observation per wavelength. Triplet observations are made during morning and afternoon Langley calibration sequences and at standard 15-minute intervals in between (Table 5.1). The time variation of clouds is typically much greater than that of aerosols, and therefore significant variation in the triplets may be used to screen cloud contaminated measurements from the data. Variability over the 15-minute interval also allows another check for cloud contamination at a lower frequency. Sky measurements are performed at 440, 670, 870 and 1020 nm (Table 5.1). A single spectral measurement sequence (Langley sky) is made immediately after the Langley air mass direct sun measurement, with the sensor pointed 20° from the sun. This is used to assess the stability of the Langley plot analysis (O'Neill *et al.* 1984). Two basic sky observation sequences are made, "almucantar" and "principal plane". The objective of these sequences is to retrieve size distribution, phase function and aerosol optical thickness (AOT). This is approached by acquiring aureole and sky radiance observations spanning a large range of scattering angles, relative to the sun's direction, assuming a constant aerosol profile.

An almucantar is a series of measurements taken at the same sun elevation for specified

azimuth angles relative to the Sun position. The range of scattering angles decrease as the solar zenith angle decreases, thus almucantar sequences made at an optical air mass of 2, or more, achieve scattering angles of 120°, or larger. Scattering angles of 120° are typical of many sun-synchronous viewing satellites, and thus a measure of the satellite path radiance is approximated from the ground station. During an almucantar measurement, observations from a single channel are made in a sweep at a constant elevation angle across the solar disk and continue through 360° of azimuth in about 40 seconds (Table 11.2). This is repeated for each channel to complete an almucantar sequence. A direct sun observation is also made during each spectral almucantar sequence. More than four almucantar sequences are made daily at optical airmasses of 4, 3, 2 and 1.7, both morning and afternoon. An almucantar sequence is also made hourly between 9 AM and 3 PM local solar time for the standard instrument and skipping only the noon almucantar for the polarization instrument. The standard principal plane sky radiance measurement sequence is similar to the almucantar sequence, but the sensor scans in the principal plane of the sun, and therefore all angular distances from the sun are scattering angles, regardless of solar zenith angle. This measurement pointing sequence begins with a sun observation, moves 6° below the solar disk then sweeps through the sun's principal plane, taking about 30 seconds for each of the four spectral bands (Table 5.2). Principal plane observations are made hourly when the optical airmass is less than 2 to minimize the variations in radiance due to the change in optical airmass.

Polarization measurements of the sky at 870 nm are an option with this instrument. The sequence is made in the principal plane at 5° increments between zenith angles of –85° and +85°. The configuration of the filter wheel requires that a near-IR polarization sheet be attached to the filter wheel. Three spectrally matched 870 nm filters are positioned in the filter wheel exactly 120° apart. Each angular observation is a measurement of the three polarization filter positions. An observation takes approximately 5 seconds and the entire sequence about 3 minutes. This sequence occurs immediately after the standard measurement sequence in the principal plane.

Data Analysis

We are following the procedures established for the AERONET program (Holben et al, 1998) (Table 5.3). These algorithms impose a processing standardization on all of the data taken in the network, facilitating comparison of spatial and temporal data between instruments.

Table 5.1. Measurement sequences of the CIMEL Sun/Sky scanning spectral radiometer.

	Spectral Range nm	**Target**	**No. Obs.**	**Obs. Interval**	**Application**
BASIC DIRECT SUN	340 to 1020	Sun	1 each λ	~ 8 sec. for. 8 λ	AOT, Pw, α
Triplet Observation	340 to 1020	Sun	Three direct sun	3 @ 30 sec. apart, 1 min total	AOT, Pw, α & cloud screening
Standard Measurement Sequence	340 to 1020	Sun	Variable: depends on day length	Ea. 15 min m=2 AM to m=2 PM	AOT, Pw, α
Langley	340 to 1020	Sun	16, am & PM between m 7 & 2	m=7 - 5, incr of.5 m m=5 - 2, incr. of.25	Langley, Cal., AOT, Pw, α
BASIC SKY	440 to 1020	Sky	1 each λ	none	Sky Radiance
Langley sky	440 to 1020	Sky	16 between m 7 & 2	m=7 - 5,.5; m=5- 2,.25	Stability of Lngly Plot
Almucantar	440 to 1020	Sky	72 (Table 2)	>8/day: m= 4, 3, 2, 1.7 hrly 9AM to 3PM	Size Dist. and P(θ), AOT, α
Polarization	870	Sky	42 (Table 2)	hourly m=3 AM to m=3 PM	Size Dist. and P(θ)
Principal Plane	440 to 1020	Sky	42 (Table 2)	hourly m=3 am to m=3 PM	Size Dist. and P(θ) AOT, α

The archival system allows the SIMBIOS community to access either the raw or processed data via internet for examination, analysis and/or reprocessing, as needed, through the AERONET web page: aeronet.gsfc.nasa.gov:8080. The algorithms, inputs, corrections, and models used in computing the aerosol optical thickness, precipitable water (Pw), spectral irradiance, and sky radiance inversions are referenced in Table 15.3. The algorithms comprise two principal categories; time dependent retrievals such as AOT and Pw, and sky radiance retrievals such as size distribution, asymmetry parameter, single scattering albedo and complex index of refraction. As new and improved approaches and models are accepted within the community the processing may be applied uniformly to the network-wide database.

Sky radiance Inversion Products

Optical properties of the aerosol in the atmospheric column are retrieved by two inversion algorithms: that of Nakajima et al. (1983, 1996) and the new algorithm developed by the AERONET Project (Dubovik and King 2000; Dubovik *et al.* 2000).

a) Inversions by the Nakajima et al.'s (1983, 1996) algorithms

The code inverts sky radiance in two ways:

1. simultaneously at four wavelengths (440; 670; 870 and 1020 nm) in the aureole angular range (scattering angle between 2.8^0 and 40^0 ;

2. separately at each of four wavelengths (440; 670; 870 and 1020 nm) in the whole solar almucantar (scattering angle greater than 2.8^0) - -option "single channel inversion".

The inversion assumptions are that aerosol particles are homogeneous spheres with a fixed index of refraction: n (λ) = 1.45, k(λ) = 0.005. The retrieved variables are: $\frac{dV(r)}{d\ln r}$ (in $\mu m^{-3}/\mu m^{-2}$), the volume particle size distribution in range of sizes: 0.057 μm < r < 8.76 μm, the scattering optical thickness at 440,670,870,1020nm, and the phase function at 440, 670, 870 and 1020nm (including an asymmetry parameter).

b) Inversions by the new AERONET code (Dubovik and King 2000; Dubovik et al. *2000)*

The code inverts $\tau_a(\lambda)$ and sky radiances simultaneously at four wavelengths (440; 670; 870 and 1020 nm) in the whole solar almucantar (scattering angles greater than 2.8°). Aerosols are assumed to be homogeneous spheres, but the index of refraction is not fixed.

Table 5.2. Almucantar and Principal Plane sequences for the standard and polarization instruments.

	Sun	Sky (°)
ALMUCANTAR Azimuth angle relative to sun	0°	6.0, 5.0, 4.5, 4.0, 3.5, 3.0, 2.5, 2.0, -2.0,-2.5, -3.0, -3.5, -4.0, -4.5, -5.0, -6.0, -8.0, -10.0, -12.0, -14.0, -16.0, -18.0, -20.0, -25.0, -30.0, -35.0, -40.0, -45.0, -50.0, -60.0, -70.0, -80.0, -90.0, -100.0, -110.0, -120.0, -130.0, -140.0, -160.0, -180.0 Duplicate above sequence for a complete counter clockwise rotation to –6
PRINCIPAL PLANE: Standard Scattering Angle from sun (negative is below the sun)	0°	-6.0, -5.0, -4.5, -4.0, -3.5, -3.0, -2.5, -2.0, 2.0, 2.5, 3.0, 3.5, 4.0, 4.5, 5.0, 6.0, 8.0, 10.0, 12.0, 14.0, 16.0, 18.0, 20.0, 25.0, 30.0, 35.0, 40.0, 45.0, 50.0, 60.0, 70.0, 80.0, 90.0, 100.0, 110.0, 120.0, 130.0, 140.0
PRINCIPAL PLANE: Polarization Scattering Angle from sun (negative is in the anti solar direction)	-	-85.0, -80.0, -75, -70, -65.0, -60.0, -55.0, -50.0, -45.0, -40.0, -35.0, -30.0, -25.0, -20.0, -15.0, -10.0, -5.0, 5.0, 10.0, 15.0, 20.0, 25.0, 30.0, 35.0, 40.0, 45.0, 50.0, 55.0, 60.0, 65.0, 70.0, 75.0, 80.0, 85.0

Table 5.3 Procedure of the AERONET Program

Variable, algorithm or correction	Comments	References
Basic Computations		
Rayleigh Optical Depth, τ_r refractive index of air depolarization factor	Input elevation in m	Penndorf, 1957 Edlen, 1966 Young, 1980 Burcholtz, 1995
Solar Zenith Angle, θo		Michalsky, 1988
Earth sun distance, d		Iqbal, 1983
Ozone amount, O_3	Table lookup by 5° lat. long.	London et al., 1976
Aerosol optical air mass, m_a		Kasten and Young, 1989
Rayleigh optical air mass, m_r		Kasten and Young, 1989
O_3optical air mass, m_o		Komhyr et al., 1989
Corrections		
Temperature, T	~0.25%/°C for 1020 nm specific for each inst.	Hamamatsu Inc. and Lab measurements
Water Vapor for 1020 AOT	from Pw retrieval, Lowtran	Kneizys et al, 1988
Rayleigh, all wavelengths	from elevation	
O_3 abs. coef. $\lambda > 350$ nm		Vigroux, 1953
O_3 abs. coef. $\lambda < 350$ nm		Bass and Paur, 1984
Time, t	CIMEL, UTC, DAPS time stamps, ±1 second	Refer to Homepage
Retrievals		
Spectral direct Sun AOT,Langley Plots	Beer's Law	Shaw, 1983
Pw: (a, k, Vo)	Modified Langley	Bruegge et al., 1992; Reagan et al., 1992
Size Dist., Phase function	From spectral sky radiance	Nakajima et al., 1983 Dubovik and King, 2000
Procedures		
Cloud Screening	Thresholds, λ AOT & t	Smirnov et al., 2000
Climatology, Direct Sun	AOT, Pw, Wavelength Exp.	Refer to Homepage
Climatology, Sky	Size Dist., Phase function, g	Refer to Homepage

The retrieved variables are $\frac{dV(r)}{d\ln r}$ (in $\mu m^3/\mu m^{-2}$), the volume particle size distribution in the range of sizes 0.05 μm $< r <$ 15 μm, and the volume concentration, volume mean radius, standard deviation, and effective radius for total (t), fine (f), and coarse (c) modes.

Note that the fine and coarse mode variables can be used only if the retrieved $\frac{dV(r)}{\ln r}$ is bi-modal. There is no automatic check for bi-modality. Also retrieved are the real and imaginary parts of the complex refractive index, $m(\lambda) = n(\lambda) - i\,k(\lambda)$, ($1.33 < n(\lambda) < 1.6$; $0.0005 < k(\lambda) < 0.5$) at 440,670,870, and 1020nm, the single scattering albedo, and the phase function (including its asymmetry parameter) at 440, 670, 870, and 1020 nm. It is assumed that particles in the range 0.05-0.6 μm are fine mode and those in the range 0.6-15 μm are coarse mode aerosols (Dubovik et al., 2000). This definition is not completely correct in all size distributions. Nevertheless, experience has shown it to hold true in the majority of practical cases.

Quality Control

The AERONET $\tau_a(\lambda)$ quality assured data are cloud screened following the methodology of Smirnov et al. (2000), and here we present just a brief outline of the procedure. The principal filters used for the cloud screening are based on temporal variability of the $\tau_a(\lambda)$, with the assumption being that greater temporal variance in τ_a is due to the presence of clouds. The first filter is a check of the variability of the three τ_a values measured within a one-minute period. If the difference between

minimum and maximum $\tau_a(\lambda)$ within this one minute interval is greater than 0.02 (for τ_a less than 0.667) or $0.03\tau_a$ (for τ_a greater than 0.667) then the measurement is identified as cloud contaminated. Then the time series of the remaining $\tau_a(\lambda)$ are analyzed for the presence of rapid changes or spikes in the data. A filter based on the second derivative of the logarithm of $\tau_a(\lambda)$ as a function of time is employed to identify rapid variations which are then filtered as observations affected by cloud. Other secondary order cloud screening and data quality checks are also made and these are described in detail in Smirnov et al. (2000). Unscreened data is fully available from the AERONET homepage. Automatic cloud screening of the almucantar and principal plane data is done by checking the distributions of data about the solar disc for symmetry and smoothness.

5.3 SKY RADIANCE DISTRIBUTION CAMERA SYSTEMS

Camera systems for sky radiance distribution are useful to collect the entire hemisphere of sky radiance data in a quick manner. The resulting data images usually contain the sun, so that the measurement geometry can be determined accurately and unambiguously. Also images can be checked for cloud contamination and other measurement artifacts more easily than can be done with data from scanning systems. The limitation of camera systems is that the dynamic range of the whole scene must be contained in each image. Therefore, the camera system must have large dynamic range and there has to be a method of attenuating the direct sunlight before it strikes the imaging optics. To get a complete sky radiance distribution, including the solar aureole, it may be necessary to have an auxiliary system to measure the sky radiance near the sun (Ritter and Voss, 2000).

In addition, a sky radiance system, fitted with polarizers, can measure the Stokes parameters dealing with linear polarization (Voss and Liu, 1997). These additional parameters are useful for investigating the polarization properties of the atmospheric aerosols, and improving the aerosol optical models.

One of the most important areas of the sky radiance distribution to measure is the area near the horizon, opposite the sun, in the principal plane (the plane containing the sun and the zenith direction). This portion of the sky contains information on the large scattering angle portion of the atmospheric aerosol phase function, and is very important for determining the aerosol optical properties relevant to atmospheric correction for ocean color satellites.

The second very important region of the sky is the solar aureole, the region near the sun. Because the aerosol scattering phase function is strongly peaked in the forward direction, information in this region is important in determining the aerosol single scattering albedo. Techniques for converting sky radiance measurements to aerosol properties have been described in Wang and Gordon (1993), Gordon and Zhang (1995) and Zhang and Gordon (1997a, b). An example of a camera system for sky radiance distribution is described in Voss and Zibordi (1989). The system described has been upgraded, for greater dynamic range, with a cooled CCD array. The basic system consists of a fisheye lens, a spectral/polarization filter changer, and a digital camera. To block direct sunlight from hitting the array, an occulter is manually adjusted to shadow the fish-eye lens. The size of the occulter is approximately $\pm$ 20° of the almucantar when the sun is at 60° zenith angle; the effect of the occulter is obvious in data images shown in Liu and Voss (1997). Four spectral filters select the wavelength range to be measured. Polarization filters are used to collect 3 planes of polarization in data images. These images can be combined to determine the linear polarization stokes vectors.

Measurement Protocols

Obviously the first order requirement is that the field of view of the camera system be as unobstructed as possible, and that the measurement site be located in an appropriate place with respect to the ships stack exhaust. If the whole field of view cannot be clear (as is usually the case), then one should try for a clear hemisphere, where data between obstructions in the other hemisphere can be used for checking the sky symmetry.

As the desired objective is the aerosol scattering parameters, the sky must also be cloud free. Clouds cause two problems. The first is easy to detect and is the direct effect of having the bright cloud in the scene (in particular on the almucantar or principle plane). Almost any cloud will overwhelm the effect of aerosols in determining the sky radiance. This effect of clouds is usually quite evident in the sky radiance image. The second problem is the indirect effect of clouds, while not directly causing a problem, shadowing aerosols and reducing the skylight caused by aerosol scattering.

This second effect is more difficult to handle and places a more stringent requirement on the state of cloudiness during a measurement sequence. This effect can often be quite visible when the atmospheric aerosol loading is high, causing light beams to be evident in the aerosol layer. For these reasons, measurements with clouds present should be avoided if at all possible.

The maximum scattering angles existing in the sky radiance distribution occur near the horizon in the principle plane opposite the sun. For a given solar zenith angle, the maximum scattering angle is given by adding $\pi/2$ to the solar zenith angle. Since knowledge of the aerosol phase function at large scattering angles is important for the atmospheric correction process, measurements of the sky radiance distribution should be taken when the sun is at large zenith angles. The optimum angle is a compromise between getting large scattering angles and working too close to the horizon where multiple scattering effects are large (because of long optical paths through the atmosphere). A solar zenith angle of 60^0 has been chosen as optimum, because of these constraints. Concurrent with the sky radiance measurements, it is important to measure the aerosol optical depth. By combining the aerosol optical depth and sky radiance distribution, the aerosol scattering properties can be determined, together with the single scattering albedo of the aerosols (Wang and Gordon, 1993; Gordon and Zhang, 1995; Zhang and Gordon, 1997a).

Data Analysis Protocols

Data reduction of the sky radiance data is very straightforward, and is described in Voss and Zibordi (1989). Basically with camera images, the data reduction process consists of simple image processing. Each image is multiplied by an absolute calibration factor and by an image that corrects for camera lens roll-off. This last factor is very important with a fisheye lens, as the important portion of the image is near the edge where the roll-off can become very significant. Once the image has been converted to radiometric data, specific areas can be selected for further analysis. In particular the almucantar and principal plane can easily be extracted for use in inversion routines.

Reduction of the sky radiance data to get the polarization properties is slightly more complicated. The current method is described in Voss and Liu (1997). Basically the Mueller matrix of the camera system is described as interacting with the Stokes vector of the skylight. There are three orientations of a linear polarizer in the system providing three separate Mueller matrices describing the camera system. For each sky direction (a pixel in the camera images), these Mueller matrices and the resultant intensities measured by the camera form a set of simultaneous equations with the unknowns being the sky Stokes vectors. For each pixel, these equations are inverted to obtain the Stokes vector of the skylight. While these images have been evaluated qualitatively (Liu and Voss, 1997), work is currently being done to do more quantitative inversions following the methods of Zhang and Gordon (1997b).

5.4 HAND-HELD SUN PHOTOMETERS

These instruments offer the simplest and most cost-effective means to collect data on aerosol optical thickness at sea. They are based on the measurement of the solar beam intensity, and therefore, the direct atmospheric transmittance. From this transmittance, after proper correction for attenuation by air molecules, the aerosol optical thickness may be obtained (Equation 5.1). The technique is straightforward in principle. It is difficult for an observer to point the photometer at the sun accurately from a moving platform, but this difficulty is obviated with modern-day instruments. The interest of these instruments also resides in the fact that, in most of the oceans, aerosol optical thickness measurements at the time of satellite overpass are sufficient to verify the atmospheric correction of ocean color (Schwindling *et al.* 1998). They allow one to estimate, via the Angstrom coefficient, the "pseudo" phase function of the aerosols (the product of the single-scattering albedo and the phase function), a key atmospheric correction variable.

Many types of sun photometers have been built and are available commercially. In the following, we focus on two instruments, the MicroTops sun photometer, manufactured by Solar Light, Inc., and the SIMBAD radiometer, built by the University of Lille. The NASA SIMBIOS Program maintains a set of these instruments for use during ocean-color evaluation cruises. The objective is to collect accurate aerosol optical thickness measurements during the ship cruises for comparison with values derived from satellite algorithms.

a) MicroTops

The Solar Light, Inc. MicroTops sun photometer is a hand held radiometer used by many investigators throughout the world. The popularity

of MicroTops sun photometers is due to their ease of use, portability, and relatively low cost. The instruments have five channels whose wavelength can be selected by interference filters. In order to follow the specifications given by the World Meteorological Organization (WMO), the wavelengths are typically chosen at 440, 500, 675, 870 nm, with an additional channel at 940 nm to derive integrated water vapor amounts. If an additional sun photometer is available then it is also desirable to make measurements at 380 and 1020 nm.

The MicroTops sun photometers use photodiode detectors coupled with amplifiers and A/D converters. The collimators are mounted in a cast aluminum block with a 2.5^{o} full field of view. The MicroTops sun photometer has built-in pressure and temperature sensors and allows for a GPS connection to obtain the position and time. A built in microprocessor can calculate the aerosol optical depth, integrated water vapor, and air mass in real time and display these values on a LCD screen. Temperature effects are corrected by taking dark count measurements with the lid covered on startup. Further information on MicroTops sun-photometers can be found in Morys (1998).

b) SIMBAD

The SIMBAD radiometer was designed by the University of Lille to measure both aerosol optical thickness and diffuse marine reflectance, the basic atmospheric correction variables. The radiometric measurements are made in 5 spectral bands centered at 443, 490, 560, 670, and 870 nm. The ocean surface and the sun are viewed sequentially. The same 3^{o} field-of-view optics interference filters, and detectors are used in both ocean- and sun-viewing modes. A different electronic gain, low and high, is used for each mode, respectively. A specific mode allows measurement of the dark current. The optics are fitted with a vertical polarizer to reduce reflected skylight when the instrument is operated in ocean-viewing mode (Fougnie et al., 1999). The polarizer does not affect the sun intensity measurements, because direct solar radiation is not polarized.

Attached to the instrument is a GPS for automatic acquisition of geographic location at the time of measurement. Also acquired automatically are pressure, temperature, and view angles. Frequency of measurements is 10 Hz. In sun-viewing mode, only the highest intensity measured over one second is kept to avoid sun-pointing errors on a moving platform. Data is stored internally and downloaded onto diskette at the end of the day, or cruise. The instrument is powered with batteries, allowing 6 hours of continuous use. In normal use during a cruise (see below), the internal memory and batteries allow for 3 months of operations without downloading data or recharging the batteries.

Installation and Maintenance

The MicroTops and SIMBAD instruments need to be pointed towards the sun manually. The sun is correctly aligned when its image appears in the cross hair on a small screen (MicroTops) or on a target (SIMBAD). After 10-20 minutes of practice the user will become familiar with the pointing procedure and the process will become second nature. It is important to get familiar with this pointing procedure on land as ship based measurements require more skill.

The exterior of the instrument lenses can accumulate salt spray and should be inspected and cleaned if needed. For the open ocean, salt is the primary contaminant. Under these conditions, a lens tissue can be wet with clean (filtered if possible) water or ethanol and used to remove the salt, then a dry lens tissue used to remove remaining water drops.

Faulty electronics pose a potential problem that is not always easy to detect when using MicroTops instruments. In the past it has been found that a leaky capacitor lowered the power and created erratic behavior for the shorter wavelengths where more gain is required. One can also get some idea of the instrument stability by taking numerous measurements with the lid covered. The voltage on all five channels should be less than $\pm$ 0.03 mV and the variability will give some idea of the noise present in the photometer. If the values are greater then the unit should be sent back to the manufacturer for repair.

Measurement Protocols

During stable conditions (land or calm seas) pointing the radiometers at the sun is straightforward and most of the measurements will be accurate. Under rough ocean conditions, pointing at the sun can become the major source of uncertainty, with many of the measurements being off the sun. The measurements that are off the sun will have higher apparent aerosol optical depths, artifacts that bias the average positively. For data acquired under rough sea conditions, repeated measurements of aerosol optical depths are typically distributed in a comet shaped pattern, with

a cluster of lower values and a tail extending to higher values. In these cases, the smaller optical depth values are more accurate and the larger values, which are likely due to pointing error, must be removed in post processing. Since many measurements may be discarded in post processing, it is suggested that 25 or more measurements should be made within a short period of time (less than 5 minutes).

In general, the SIMBAD instrument is used alternatively in sun- and ocean-viewing mode. The sun intensity measurements also allow one to compute down-welled solar irradiance accurately in clear sky conditions, or when the sky is partly cloudy (<30%) with the sun not obscured by clouds. The modeled values of solar irradiance are used to normalize water-leaving radiance measurements.

The recommended protocol is to make consecutively one "dark" measurement, three measurements in sun-viewing mode, one "dark" measurement, three measurements in ocean-viewing mode, one "dark" measurement, three measurements in sun-viewing mode, and one "dark" measurement. It requires about 15 minutes to collect a complete data set (ocean, sun, optical zero), including deploying the instrument and logging ancillary data (wind speed, sea state, cloud cover, etc.).

In order to expedite the measurements, the MicroTops averaging time should be set to one and the sampling down to six samples. The shorter sampling periods will speed the measurements and no averaging will improve the chances that at least some of the measurements are accurately pointed at the sun. After making the measurements, post processing is needed to remove the high values that occur from misalignment with the sun. Once the large values have been removed, the remaining values should be averaged which will reduce electronic noise.

Temperature tests have shown that the aerosol optical thickness derived from MicroTops is strongly dependent on the temperature (Porter *et al.* 2000). Being out in the sun for 1-2 minutes can change the instrument's temperature, and thus affect the aerosol optical depth measurement. In order to avoid this effect, the MicroTops should be turned off and on frequently during the measurement period. It is recommended that the MicroTops be shut off and on every 10 seconds when making measurements, or after every 2 continuous measurements. On the other hand, temperature variation effects are negligible in the SIMBAD measurements.

On several instances we have found condensation to be a problem when radiometers were stored in an air-conditioned room prior to making measurements in the humid marine atmosphere. Condensation may occur outside the SIMBAD radiometer, but can also occur inside the MicroTops (i.e. it is not always possible to wipe it off). To avoid water condensation, the instrument should be placed in the sun to warm to temperatures higher than ambient temperatures prior to making the measurements. It is suggested to leave the instruments in the sun for 15-20 minutes before the measurements. The temperature can be monitored in the MicroTops to ensure enough warming has occurred. This procedure presupposes that the instrument has been calibrated at the elevated temperature level.

For MicroTops the latitude and longitude and time should be set either manually, or by connecting the GPS receiver directly to the radiometer. Using either method, the time can be set to within one second of the correct time. The latitude and longitude can also be stored in the MicroTops for measurements at fixed sites. For SIMBAD the geographic location and time are automatically acquired at the beginning of each acquisition in "dark", sun-viewing, and ocean-viewing modes.

In order to maintain the quality of the aerosol optical thickness measurements, the procedures suggested above should be followed and the radiometers should be calibrated at least twice a year (more frequently if the calibration site is not stable –see Chapter 6). When possible, it is also advisable to make measurements with two instruments. This redundancy will help to determine if any problems are occurring.

Data Analysis

In order to derive aerosol optical thickness measurements, 1) the bad values need to be removed, 2) the air mass should be calculated, and 3) the molecular, ozone, water vapor and trace gas optical depths should be removed.

To remove the bad values, the data should be plotted and large values should be eliminated manually, if they are not part of a systematic trend. Poor pointing artifacts will appear as noise, while real aerosol variations will have a more systematic behavior when plotted as a short time series. This visual inspection and removal of large values should be done for each channel, and it should not be assumed that removing all bad data points in one channel will remove all bad data for all channels. In this process a final optical depth variability of 20%

of the final average value or 0.025 may be permitted when the optical depths are below 0.08. This approach may slightly bias the data to lower values but it will remove the unrealistic larger values that would occur if the data were not filtered.

In the standard processing, the direct atmospheric transmittance $T(\lambda) = exp(- \tau(\lambda)\ m)$ and, thus, the total optical thickness $\tau(\lambda)$ is obtained from the sun intensity (or voltage) V measured by the radiometer and the calibration constant V_0, by solving the Beer-Lambert-Bouguer equation (Eq. 5.1). The protocols used within the SIMBIOS Project to calculate AOT are described below in Sect. 5.6.

5.5 FAST-ROTATING SHADOW-BAND RADIOMETERS

An estimate of τ_a can be made from calibrated measurements of the solar beam irradiance, $E_M(\lambda)$, at normal incidence when there are no clouds in front of the solar disk. Two sun photometer designs are commonly used to measure $E_M(\lambda)$: a narrow-beam detector mechanically pointed at the solar disk and a wide-field-of-view radiometer with a solar occulting apparatus. The first type of sun photometer requires careful angular positioning and can provide additional information about the forward scattering phase functions that help characterize the aerosol constituents. In contrast, a radiometer equipped with an occulting apparatus, known as a shadow-band radiometer, measures the diffuse and global (upper hemispheric) irradiance and computes $E_M(\lambda)$ from the difference between the two. The device gets its name from the hemispherical metal strip that rotates around the detector and blocks the direct solar beam to yield a signal that is from the sky only (after the effect of the arm is included).

The multiple wavelength rotating shadow-band radiometer (Harrison et al., 1994) uses independent interference-filter-photodiode detectors and an automated rotating shadow-band technique to make spatially resolved measurements at seven wavelength pass-bands. The uncertainty of the direct-normal spectral irradiance measurement made with this type of sun photometer is comparable with that made by narrow-beam tracking devices. A significant advantage of the shadow-band technique is that the global and diffuse irradiance measurements can be used to study the solar radiation budgets and the fractional cloud cover at the time of the measurement. The latter capability is particularly important for satellite validation studies. In the SIMBIOS context, direct solar and diffuse sky irradiances are critical terms for correcting down-looking in-water radiometers for self shading (Gordon and Ding (1995).

A marine version of the multiple-wavelength rotating shadow-band radiometer has been developed at the Brookhaven National Laboratory (BNL). The BNL marine version uses a slightly modified version of the detector used for continental applications. It has seven channels: one broadband silicon detector and six ten-nm-wide channels at 415, 500, 610, 660, 870, and 940 nm. Modifications to the detector circuitry used for continental applications are necessary because the response time of the original circuitry is too slow for use on a moving ship. If the response time of the detector is too slow, wave action may cause the orientation of the radiometer to change appreciably during the time the shadow-band is occulting the sun. The rotation of the shadow-band itself must be sufficiently fast for the same reason. The marine version of the shadow-band radiometer is hereafter referred to as the BNL Fast-Rotating, Shadow-band Radiometer (FRSR). Implicit in this terminology is that the FRSR is a multi-filter or "spectral" radiometer.

The response of the silicon cell in the detector used for continental applications is faster than one millisecond, yet the internal preamplifiers have integrating low-noise amplifiers that slow the overall response. The response time of the detector is made faster for marine applications by reducing the magnitude of the low-pass filter capacitors. Laboratory tests do not show additional noise in the measurements as a result of this modification. The processing algorithms, which incorporate pitch, roll and heading measurements, are key to the instrument's ability to derive direct-normal beam irradiance without gimbals and a gyro-stabilized table.

Installation and Maintenance

The installation location of the instrument on a ship must be carefully selected. Ideally, FRSRs should be mounted in an exposed location as high as possible and free of nuisance shadows from other objects. This is often difficult. Radiation measurements on a ship always need to consider errors from the ubiquitous masts and antennas. A ship's communication antennas have highest vertical priority as do the running lights, and one must be careful of radar beams that can cause

severe electronic noise. Once a suitable location has been found and the instrument mounted, the diffuser should be rinsed with distilled water and wiped with a moistened cloth at least once per day. The FRSR is typically mounted as a part of a portable radiation package that includes independent broadband solar and IR radiometers. The glass domes on these radiometers should be rinsed with distilled water and wiped with a moistened cloth.

Calibration is the most essential element of a radiation measurement program. A thorough and on-going calibration process is required before the FRSR can make accurate radiometric measurements at sea. To insure accurate measurements, there are two important elements for FRSR measurement protocol: calibration of the instrument circuitry, which includes temperature stabilization of the detector during measurements, and determination of the extra-terrestrial constants.

Data Analysis

The shadow-band radiometer must properly measure the global and diffuse irradiances from which the direct-beam solar irradiance is derived by the subtraction as

$$E_{sun}(\lambda) = E_s(\lambda) - E_{sky}(\lambda), \qquad (5.4)$$

where $E_{sun}(\lambda)$ is the direct-beam solar incident irradiance projected onto a horizontal plane, $E_s(\lambda)$ is the global irradiance incident on the horizontal plane, and $E_{sky}(\lambda)$ is the diffuse incident irradiance from non-forward scattering. The global irradiance, $E_s(\lambda)$, is measured when the band is out of the field of view and the sensor is exposed to full sunlight. The irradiance normal to the incident solar beam is determined as

$$E_N(\lambda) = E_s(\lambda)\sec\theta_o, \qquad (5.5)$$

A correction for the amount of sky that is blocked by the occulting band is essential for an accurate measurement. An automatic correction for the shadowband is possible through measurement of ``edge'' irradiance as is done with the land-based shadow-band radiometers. The shadow irradiance, $E_{shadow}(\lambda)$, occurs when the sun is completely covered by the shadowband, but a portion of the diffuse irradiance is also blocked. The edge irradiance, $E_{edge}(\lambda)$, is measured when the band is just to one side of the solar disk and provides a good estimate of the global irradiance minus the portion of sky that is blocked by the shadowband at the time it blocks the solar disk. In practice, $E_{edge}(\lambda)$ is selected from two measurements taken when the shadow is on one side or the other of the diffuser. Generally an average is taken, but in some cases in the early morning or late evening only one of the edges is acceptable. It is easy to show that the fully corrected direct solar incident irradiance is

$$E_{sun}(\lambda) = E_{edge}(\lambda) - E_{shadow}(\lambda). \qquad (5.6)$$

With the fast-rotating technique, an advantage of using (5.6) to determine $E_{sun}(\lambda)$ is that the edge and shadow measurements are made in a very short time, which reduces noise significantly, especially on partly cloudy days. Also, if the electronics have a constant bias, the bias is removed by the subtraction. On a moving platform, some smoothing of the data is necessary. It was found that simple averages over a two-minute period (16 sweeps) would reduce the sampling uncertainty by a factor of approximately 4, and yield worst-case measurement uncertainties of about 5 Wm^{-2} for the global values and less than 1 Wm^{-2} for the shadow value. For perspective, two minutes is the approximate time for the sun to move by one diameter across the celestial sphere. A discussion and an example of the effectiveness of the two-minute averaging process is shown in Reynolds *et al.* (2000).

The shadow-band theory must be modified for a moving platform when the head might not be on a horizontal plane. Three measurement quantities for each channel are computed from the two-minute mean voltages: the global signal, v'_G, the shadow signal, v'_S, and the edge value, v'_E. The primes indicate the measurement is referenced to the plane of the head, which can be different than a horizontal plane. The two global measurements, v_{G1} and v_{G2}, are combined to produce the best estimate of global voltage, v'_G. The mean shadow voltage is v'_S. The edge value is selected from the two-minute composite sweep using an objective algorithm that accounts shadow width dependence on solar zenith and relative azimuth angles. The objective selection of the edge voltage uses one or a mean of both edge measurements to get the best estimate of v'_E. The voltage due to direct-beam irradiance falling onto the plane of the instrument is given by

$$v'_H = v'_E - v'_S. \qquad (5.7)$$

This equation automatically corrects for the sky that is blocked by the shadow-band and also

removes any bias term in the calibration equation. An important point in (5.7) is that the right-hand quantities are measured in a few tenths of a second, while the shadow crosses the diffuser. In such a short time interval the ship attitude changes insignificantly and interference from moving clouds is minimized. The diffuse component of the irradiance signal is computed from

$$v'_D = v'_G - v'_H. \tag{5.8}$$

As we have stated previously, v'_D is relatively unaffected by small amounts of platform motion. The exact azimuth and elevation of the solar beam relative to the head must be computed from the following variables measured externally:

$$\{\alpha_h, \theta_h\} = f(\alpha_S, \phi_P, \phi_R, \alpha_r, \theta_r) \tag{5.9}$$

where $\{\alpha_h, \theta_h\}$ are the solar azimuth angle and solar zenith angle relative to the plane of the head, α_r is the mean heading of the ship in true coordinates, ϕ_P is the ship mean pitch, and ϕ_R is the corresponding mean roll over the two-minute period. The relative solar azimuth and zenith angles in geographic coordinates, as seen by the observer, are α_r and θ_r.

Equation (5.6) uses three two-dimensional coordinate transformations in heading, pitch, and roll to shift the solar beam vector to a coordinate system aligned with the FRSR head. The matrix transformation technique is well known and discussed in many textbooks on matrix algebra. Once α_h and θ_h are known, the calibration table can be consulted and an interpolated correction value, $\chi(\alpha_h, \theta_h)$, can be derived.

The direct beam intensity on a horizontal plane relative to the instrument, v'_H, is converted to a direct-beam intensity into a plane normal to the solar beam using the relationship

$$v_N = \frac{v'_H}{\chi(\alpha_h, \theta_h)\cos\theta_h} \tag{5.10}$$

The global and horizontal voltages are re-computed for the Earth frame of reference:

$$v_H = v_N \cos\theta_r \tag{5.11}$$

$$v_G = v_H + v_D \tag{5.12}$$

The calibration equation is used to compute E_S, E_{sky}, E_{sun}, and E_N from v'_G, v'_D, v'_H, and v'_N respectively. From these terms, the Beer-Lambert-Bouguer law (equation 5.1) can be used for estimating the calibration constant or $\tau_a(\lambda)$.

Cloud filtering is the most important challenge for FRSR data processing. Because the FRSR operates autonomously, cloud observations are naturally part of the signal that must be processed to obtain τ. The cloud filter that is currently used is based on two steps: computing signal statistics over windows of periods of less than two hours and using these statistics to judge the quality of the observation under consideration. If the standard deviation of the observations in a two-hour moving window is less than 0.05, a subjectively defined threshold, and the observation at the center of the window is also less than 0.05, the central observation is accepted. The underpinning of this cloud filtering technique is that τ is relatively constant over a period of two hours, while the cloud signal is highly variable. This approach has proven relatively successful, although improvements in the filter are expected in the future.

5.6 SIMBIOS PROJECT AOT EXTRACTION PROTOCOLS

The SIMBIOS Project is concerned with ocean color satellite sensor intercomparison and merger for biological and interdisciplinary studies of the global oceans. Imagery from different ocean color sensors can now be processed by a single software package using the same algorithms, adjusted by different sensor spectral characteristics, and the same ancillary meteorological and environmental data. This enables cross-comparison and validation of the data derived from satellite sensors and, consequently, creates the continuity of ocean color information in temporal and spatial scales. The next step in this process is the integration of *in situ* obtained ocean and atmospheric parameters to enable cross-validation and further refinement of the ocean color methodology.

Atmospheric correction of satellite radiances and, in particular, estimation of aerosol effects on the upwelling radiance at the top of the atmosphere is one of the most difficult aspects of satellite remote sensing. Merging of aerosol properties obtained from *in situ* observations with these derived by sensor algorithms creates exceptional opportunities to validate and improve the atmospheric correction. There are many uncertainties associated with *in situ* measurements themselves. They include sun photometer or radiometer calibration and operation problems, inadequate handling by people and cloud contamination. When matching against atmospheric

properties obtained by a satellite sensor, additional uncertainties come into play which are caused by different viewing angles by the satellite and surface instruments and by time discrepancies when both instruments acquire their observations. In the case of the atmosphere, these uncertainties are considerable.

Therefore, the fine calibration of sun photometers and radiometers is needed as well as the best possible (and uniform from instrument to instrument) correction of obtained measurements. Finally, having multiple observations and from different sun photometers and radiometers is required to cross-validate the quality of *in situ* data, extract measurements of high stability and confidence and compare them against satellite sensor estimates with a larger degree of certainty.

Extraction of in situ AOTs

The Project has recently implemented its own correction strategy for instrument voltages corresponding to AOTs. The approach ensures a uniform AOT processing for all instruments making the AOTs comparable amongst the instruments and between instruments and satellite sensor AOTs derived by means of the atmospheric correction. Also, the method uses a consistent set of tuning variables, such as ancillary data, concurrently applied for the correction of satellite radiances. Therefore, some stages of the satellite and *in situ* data processing are identical, contributing to increasing confidence in the match-ups.

Firstly, separate procedures retrieve sun intensity measurements, V(λ), from individual sun photometers and, in case of the shadow-band radiometer, processed direct-beam irradiances (corresponding to the $I_H(\lambda)$ term from the section 5.4). The following processing is uniform for all instruments, however, of course considers distinct spectral wavelengths used by the sensors. The Beer-Lambert-Bouguer law (equation 11.1) can be written as follows:

$$V(\lambda)=V_0(\lambda)*\left(\frac{d_0}{d}\right)^2\exp\left(-M(\theta_s)\tau_R(\lambda)\right) \qquad (5.13)$$
$$*\exp\left(-M(\theta_s)\tau_o(\lambda)\right)*\exp\left(-M(\theta_s)\tau_a(\lambda)\right)$$

where τ_R and τ_o are the molecular (Rayleigh) and ozone and aerosol optical thickness, respectively, and the other terms have been previously defined. The equation (5.14) assumes that the signal, $V(\lambda)$, captured by a sun photometer is measured when the instrument is pointing directly into the sun and that gaseous absorption is only due to ozone.

The earth-sun distance adjustment, $(d_0/d)^2$ and air mass, M, are calculated using equations 5.2 and 5.3, respectively. Currently, the same value of air mass is used for Rayleigh, ozone, and aerosol factors.

The desired variable τ_a is extracted from equation 5.13 by calculating all other variables. The following estimations of earth and atmospheric parameters to obtain AOT coincide with the SeaWiFS satellite sensor correction, including the choice of meteorological and ozone ancillary data.

Calculations of the Rayleigh optical thickness apply the most contemporary atmospheric pressure readings obtained from the spatial and temporal approximation of daily global pressure maps provided by the National Centers for Environmental Prediction. The Rayleigh optical thickness is extracted as follows:

$$\tau_R(\lambda)=k_{Ray}(\lambda)*e^{-\frac{A}{7998.9}}*\frac{P}{P_0}, \qquad (5.14)$$

where, k_{Ray} is defined as

$$k_{Ray}(\lambda)=28773.597886*\left\{1.0e^{-8}\left[8342.13+\frac{2406030}{130-\frac{1}{\lambda^2}}+\frac{15997}{38.9-\frac{1}{\lambda^2}}\right]\right\}^2*$$
$$\left\{1.0e^{-8}\left[8342.13+\frac{2406030}{130-\frac{1}{\lambda^2}}+\frac{15997}{38.9-\frac{1}{\lambda^{-2}}}\right]+2\right\}^2*\frac{1}{\lambda^{-4}}. \qquad (5.15)$$

where A is the altitude, P is the current atmospheric pressure, and P_0 is the standard atmospheric pressure of 1013.25 hPa (Kasten and Young 1989).

The ozone optical thickness is acquired from spatial and temporal approximation of daily satellite global measurements of ozone amounts. Preferably, ozone data come from Total Ozone Mapping Spectrometer (TOMS). If TOMS data are unavailable, ozone counts from TIROS Operational Vertical Sounder (TOVS) are used. Finally, if TOVS data are missing, ozone climatology files are applied. The ozone optical thickness is calculated from the ozone amount, Dobson, using a scaling factor $k_{oz}(\lambda)$,

$$\tau_0(\lambda)=k_{oz}(\lambda)*\frac{Dobson}{1000}, \qquad (5.16)$$

where $k_{oz}(\lambda)$ is expressed below for the following spectral bands (Nicolet at al., 1981):

λ = (315, 340, 380, 400, 415, 440, 443, 490, 500, 560, 610, 660, 670, 675, 862, 870, 936, 1020);

k_{oz} (λ) = (1.35, 0, 0.00025, 0.00065, 0.00084, 0.0034, 0.00375, 0.02227, 0.0328, 0.10437, 0.12212, 0.05434, 0.04492, 0.0414, 0.00375, 0.0036, 0, 0).

REFERENCES

Bass, A.M. and R.J. Paur, 1984: The ultraviolet cross-section of ozone: 1. The measurements, in Atmospheric Ozone, edited by C.S. Zerefos & A. Ghazi, pp. 606-610, Reidel, Dordrecht.

Bruegge, C.T., J.E. Conel, R. O. Green, J.S. Margolis, R.G. Holm, and G. Toon, 1992: Water vapor column abundance retrievals during FIFE. J.Geophys. Res., 97(D19), 18759-18768.

Burcholtz, A., 1995: Rayleigh-scattering calculations for the terrestrial atmosphere, Appl. Opt., 34, 2765-2773.

Dubovik, O.and M.D.King,, 2000: A flexible inversion algorithm for retrieval of aerosol optical properties from Sun and sky radiance measurements, J. Geophys. Res., (submitted).

Dubovik, O., A.Smirnov, B.N.Holben, M.D.King, Y.J. Kaufman, T.F.Eck, and I.Slutsker, 2000: Accuracy assessments of aerosol optical properties retrieved from AERONET Sun and sky-radiance measurements, J. Geophys. Res., 105, 9791-9806.

Edlen, B., 1966: The refractive Index of Air, Meteorol., 2, 71-80.

Ehsani, A. R., J. A. Reagan, and W. H. Erxleben, 1998: Design and performance analysis of an automated 10-channel solar radiometer instrument, J. Atmos. Ocean. Tech., 15, (in press).

Forgan, B.W., 1994: General method for calibrating Sun photometers, Applied Optics, 33, 4841-4850.

Fougnie, B., R, Frouin, P. Lecomte, and P-Y. Deschamps, 1999: Reduction of skylight reflection effects in the above-water measurement of marine diffuse reflectance. Applied Optics, 38, 3844-3856.

Gordon, H. R., J. W. Brown, and R. H. Evans, 1988: Exact Rayleigh scattering calculations for use with the Nimbus-7 coastal zone color scanner, Applied Optics, 27, 862-871.

Gordon, H.R., and K. Ding, 1992: Self shading of in-water optical instruments. Limnol. Oceanogr., 37, 491--500.

Gordon, H. R. and T. Zhang, 1995: Columnar aerosol properties over oceans by combining surface and aircraft measurements: simulations. Applied Optics, 34, 5552 – 5555.

Hansen, J. E., and L. D. Travis, 1974: Light scattering in planetary atmospheres. Space Sci. Rev., 16, 527-610.

Harrison, L. and J. Michalsky, 1994: Objective algorithms for the retrieval of optical depths from ground-based measurements, Applied Optics, 33 ,5126-5132.

Harrison, L., J. Michalsky, and J. Berndt, 1994: Automated multi-filter rotating shadow-band radiometer: an instrument for optical depth and radiation measurements, Applied Optics, 33, 5126-5132.

Holben, B.N., T. F.Eck, I.Slutsker, D.Tanre, J.P.Buis, A.Setzer, E.Vermote, J.A.Reagan, Y.Kaufman, T.Nakajima, F.Lavenu, I.Jankowiak, and A.Smirnov 1998: AERONET - A federated instrument network and data archive for aerosol characterization, Rem. Sens. Environ., 66, 1-16.

Iqbal., M., 1983: An introduction to Solar Radiation, Academic, San Diego, Calif., 390 pp.

Kasten F. and A. T. Young, 1989: Revised optical air mass tables an approximation formula, Applied Optics, 28: 4735-4738.

Kaufman, Y.J., A. Gitelson, A. Karnieli, E. Ganor, R.S. Fraser, T. Nakajima, S. Mattoo, B.N. Holben, 1994: 'Size Distribution and Phase Function of Aerosol Particles Retrieved from Sky Brightness Measurements', J. Geophys. Res., 99, 10341-10356.

Kneizys, F.X., E.P. Shettle, L.W. Abreu, J.H. Chetwynd, G.P. Anderson, W.O. Gallery, J.E.A. Selby, and S.A. Clough, 1988: Users Guide to LOWTRAN 7, AFGL-TR-88-0177,

(NTIS AD A206773), Air Force Geophysics Laboratory, Hanscom Air Force Base, Massachusetts.

Komhyr, W. D., R. D. Grass, and R. K. Leonard, 1989: Dobson Spectrophotometer 83: a standard for total ozone measurements, 1962-1987, J. Geophys. Res., 94, 9847-9861.

Liu, Y. and K. J. Voss, 1997: Polarized radiance distribution measurements of skylight: II. experiment and data. Applied Optics, 36,8753 - 8764.

London, J., R. D. Bojkov, S. Oltmans, and J. I. Kelley, 1976: Atlas of the global distribution of total ozone July 1957 - June 1967, NCAR Technical Note 133+STR, National Center for Atmospheric Research, Boulder, Colorado, 276 pp.

Michalsky, J. J., 1988: The astronomical almanac's algorithm for approximate solar position (1950 - 2050), Solar Energy, 40, 227 - 235.

Morys, M., F.M. Mims III, and S.E. Anderson, 1998: Design, calibration and performance of MICROTOPS II hand-held ozonometer.

Nakajima, T., M. Tanaka and T. Yamauchi, 1983: Retrieval of the optical properties of aerosols from aureole and extinction data. Applied Optics, 22, 2951-2959.

Nakajima, T., G. Tonna, R. Rao, P. Boi, Y. Kaufman, and B. Holben, 1996: Use of sky brightness measurements from ground for remote sensing of particulate polydispersions, Applied Optics, 35, 2672-2686.

Nicolet M., 1981: The solar spectral irradiance and its action in the atmospheric photodissociation processes, Planet. Space Sci., 29, 951-974.

Penndorf, R., 1957: Tables of the Refractive Index for Standard Air and the Rayleigh Scattering Coefficient for the Spectral Region Between 0.2 and 20.0 Microns and their Application to Atmospheric Opt., J. Opt. Soc. Am., 47, 176-182.

Porter, J. N., M. Miller, C. Pietras, and C. Motell, 2000: Ship-based sun photometer measurements using MicroTops sun photometers, J. Ocean. Atmos. Tech. (in press).

Reagan, J.A., K.J. Thome, and B.M. Herman, 1992: A simple instrument and technique for measuring columnar water vapor via Near-IR differential solar transmission measurements. IEEE Trans. Geosci. Remote Sensing, 30, 825-831.

Reynolds, R.M., M.A. Miller, and M.J. Bartholomew, 2000: Design, Operation, and Calibration of a Shipboard Fast-Rotating Shadow-band Spectral Radiometer, Jour. Atmos. Ocean. Tech., (accepted).

Ritter, J. M. and K. J. Voss, 2000: A new instrument to measure the solar aureole from an unstable platform. J. Atmos. Ocean. Tech., in press.

Schmid, B., C. Matzler, A. Heimo and N. Kampfer, 1997: Retrieval of Optical Depth and Particle Size Distribution of Tropospheric and Stratospheric Aerosols by Means of Sun Photometry, IEEE Trans. on Geosci. and Rem Sens., 15, 172-182.

Schwindling, M., P.-Y. Deschamps, and R. Frouin. 1998: Verification of aerosol models for satellite ocean color remote sensing. J. Geophys. Res., 24,919-24,935.

Shaw, G. E., 1983: Sun Photometry, Bull. Amer. Meteor. Soc., 64, 4-11.

Shiobara, M., T. Hayasaka, T. Nakajima and M. Tanaka, 1991: Aerosol monitoring using a scanning spectral radiometer in Sendai, Japan. J. Meteorol. Soc. of Japan, 60, 57-70.

Smirnov, A., B.N.Holben, T.F.Eck, O.Dubovik, I.Slutsker, 2000: Cloud screening and quality control algorithms for the AERONET data base. Rem. Sens. Environ., (accepted).

Tanré, D., C. Devaux, M. Herman and R. Santer, 1988: Radiative properties of desert aerosols by optical ground-based measurements at solar wavelengths. J. Geophys. Res., 93, 14223-14231.

Tanré, D., C. Deroo, P. Duhaut, M. Herman, J.-J. Morcrette, J. Perbos, and P.-Y. Deschamps, 1990: Description of a computer code to simulate the signal in the solar spectrum: the 5S code. Int. J. Remote Sensing, 11, 659-668.

Young, A.T., 1980: Revised Depolarization Corrections for Atmospheric Extinction, Applied Optics, 19, 3427-3428.

Vigroux, E., 1953: Contribution a l'etude experimentale de l'absorption de l'oxone, Annales de Phys., 8, 709.

Volz, F.E., 1959: Photometer mit Selen-photoelement zurspektralen Messung der Sonnenstrahlung und zer Bestimmung der Wallenlangenabhangigkeit der Dunsttrubung. Arch. Meteor. Geophys Bioklim. B10, 100-131.

Voss, K. J. and Y. Liu, 1997: Polarized radiance distribution measurements of skylight: I. system description and characterization. Applied Optics, 36, 6083-6094.

Voss, K. J., 1989: Electro-optic camera system for measurement of the underwater radiance distribution. Optical Engineering, 28, 241-247.

Voss, K. J. and G. Zibordi, 1989: Radiometric and geometric calibration of a spectral electro-optic "fisheye' camera radiance distribution system. J. Atmos. Ocean. Tech.., 6, 652-662.

Wang, M. and H. R. Gordon, 1993: Retrieval of the columnar aerosol phase function and single-scattering albedo from sky radiance over the ocean: simulations. Applied Optics, 32,4598 – 4609.

Zhang, T. and H. R. Gordon, 1997a: Columnar aerosol properties over oceans by combining surface and aircraft measurements: sensitivity analysis. Applied Optics, 36, 2650 – 2662.

Zhang, T. and H. R. Gordon, 1997b: Retrieval of elements of the columnar aerosol scattering phase matrix from polarized sky radiance over the ocean: simulations. Applied Optics, 36,7948 – 7959.

Chapter 6

SIMBIOS Project Protocols for Processing *In Situ* Aerosol Optical Thickness Measurements

Ewa J. Ainsworth[1], Christophe Pietras[1], Mark Miller[2], Robert Frouin[3] and Sean Bailey[4]

[1]*SAIC General Sciences Corporation, Beltsville, Maryland*

[2]*Department Environmental Science, Earth System Science Division, Brookhaven National Laboratory, Upton, New York*

[3]*Scripps Institution of Oceanography, University of California, San Diego, California*

[4]*Future Tech Corporation, Greenbelt, Maryland*

6.1 INTRODUCTION

In situ measurements from sun and sky radiometers are extremely useful for vicarious calibration of satellite ocean color sensors and validation of atmospheric correction algorithms. An atmospheric property which has been applied in the analyses is aerosol optical thickness (AOT). AOT values are obtained from a direct solar signal and sky radiances processed using latest radiometer calibration parameters and corrected for gas absorption and molecular scattering. AOT levels calculated from satellite sensor observations are a by-product of the atmospheric correction (Gordon and Wang, 1994). *In situ* and satellite-obtained AOT values are quality screened and compared against each other to create a reliable set of match-ups. The term "match-ups" relates to the results of the AOT comparisons. The match-ups are explored to draw conclusions about the satellite sensor calibration and the suitability of the set of aerosol models applied in the sensor atmospheric correction.

Uncertainties Associated With AOT Measurements

There are several uncertainties associated with sun and sky radiometer measurements which need to be carefully investigated. Some of the reasons for these uncertainties stem from inconsistencies in the radiometer calibration, in the processing of raw radiometer observations, and from purely erroneous observations. The accuracy of the correction of direct sun intensity measurements for sun photometers and of diffuse and global solar beam irradiances for sky radiometers is important in the derivation of AOT values from the digital counts captured by the instruments. Before the current study, individual primary investigators using their own correction parameters frequently performed this processing. As a result, the correction techniques and the derived AOT values were not universally comparable. A streamlined measurement correction method has now been introduced for all radiometers (Chapter 5). Some stages of the *in situ* and satellite data processing are actually interchangeable, thus contributing to an increase in confidence in the match-ups. There can be various reasons for erroneous radiometer observations. Many errors occur due to the difficulty for an investigator to point a hand-held instrument directly into the sun, especially from a ship's deck. Occasionally, some spectral bands are missing from a measurement set. Depending on the nature of the flaws, the defects can be uncovered by analyzing the behavior of the measurement in a temporal sequence of observations and in the spectral distribution of the measurements.

Uncertainties Associated With Comparing Data Sets From Different Sources

Radiometer and satellite sensor observations of aerosols are different in nature. Radiometer measurements are obtained from the ground and a single location at a time. Satellite observations are performed from space at the top of the atmosphere. For SeaWiFS, a 30 sec viewing duration provides 100 km of observation around a ground target (Gregg et al., 1994). There usually are several to a few hundred AOT measurements collected from each sun or sky radiometer per day. The number of daily measurements depends on the instrument and investigator. Automatic radiometers and hand-held sun photometers operate differently. Some radiometers work from a moving platform, such as a ship, and some need to be stationary. On the other hand, there normally is one ocean color satellite observation of the same spot on the ground

per day (there may be two or more observations in higher latitudes). Thus, a large number of *in situ* radiometer observations need to be compared against information carried by a single satellite image.

There are a few conditions which adversely influence the comparisons of AOT values derived from ground radiometers and satellite sensors. These include:

1. the variability in the measurement styles employed for each ground radiometer and investigator;
2. cloud contamination;
3. time differences between the satellite and ground instrument observations; and
4. viewing geometry differences between the satellite and ground observations.

The SIMBIOS Project has a continuously growing collection of *in situ* AOT measurements stored in both the SeaBASS and AERONET databases. These AOT measurements are obtained from coastal and ship-borne radiometers around the globe and form large and diverse data sets. AOT observations are acquired from different investigators and different sun and sky radiometers where the operators apply their individual styles while taking the measurements. Temporal distributions of daily AOT observations vary substantially from data set to data set and cannot be generalized. Automatic sun and sky radiometers, CIMEL and Shadow-band, usually take measurements within proportional time intervals through a day. The frequency of observations obtained from hand-held sun photometers, SIMBAD and MICROTOPS II, is influenced by individual operator preferences and their judgement of clear sky conditions.

Both ground radiometer and satellite sensor atmospheric measurements suffer from the frequent problem of cloud contamination. The fractional global cloud cover decreases from 50% at the equator to just over 40% at 17° to 30° latitude. Then, the cloud cover increases steadily from mid to higher latitudes reaching around 80% at 64° latitude and more towards the poles (Paltridge and Platt, 1976). Cloud contamination significantly limits the extent of radiometer and satellite measurements of global aerosols. Fractional cloud contamination of ground-radiometer and satellite-image-pixel observations masks aerosol signatures and causes erroneous or unreliable AOT match-up results. Therefore, cloud screening is a vital operation in the processing of both types of aerosol information.

It takes a satellite a split second to observe a geographical location where a sun or sky radiometer is operational. It is highly unlikely that the ground radiometer performs its measurements exactly at the same time as the satellite. The time difference between the two observations introduces an uncertainty in comparisons of both types of observations. This uncertainty arises from changing atmospheric conditions, which may include cloud and aerosol plume movements.

Earth orbit and the scanning mechanism define a satellite viewing geometry. For example, SeaWiFS flies in a sun synchronous orbit at 705 km with a descending equator crossing at 20 min past noon, local time. SeaWiFS scans across the Earth's surface from west to east (Barnes et al., 1995). Each scan contains 1,285 contiguous pixels over a 116.6° scan angle centered at nadir. Each pixel is nominally square with a side length of 1.6 mrad, which corresponds to 1.13 km at nadir. When SeaWiFS samples away from nadir, the path length between the instrument and the Earth increases as well as the pixel size.

Sun photometers, on the other hand, capture photometric intensity of the direct solar beam. They are pointed from the Earth's surface precisely into the sun disk. Sky radiance scanning systems, which include fast rotating Shadow-band radiometers, obtain solar intensity values indirectly from diffuse and global (upper hemispheric) solar beam irradiance by measuring the solar aureole and sky radiance distributions.

Therefore, both ground and satellite instruments observe different paths through the atmosphere which may have significantly different optical properties. There may be clouds or cloud edges observed by a satellite over a sun photometer location while the photometer, looking at the sun, may see a clear sky. Conversely, a radiometer sun measurement may be contaminated with clouds while a satellite pixel centered on the location of the radiometer may be cloud free. In the same manner, the satellite and ground sensors may observe different aerosol types.

General Strategy For Processing of AOT Observations

With large and diverse AOT *in situ* data sets available for the match-ups, a complete and effective processing of radiometer and satellite observations is vital. A processing strategy has been designed and implemented to compare *in situ* observations with those of SeaWiFS (Ainsworth et al., 2000). The strategy is aimed to:

- minimize the match-up uncertainties; and
- make full use of the large volume and diversity of the existing data sets.

Match-up uncertainties arise both from uncertainties associated with sun and sky radiometer measurements and from uncertainties in comparing two data sets coming from different sources. The SIMBIOS Project has created ocean optics protocols for satellite ocean color sensor validation (Fargion and Mueller, 2000). The protocols establish strictly defined instrument calibration procedures which are described in Chapter 5. The SIMBIOS Project has also implemented its own processing strategy to convert radiometer digital count measurements to geophysical AOT values. This strategy is described in Chapter 5. The approach provides a uniform algorithm for obtaining AOT levels for all radiometers which makes AOT measures comparable among the instruments and between the instruments and the satellite sensor. Direct sun intensity measurements and direct-beam solar irradiances, in case of the Shadow-band radiometer, are corrected for molecular and ozone scattering, air mass, and Earth-sun distance. The algorithm uses a consistent set of tuning variables and ancillary data of atmospheric ozone and pressure concurrently applied for the correction of satellite radiances. Therefore, sections of the radiometer measurement processing are the same as portions of the SeaWiFS processing. This approach eliminates most of the inconsistencies in the atmospheric correction of radiometer observations, thus in turn contributing to higher confidence in the match-ups.

The screening of radiometer AOT values is designed to intercept the remaining erroneous or badly processed measurements by analyzing their spectral distributions and behavior within time sequences of AOT observations. Because of the uncertainties involved in comparing satellite and ground radiometer AOT information, these two distinct data sets are processed individually:

- ground radiometer AOT measurements are temporally screened throughout a day; and
- satellite-derived AOT observations are spatially screened within an image window corresponding to the radiometer geographical location.

The quality of the temporal screening of radiometer AOT observations is often dependent on the amount and daily spread of AOT measurements. The screening is easier with a larger number of measurements and when their spread through a day is more regular. However, as shown below, distributions of daily AOT observations cannot be generalized for the variety of radiometers and operators involved in the SIMBIOS Project. A significant part of this study is concerned with the search for a method which will work the best with any daily AOT distributions. The analysis of AOT time sequences is currently the only available cloud screening method for radiometer data. The approach assumes that clear AOT observations cannot undergo rapid changes in time and space, except for narrow plumes which are unfortunately discarded as clouds during the processing (Smirnov et al., 2000). The smoothness criterion, which limits sudden increases and decreases in AOT measurements, is usually implemented by placing thresholds on AOT variations throughout a day or within smaller temporal sequences of AOT observations. The current study has investigated a number of cloud screening approaches which will be described below. Cloud screening employed with satellite imagery is a part of the sensor processing algorithms. For SeaWiFS, a threshold is set on albedo at 865 nm to mask out the pixels which are contaminated by clouds and ice.

Uncertainties arising from time and viewing geometry differences between satellite and ground observations are tackled by analyzing larger temporal and spatial AOT sequences. Only those atmospheres are extracted which are relatively stable in time and space. The derived AOT match-up points are then characterized by the uniformity and clarity of atmospheric conditions. Strict algorithm checks for cloud contamination and limits are put on the spatial and temporal aerosol variabilities. This strategy may reject many valid AOT radiometer and satellite measurements. However, it also increases the match-up confidence in view of significant uncertainties associated with comparing information from the two sources by ensuring that only unambiguous aerosol examples are compared between satellite and radiometer observations. These unambiguous match-ups are then credible enough to provide confident statistics on the deviation in the satellite sensor gains and to validate the applied set of aerosol models (Shettle and Fenn, 1979).

For the SIMBIOS Project, a universal strategy has been designed and implemented to automatically and effectively screen temporal sets of *in situ* AOT daily observations. The screening removes cloudy and erroneous AOT measurements and the measurements which exhibit questionable atmospheric properties. It also studies the uniformity of the atmosphere around the time of the

satellite over-flight. Discrete radiometer spatial coverages are considered for instruments operated from a moving platform. This accounts for changes in the geographical situations of the measurement sites. Finally, mean daily *in situ* AOT measures are calculated for the time around the satellite over-flight which are then compared against screened AOT values derived from satellite data.

The *in situ* AOT screening strategy has been designed to accommodate aerosol measurements obtained from all SIMBIOS sun photometers and sky radiometers, as well as for different radiometer operation styles and atmospheric conditions. Several algorithms have been investigated to identify their abilities to comprehensively and efficiently screen *in situ* temporal observations for cloudy and faulty measurements. Satellite derived AOT values are uniformly screened within spatial image windows. The windows are centered on the geographical coordinates of AOT *in situ* measurements which passed the temporal screening. The windows have a standard ground coverage irrespective of their format: Local Area Coverage (LAC), High Resolution Picture Transmission (HRPT), or Global Area Coverage (GAC). The screening applies a set of pixel exclusion criteria used operationally to derive SeaWiFS standard ocean and atmospheric products and includes the albedo-threshold cloud masking. The uniformity of the atmosphere within the windows is established based on the same conditions as used for the temporal AOT *in situ* measurements. Consequently, temporal and spatial atmospheric properties are tested in a similar fashion for radiometer and satellite AOT observations.

This supports the comparability of the two data sets. The occurrences of aerosol distributions which are overly variable spatially and/or temporally are removed from the match-ups. For the remaining satellite image windows, average AOT measures are calculated within the windows and then compared against the means of the corresponding screened *in situ* AOT values.

6.2 PROCESSING OF *IN SITU* AOT DATA SETS

Quality assurance for *in situ* AOT measurements in the context of comparison against satellite-derived aerosol optical thickness values encompasses all activities concerned with radiometer calibration (Chapter 3); correction of sun intensity measurements (for sun photometers) and diffuse and global solar beam irradiances (for sky radiometers) to obtain AOT levels from digital counts captured by the instruments (Chapter 5); screening of AOT values and extraction of match-up points. This chapter concentrates on the last point from this list, the screening of radiometer AOT values and extraction of *in situ* points for comparison with satellite-derived aerosol properties. The processing operates on radiometer data which have already been calibrated and converted to AOT geophysical values. The screening of *in situ* AOT data sets includes the following explicit tasks:

1. the elimination of measurements with incomplete bands; the elimination of cloud-contaminated, erroneous, badly calibrated and badly corrected measurements; and the exclusion of atmospheres which significantly vary around the time of the satellite over-flight;
2. uniform and compliant processing for AOT data obtained from different radiometers and investigators; and
3. the averaging of temporal AOT sequences within stationary or discrete radiometer spatial coverages which correspond to ground geographical locations of the satellite sensor observation path.

The major processing steps involved in screening of *in situ* AOT values are shown in Figure 6.1. The consecutive stages of the *in situ* AOT screening strategy are described in the following sections.

6.3 REMOVAL OF MEASUREMENTS WITH MISSING BAND INFORMATION

The *in situ* AOT screening strategy uniformly processes measurements from any sun photometer and sky radiometer equipped with at least three bands within the ocean-color visible and near-infrared range of the electromagnetic spectrum. Different ground radiometers actually operate within different spectral bands. After the match-ups are obtained, a simple conversion is applied which maps instrument bands to corresponding satellite sensor bands, if these bands are different (Chapter 9). This enables a consistent comparison of radiometer and satellite aerosol optical information derived from the same portions of the spectrum.

Occasionally, some band information is missing from individual *in situ* measurements. Reasons for these missing bands include temporary radiometer and measurement faults, errors in information storage, and measurement downloading problems from the instrument. To successfully interpolate satellite spectral bands using radiometer band measurements, most of the radiometer band information should be present. Therefore, the current strategy discards the entire measurement if there are missing bands that are within the spectral range of ocean color.

6.4 ELIMINATION OF CLOUD CONTAMINATED AND ERRONEOUS MEASUREMENTS

Removal of cloud contaminated and erroneous measurements is fundamental to limiting the uncertainties associated with comparisons between radiometer- and satellite-derived aerosol properties. The objective for the algorithm design is that the screening procedure needs to work uniformly and efficiently with *in situ* AOT data obtained from different sun and sky radiometers and from different investigators. However, the creation of a unified approach to the analysis of AOT time sequences is not straightforward because of the variability of measurement styles employed for each instrument and operator. To test this unified approach, the results of multi-platform experiments are used where AOT data come from a number of sun photometers and sky radiometers operated concurrently.

AOT measurements are temporally screened throughout a day which enables extraction of observations that undergo rapid changes in time. These variable AOT counts can represent either:

1. cloudy atmospheric conditions;
2. incorrectly performed measurements; or
3. sudden aerosol plumes.

Although it is difficult to differentiate among these three conditions with AOT information alone, they are all undesirable for matching against satellite-obtained AOTs. This is because: cloud contamination masks aerosol information; failed observations cause distorted AOT measurements; and sudden aerosol plumes create spatial and temporal variations in atmospheric characteristics. The variations from aerosol plumes contribute to the uncertainties in comparing radiometer and satellite-derived aerosol properties due to time and viewing geometry differences between the two types of observations.

Automatic sun and sky radiometers, such as Shadow-band and CIMEL, normally provide both cloud-free and cloud-contaminated data. They rarely fail to perform their measurements correctly. Observations taken from hand-held sun photometers occasionally fail due to the difficulties in pointing the instrument into the solar disk from an unstable ship platform. With hand-held sun photometers, an operator's incorrect judgment of clear skies and other unfavorable measurement conditions can also result in cloud-contaminated observations. Effects of cloud contamination and erroneous observations are not different in terms of temporal AOT irregularities. Therefore, both of these conditions are treated in the same manner so as to limit the uncertainties concerned with radiometer and satellite-derived AOT comparisons.

The boundary between cloud-contaminated and cloud-free AOT measurements can be very fuzzy. It is most desirable to eliminate all clouds, including those most troublesome, like high cirrus, and leave all aerosol types for the benefit of further comparisons with aerosol properties attained from a satellite. Unfortunately, with the limited AOT information, some cloud measurements, including thin stable cirrus, are found to be indifferent from clear AOT observations. The ability to differentiate clouds using ocean color sensors is also imperfect. Only a very weak cloud contamination, such as high thin cirrus, may not contribute to notable errors in the match-ups.

Cloud screening and removal of erroneous measurements relies on the analysis of time sequences of AOT observations. The approach assumes that clear AOT values cannot undergo rapid changes in time and space, except for narrow plumes which are discarded as clouds during the processing. The smoothness criterion, which limits sudden increases and decreases in AOT measurements, is usually implemented by placing thresholds on AOT variations throughout a day or within shorter AOT sequences. The current study examines a few statistical and signal processing methodologies to find the most comprehensive and effective method to screen *in situ* AOT data.

Although only direct sun observations from the CIMEL sun and sky radiometer have been used so far, the instrument also measures sky radiances in solar almucantar and plane parallel. From the diffuse solar radiation, properties of aerosol scattering optical thickness, aerosol size distribution and phase function can be calculated. Although sky radiances are not captured each time

a sun observation is performed, it may be beneficial for future studies to consider CIMEL sky radiance measurements for the purpose of cloud screening.

A set of AOT observations for a single day is shown in Figure 6.2. In this figure, CIMEL measurements were taken from the AERONET and SIMBIOS site at Bahrain. SIMBAD, Shadow-band and MicroTops measurements were collected by different operators at the same location during an oceanic cruise experiment. This experiment, AEROSOLS'99, was conducted at the beginning of 1999. Measurements taken by automatic sun and sky radiometers, CIMEL and Shadow-band, are uniformly spread throughout the day. Frequency and daily distribution of observations captured with hand-held sun photometers, SIMBAD and MicroTops, fully depend on an individual investigator's schedule, atmospheric conditions, and judgment of the clear skies. For these analyses, the validation of the cloud screening is accomplished using a Micropulse Lidar (MPL) which operates at 523 nm (see Chapter 2). The MPL detects cloud-base and layer boundary altitudes (to the limit of signal attenuation) and measures several physical and radiative parameters including scattering/extinction cross-section profiles and optical thickness. The validation procedures described here use MPL's normalized relative backscatter data processed by Judd Welton from the MPL-Net Project that are available for from the GSFC MPL web site. In addition, the SIMBIOS project has a database of AOT observations obtained from Shadow-band, MicroTops, and SIMBAD radiometers during the AEROSOLS'99 and Indian Ocean Experiment (INDOEX) campaigns in the Atlantic and Indian Oceans, respectively. The radiometers collected data from the NOAA ship R/V Ronald H. Brown. The MPL was also operated on board the ship. However, CIMEL measurements cannot be validated using the MPL. The following sections will describe cloud screening and erroneous measurement removal algorithms studied for the match-up application.

Statistical Estimates Of Daily AOT Variation

The CIMEL sun and sky radiometer was the first type of instrument from which data were analyzed and matched against SeaWiFS derived AOT values (Wang et al., 2000). An algorithm was then designed to screen daily CIMEL observations. CIMEL AOT measurements are proportionally spaced in time but contain a large share of cloud-contaminated data. The CIMEL algorithm only accepts days which are statistically stable. These days are expected to have cloudless atmospheric conditions, since clouds moving through the sky increase the variability in the CIMEL measurements. The stability of the atmosphere is examined within the time from 3 hours before to 3 hours after the SeaWiFS over-flight. Even stricter conditions are then imposed on the AOT swivels within ±1 hour off the SeaWiFS over-flight. The constraints on the atmospheric variability are shown in Figure 6.3, where τ denotes a sequence of AOT observations and SO is the satellite over-flight time.

This statistical screening of the temporal distribution of *in situ* AOT daily levels is independent of the instrument type and the measurement style. The only requirement is that the number of measurements performed per day within ±1 hour off the satellite over-flight needs to be higher than two. The algorithm evaluates relative uniformity of the atmosphere over several hours. Comparatively minor variations in AOT values will not be distinguished, although they can indicate cloud contamination. However, a single occurrence of a relatively significantly cloudy or erroneous measurement will cause the whole day to be classified as cloudy and rejected.

To reduce drawbacks associated with the measurement generalization, this statistical test can also be applied within smaller temporal segments of the AOT observation sequences. A sliding filter of a certain radius of R - the number of AOT observations - is passed through a daily AOT sequence, as sketched in Figure 6.4. AOT statistics are computed within the filter. If $\sigma \leq 0.1$ and $\frac{\sigma}{\tau} \leq 0.2$ then the central AOT measurement within the filter is accepted as cloudless and valid. When the whole day of observations is processed, the remaining cloud-free measurements are further analyzed. The analysis is based on the assumption that there can be some passing clouds in a good measurement day, which is otherwise atmospherically stable. These cloudless AOT measurements can then compare well against satellite-derived aerosol estimates. If there are more than two clear AOT measurements within ±1hour off the satellite over-flight, they are again checked for the overall stability of the atmosphere within the two hour interval. If the atmosphere is temporally uniform, the cloud-free measurements are averaged and their mean observation time is computed.

Compared to generalized daily statistical screening, the method based on the analysis of measurement segments within a sliding filter is

more sensitive to local variations within AOT observations. Thus, it can detect less conspicuous cloud contamination. Also, the approach only rejects segments of AOT measurements which contain cloudy and erroneous data, not the whole day's worth of observations.

The drawback of the sliding filter method is that it is sensitive to the temporal spacing of the measurement, therefore, its application depends on the instrument type and the way the measurements are performed. To obtain comparable screening results verified against MPL observations, a different filter radius had to be applied for different sun and sky radiometers. The screening of Shadow-band measurements used the filter with R=5; for the MicroTops sun-photometer, R=5; for the SIMBAD instrument, R=2; and for the CIMEL sun-photometer, R=3. Figure 6.5 shows the comparison of MPL backscatter data and AOT statistical screening for different radiometers using the sliding filter method with the corresponding radii. MPL, Shadow-band, MicroTops, and SIMBAD were operated concurrently from aboard the NOAA ship R/V Ronald H. Brown which took part in the AEROSOLS'99 campaign. The CIMEL measurements were captured on a different day and come from the AERONET/SIMBIOS site at Bahrain. For the Bahrain measurements, there are no MPL data to validate CIMEL's AOT screening. The filter radii were specially fitted to suit the style of hand-held sun photometer and automatic radiometer operation during the AEROSOLS'99 and INDOEX cruises. Different investigators and atmospheric conditions may cause the optimal parameters of the method to differ.

For the purposes of the SIMBIOS Project, there are limitations associated with the statistical screening of AOT variations, and a search for the optimal algorithm for elimination of cloud-contaminated and erroneous measurements continues. The aim of this search is to find an algorithm that provides a uniform and standardized AOT processing for all instruments and data sets.

Derivative Estimates Of AOT Variation

The numerical differentiation of digitized signals has found many applications in analytical signal processing. In signals containing peaks, the amplitude of the n^{th} derivative is directly proportional to the amplitude of a peak and inversely proportional to the n^{th} power of the peak's width. Therefore, differentiation can be applied to discriminate against broad temporal features in favor of narrow components, such as sudden cloud signatures and erroneous AOT measurements.

The first derivative of a signal is the rate of change of the signal, τ, with time, t, that is $\frac{d\tau}{dt}$ which is interpreted as the tangent of the slope to the signal at each point in time. The second derivative is a measure of the curvature of the signal. It provides information on the rate of change of the slope of the signal between convex and concave, and the location of inflection points. Higher derivatives enable the detection of weak signal variations in the presence of noise and strong background interference, such as general daily AOT trends. The numerical expression to calculate the first derivative is given in Equation 6.1 as

$$\tau_i' = \frac{\tau_{i+1} - \tau_i}{t_{i+1} - t_i}. \qquad (6.1)$$

Derivatives are used to evaluate the smoothness of daily AOT observations. In the current study, first, second, and third derivatives of daily AOT sequences are analyzed. Limits are imposed on variations in the magnitude of the three derivatives. Also, a methodology implemented in the operational quality control of CIMEL data for the AERONET database is studied (Smirnov et al., 2000). In this technique, a norm of the second derivative, as defined in Equation 6.2, and the logarithmic second derivative are restricted by thresholds. Threshold values are obtained from experience with differentiating AOT temporal sequences for different optical atmospheric conditions. For the three-derivatives study, thresholds are established for different sun and sky radiometers through the evaluations of screened results with MPL backscatter data. For the CIMEL-originated quality control strategy, thresholds are directly borrowed from the AERONET algorithm.

$$\|D_2\| = \sqrt{\int_{t_1}^{t_2} \left(\frac{d^2\tau(t)}{dt^2} \right)^2 dt}. \qquad (6.2)$$

A significant drawback of the AOT sequence differentiation is that derivatives and derivative norms are calculated relative to the time of AOT capture; therefore, the method is sensitive to the temporal spacing of the measurements. These algorithms are better suited to work with AOT data obtained from automatic sky radiometers, such as Shadow-band and CIMEL, because their measurements are proportionally spaced through time. With data from hand-held sun photometers, unequal spread of AOT daily observation causes

under-representation or exaggeration of extracted peak features within the signal. This forces determination of individual thresholds for different instruments and data sets which in turn limits the ability to generalizate the algorithm.

Figure 6.6 highlights the difficulties in generalizing the AOT screening method based on derivatives. The figure displays screening results for the Shadow-band radiometer, MicroTops sun photometer, and SIMBAD sun photometer which acquired concurrent data during the AEROSOLS'99 campaign and an independent CIMEL radiometer. The algorithm applied limits on variations in the first, second and third derivatives. This particular screening used the same threshold values for all the instruments. The threshold for the first derivative is 0.5, for the second derivative it is 100, and for the third derivative is it 100,000. The screening result can be compared with the MPL response and the performance of the statistical algorithm presented in Figure 6.5. Figure 6.6 shows that in the case of Shadow-band and CIMEL radiometers, when compared to the MPL backscatter data, many cloudy AOT measurements were left out by this trial version of the screening procedure. With MicroTops and SIMBAD, too many observations were classified as cloud contaminated and removed. Therefore, these common thresholds could not benefit all the instruments.

Similar trials were performed with the AERONET algorithm. A norm of the second derivative and the logarithmic second derivative were restricted by the CIMEL-originated quality control thresholds. The method screened well Shadowband AOT observations which was verified against the MPL backscatter information. It also appeared to work successfully with CIMEL data for which the strategy was designed. However, the algorithm failed at screening MicroTops and SIMBAD AOT measurements. The imposed thresholds forced the classification of all cloudy and cloudless observations as cloud contaminated and their removal from the data set. The derivative-based screening approach can work well with particular AOT sequences, mainly those from automatic radiometers, however, the algorithm requires varying thresholds for different hand-held instruments and data sets.

The derivative method can be used in combination with a sliding filter, as shown in Figure 6.4. Both the first, second, and third derivative test and the second-derivative AERONET test can be applied within the filter. A common threshold is imposed on derivative functions for the entire AOT sequence within the sliding filter coverage. The filter expands the coverage of the temporal AOT stability limits as compared to using the first, second, and third derivatives alone (the highest third derivative combines information from four AOT measurements). The filter also defines the t_1 and t_2 limits for the AERONET test in the integration in Equation 6.2. Corresponding logarithmic second derivatives are then computed within the filter. The filter method enables immediate location of cloudy or erroneous AOT measurements within the daily observation sequence. The result of Shadow-band screening using derivative threshold values defined previously and a sliding filter with R=2 is displayed in Figure 6.7. Unfortunately, the sliding filter radius needs again to be individually established for AOT data from different radiometers and data sets.

As shown in Figure 6.7, the results of the AOT screening algorithm based on AOT sequence derivative limits compares well against MPL data. However, the method can not be generalized enough to be used in a simple and integrated form with all sun and sky radiometers and data sets.

Fourier Filter

A daily AOT measurement sequence can be treated as a time-domain signal and its plot as a time-amplitude representation of the signal. The Fourier transform enables the representation of the signal in the frequency domain. The Fourier filter is a type of smoothing function which limits high frequency components of the signal from the signal's frequency domain representation. It is assumed that the frequency components of the genuine signal, in our case a cloudless AOT daily sequence, fall predominantly at low frequencies. Noise in the signal, defined as sudden increases and decreases in AOT measurements which indicate cloudy and erroneous observations, falls primarily at high frequencies. High frequencies are then eliminated from the signal's power spectrum and the inverse Fourier transform of the signal is computed.

The Fourier filter has turned out to be useful for smoothing daily sequences of AOT measurements. It enables the entire signal to be represented only by lower frequencies which reduces the amplitude of the cloudy and erroneous AOT peaks. The general trends in the signal at different frequencies can be analyzed. However, the algorithm is only useful for stationary signals where the frequencies do not vary with time. In the Fourier transform, as signal time information does not exist, it is impossible to determine when in time certain frequency components appear. Because of this, high frequency measurements cannot be located and

eliminated from the time-domain AOT sequence. Consequently, the Fourier filter was abandoned as a screening method for cloudy and erroneous AOT measurements. An example of AOT observation smoothing using the Fourier filter is displayed in Figure 6.8.

Ångström Component Variability

The spectral distribution of Ångström components for the 12 aerosol models used in the atmospheric correction of SeaWiFS ocean color imagery is shown in Figure 6.9. The values of the Ångström component range from -0.05 to 1.5. It has been studied whether the Ångström coefficient of cloudy AOT measurements can be separated from pure aerosol Ångström values. The Ångström coefficient can be calculated in two ways. The first method is to linearly fit the Ångström value through all sun and sky radiometer spectral bands within the <440 nm, 870 nm> domain. The second method is to compute the Ångström coefficient, α, for each spectral band, λ, within the same domain relative to the 865 nm band according to Equation 6.3,

$$\alpha(\lambda) = \frac{\ln\left(\frac{\tau(\lambda)}{\tau(865)}\right)}{\ln\left(\frac{865}{\lambda}\right)}. \qquad (6.3)$$

Limiting the spread in the Ångström component to <-0.05, 1.5> does not eliminate cloudy and erroneous AOT measurements. Clouds can also be represented by low Ångström component values as verified with the MPL backscatter data. Therefore, the test on Ångström component variability is not used to eliminate cloud-contaminated and erroneous AOT observations.

Wavelet Transform

A daily AOT measurement sequence is again treated as a time-domain signal. The wavelet transform combats the problems encountered with the Fourier transform by simultaneously providing time and frequency representation of a signal (Combes et al, 1989). The transform is used to analyze non-stationary signals. Sequences of AOT observations are non-stationary because they contain time-varying frequency components.

The wavelet transform supports a multi-resolution analysis. A signal is analyzed at different frequencies and time intervals at variable frequency and time resolutions. The transform provides good time resolution at high frequencies and good frequency resolution at low frequencies. This is based on two observations. The first being that a high frequency component can be better located in time than a low frequency component. Secondly, a low frequency component can be better located in the frequency domain compared to a high frequency component. With the wavelet transform, frequency components existing at any given time interval can be extracted and analyzed separately.

The mathematical representation of the wavelet transform uses two parameters of translation and scale (Masters, 1995). The translation relates to the location of a window which is shifted through the signal and convolutes the signal with its window function. The scale parameter substitutes for the frequency parameter. High scales (low frequencies) dilate the signal and correspond to global information about the signal. Low scales (high frequencies) compress the signal and provide detailed information on hidden patterns in the signal. There are many examples of mother wavelet functions which can be used as the prototype for the windows in the convolution process. Child wavelets are dilated or compressed and shifted versions of the mother wavelet. These mother wavelet functions include the Morlet and the Mexican hut functions. The current study uses the Daubechies wavelet because a discrete wavelet transform based on the Daubechies function is a built-in function in the Interactive Data Language (IDL) software. The present application is fully implemented in IDL.

The discrete wavelet transform, DWT, is implemented through subband coding. The procedure starts by passing the signal through a half-band digital lowpass filter with impulse response H(n) and a half-band highpass filter with impulse response G(n). The half-band lowpass filter removes all frequencies in the signal that are above half of the highest frequency contained within the signal while the half-band highpass filter removes the frequencies below half of this highest frequency. After passing the signal through the half-band filters, half of the samples in the signal can be eliminated according to Nyquist's rule because the signal now has half of the original bandwidth. Discarding every second measurement subsamples the original AOT sequence by 2. The result of the half-band lowpass filter is further passed through the same lowpass and highpass filters from the first step and subsampled by 2 for further decomposition. The application of the lowpass and highpass filters in this manner continues until the signal can not be subsampled further. At each iteration, the decomposition halves the signal time resolution because there is only half the number of samples left in the signal. The

successive decomposition also doubles the frequency resolution because the bandwidth of the new signal spans only half of the previous interation's band width. The subband coding of an AOT sequence, τ, which contains the highest frequency, f, equal to π radian per second is visualized in Figure 6.10.

To apply the subband coding effectively, the number of samples in the sequence (i.e. the number of daily AOT measurements) is required to be a power of 2. Because this is usually not the case, the sequence must be padded with zeros to produce the required number of samples. The discrete wavelet transform of a MicroTops II AOT observation sequence is shown in Figure 6.11.

The discrete wavelet transform of the MicroTops AOT observations shown in Figure 6.11 has 64 coefficients. The locations of the coefficients are related to the positions of the results of the lowpass and highpass filtering as explained in Figure 6.10. The last 32 coefficients of the wavelet are the results of the first level highpass filtering. The 16 coefficients to their left are the product of the second level highpass filtering of the first level lowpass result. The 8 coefficients to their left are the outcome of the third level highpass filtering of the second level lowpass response. Within the 6^{th} level filtering, there are only 2 coefficients where one is a single highpass and the other a single lowpass result. The single lowpass result is the first coefficient (coefficient 0) in the wavelet representation. The frequencies which are most prominent in the original signal appear as high amplitudes in that region of the discrete wavelet transform which includes those particular frequencies. It can be seen from Figure 6.11 that the lowest frequencies in the AOT measurement sequence, around $1/64^{th}$ of the maximum frequency, are the most prominent in the MicroTops AOT distribution from the 11^{th} of March 1999. The second most common frequencies within this signal are between $1/16^{th}$ and $1/8^{th}$ of the maximum frequency. High frequencies occur less often in this data set.

Low frequency components within AOT daily distributions can be easily located in the frequency domain because they appear as initial coefficients in the signal's discrete wavelet representation. The most prominent frequencies within AOT sequences are found to be the lowest frequencies which appear in the transform as high wavelet peaks. The high frequency components are better located in the time domain because the AOT time representation exhibits a lot of cloudy or erroneous measurement peaks.

Because cloud-contamination and erroneous observations result in rapid AOT changes in time, these variations can be correlated to higher frequencies within the AOT daily distributions. The Fourier filter analysis shows that clear AOT measurements are actually represented by a small fraction of frequencies in the lower end of the spectrum. The wavelet transform provides a good frequency resolution at low frequencies, therefore, the AOT signal can be studied in detail at these lower frequencies while the measurements corresponding to higher frequencies can be safely discarded as cloudy or erroneous. The frequency content associated with consecutive AOT observations is studied using the discrete inverse wavelet transform. The inverse transform is applied to the AOT signal within discrete frequency ranges. Only those transform coefficients are considered which correspond to successive frequencies of interest in the signal. The coefficients represent the result of highpass filtering the original signal and highpass filtering the lowpass response from the previous level's convolution. The coefficients from each level's highpass filtering are used to produce the inverse transform of the AOT sequence while all other coefficients are set to zero.

The inverse wavelet transforms of a Shadow-band signal from the lowest up to the highest frequency components are displayed in Figure 6.12. The top left-hand-side graph in the figure shows a daily distribution of Shadow-band AOT measurements. The top right-hand-side graph gives the discrete wavelet transform of this AOT distribution. From the wavelet representation it can be seen that the most prominent frequencies in the original signal are the lowest frequencies between $1/256^{th}$ and $1/128^{th}$ of the signal's highest frequency. Graphs in the following rows give inverse wavelet representations of the original Shadow-band measurements. The graph on the left in the second row represents the inverse wavelet transform of the AOT sequence confined to the lowest and most prominent frequencies. This is the result of the 8^{th} level averaging of the AOT observations with the lowpass filters. The graph illustrates that these lowest frequencies are representative of all daily AOT measurements. These principal frequencies give a very coarse approximation of the trend in the original AOT signal and correspond to broad temporal features, which for AOT data, are commonly the clear-sky atmospheric background. The graph on the right in the second row represents the inverse wavelet transform of the AOT distribution limited to the frequencies between $1/128^{th}$ and $1/64^{th}$ of the

highest frequency obtained from the 7^{th} level convolution. The AOT sequence represented in the 6^{th} level frequencies between $1/64^{th}$ and $1/32^{nd}$ of the highest frequency is shown on the left-hand-side of the third row of graphs. The following graphs in the fourth and fifth rows show the signal at increasingly larger domains of higher frequencies. The final right-hand-side graph in the last row represents the AOT sequence restricted to a bandwidth ½ up to the highest frequency present in the signal after the 1^{st} level highpass convolution. The inverse wavelet representation at these frequencies falls to zero for some AOT measurements because the measurements within the sequence do not contain such high frequencies. Conversely, high peaks in this inverse transform characterize high frequency AOT signals, such as the AOT observations taken around 2pm.

The inverse wavelet representation of AOT sequences within different frequency ranges illustrates those frequencies which are present within each part of the signal defined by subsequent AOT measurements. The inverse wavelet transform straddles zero if the AOT observations do not contain the corresponding frequency ranges. Peaks in the inverse transform relate to measurements which are inundated with these frequencies. The wavelet properties make it possible to examine inverse AOT signals for higher undesirable frequencies and to find a frequency borderline between clear and cloud-contaminated measurements.

The borderline frequency between clear and cloud-contaminated or erroneous AOT measurements was studied using data from different sun and sky radiometers and different investigators. MPL backscatter information was used for validation of the wavelet screening strategy for the Shadow-band, MicroTops and SIMBAD instruments. No MPL backscatter data were available for CIMEL measurements. A good estimation of inverse wavelet values which straddle zero was found by limiting inverse transform peaks to <-0.01, 0.01> in amplitude. The frequency resolution available within the wavelet representation depends on the number of samples in the signal. The higher the number of daily AOT measurements the more detailed the frequency resolution at lower frequencies. The absolute frequencies extracted from the AOT sequence are fractions of the maximum frequency present within the signal. Therefore, for each daily AOT observation the frequency resolution of the wavelet transform varies with the number of measurements and absolute frequency values depend on the maximum frequency present. These conditions coupled with the inverse wavelet frequency spectrum of consecutive AOT observations distinctly define the AOT signal. It is therefore always possible to place a borderline on the same proportion of frequencies defined by lowpass and highpass convolution levels. Although the borderline absolute frequency values are then specifically tailored for individual AOT distributions, the choice criterion is always constant.

Figure 6.13 illustrates MPL backscatter information and Shadow-band, MicroTops and SIMBAD original and screened measurements for the same day during the INDOEX cruise. Also, original and screened diurnal CIMEL observations are given for the Bahrain site shared by the AERONET and SIMBIOS Projects. The borderline frequency used in the screening is just above $½^{M/2}$ of the highest frequency present in each AOT signal, specifically $½^{3M/7}$, where M is the number of highpass and lowpass filtering levels defined by the subband coding in Figure 6.10. The AOT measurements which contain frequencies between the borderline and the highest frequency are removed as cloud-contaminated or erroneous. These measurements are found as peaks in the inverse wavelet representation of the AOT distribution corresponding to these frequencies.

The MPL backscatter data illustrates that 10 March 1999 was a very clear day in the Indian Ocean over the NOAA ship R/V Ronald H. Brown except for a few scattered clouds about 8am, after 10am, and around 11:30am. These clouds show up as red spots in the backscatter plot. The wavelet screening eliminated these cloud-contaminated aerosol peaks from the Shadow-band measurements. From the MicroTops data, cloudy and erroneous AOT observations were deleted because they appeared as outliers with noticeable temporal variabilities. A set of SIMBAD AOT measurements was ruled out as cloud-contaminated or erroneous either because of its sudden increase in AOT values or its correspondence to the 11:30am cloudy period. Frequent Shadow-band observations demonstrated a rising trend in the AOT distribution for this day from 9am towards the afternoon. It may have been possible to classify SIMBAD measurements past 11am as clear if there had been more observations available. Finally, unstable AOT data were excluded from the CIMEL measurements captured on a different day and at a different geographical location. Both sudden increases and falls in CIMEL AOT values after 9am gave an inconsistent representation of the atmosphere and were all removed.

The borderline frequency of just above $\frac{1}{2}^{M/2}$ of the highest signal frequency was found to be the most suitable for wavelet screening of cloud-contaminated and erroneous AOT daily observations. This borderline frequency value was validated against MPL backscatter data which provided a stringent basis for elimination of cloudy measurements and extraction of uniform atmospheric conditions. The approach provides the same AOT processing irrespective of instruments and operator preferences. AOT measurements taken from any sun and sky radiometers and from within any current and future data sets can be screened using identical wavelet algorithm parameters.

Although the borderline frequency of just above $\frac{1}{2}^{M/2}$ of the highest frequency within the AOT sequence fits the best, more or less stringent borderline frequencies can also be applied for different screening purposes. Higher borderline frequencies, for example, will force the acceptance of additional degrees of temporal atmospheric variability and may pass some lightly cloudy or erroneous AOT measurements.

Concluding, the wavelet approach can be used for temporal screening of any sets of oceanic, coastal, and continental aerosol measurements. The method uniformly removes cloud-contaminated and erroneous AOT observations from data originated from any sun and sky radiometers and using any instrument operation schemes. The overall algorithm accuracy can be adjusted by varying a single parameter of borderline frequency. The borderline frequency is set as a universal ratio number, however, its absolute value is dependent on the amount of daily AOT measurements and the maximum frequency present in the AOT signal. The method relies on the inverse wavelet estimation of the frequency spectrum within consecutive AOT observations. The borderline frequency validated against MPL backscatter information is just above $\frac{1}{2}^{M/2}$ of the highest frequency present in each daily AOT sequence. However, other numbers for the borderline frequency can also be chosen for different AOT screening applications.

6.5 EVALUATION OF SCREENING ALGORITHMS

The purpose of screening strategies is to uniformly eliminate cloud-contaminated and erroneous AOT measurements from sequences of AOT observations which come from different sun and sky radiometers and data sets. There are three algorithms which have been found useful for this implementation. These algorithms are based on statistical and derivative estimates of daily AOT variations as well as the wavelet screening which relies on elimination of measurements characterized by large amplitudes in the frequency range.

Comparison Of Screening Algorithms

The statistical algorithm investigates stability of the atmosphere within the entire AOT measurement period under consideration. The method can be consistently applied to AOT information from any instrument or data set. Its accuracy is limited by the constant thresholds imposed on the AOT signal variability because the statistical significance of different atmospheric features changes with the number of samples present in the dataset. In its basic form, the method is not a cloud-screening and erroneous-observation-removal approach because it may reject a whole day's measurements based only on a single AOT outlier. The modified version of the statistical algorithm which uses a sliding filter is a truer observation screening strategy, however, it cannot be universally applied to different instruments and data.

The derivative-based algorithms are very sensitive to temporal distributions of AOT observations. They work well with AOT measurements captured within equal time spans throughout a day. Such AOT data are usually obtained from automatic radiometers. The method requires different thresholds for different instruments and, in case of hand-held sun photometers, different data sets.

Finally, the wavelet transform approach requires the adjustment of a single general parameter of the borderline frequency ratio which is universal for all instruments and data sets. The wavelet strategy investigates both time and frequency distributions within the AOT signal. Therefore, it is able to extract frequency-dependent uniform atmosphere periods and relate them to consecutive AOT measurements in the time domain of the signal.

Figure 6.14 illustrates the comparison of daily AOT screening results performed by the three algorithms. The wavelet screening approach used the strict borderline frequency of just above $\frac{1}{2}^{M/2}$ of the highest frequency in the signal. The statistical method adopted the sliding filter utility. The derivative-based approach applied the norm of the second derivative, as defined in Equation 6.2, and the logarithmic second derivative as inspired by the AERONET quality assurance algorithm. The wavelet approach shows relative tolerance to small variations within AOT measurements whereas the statistical method appears less flexible. The

derivative-based algorithm seems to accept AOT observations which may indicate temporally variable atmospheric conditions.

All three *in situ* AOT screening strategies can be used successfully with radiometer aerosol measurements. However, as explained in detail earlier in this chapter, there are some limitations as to the application and accuracy of the statistical and derivative estimates of AOT variations. On the other hand, wavelet-based screening can be applied uniformly with any instruments or data sets and the method is well suited to extract AOT measurements which are characteristic of periods of atmospheric stability.

Comparison Against AERONET Quality Assurance

A comparison study was performed between the wavelet approach to AOT screening and the partly interactive quality assurance procedure created by the AERONET Project (Smirnov et al., 2000). The purposes of both SIMBIOS and AERONET screening strategies are different. The AERONET algorithm is designed to analyze CIMEL observations exclusively and preserve as much aerosol information as possible for the global aerosol studies. The aim of the SIMBIOS approach is to confidently compare *in situ* AOT measurements against satellite-obtained AOT values. The SIMBIOS screening method must operate for different instruments and strictly remove all observations suspected of being cloud-contaminated, erroneous or originated in atmospherically unstable periods.

Figure 6.15 shows an original set of daily CIMEL AOT measurements captured at the Goddard Space Flight Center AERONET site, thus it is not a coastal SIMBIOS site and is more characteristic of continental aerosols. The Figure also gives the results of the AERONET AOT quality assurance and the wavelet transform screening process using the stringent borderline frequency of just above $½^{M/2}$ and the less strict version of $½^{0.3M}$ of the highest frequency. It is seen that the AERONET approach accepts all low-in-value AOT measurements, within both stable and unstable atmospheric periods. The more rigid version of the wavelet algorithm only defines as clear those AOT observations which originate within temporally uniform atmospheric conditions. The last plot in the figure illustrates that the wavelet approach can virtually imitate the AERONET result by increasing the borderline frequency.

Wavelet screening results are produced using multi-band exclusion criteria which are explained in detail in Section 6.6. If the AERONET AOT quality assurance applies a single spectral band to select clear AOT values, the additional difference in the results can be explained from stricter multi-band inspection of diurnal AOT variabilities used by the wavelet algorithm.

In general, the final average of daily cloud-free AOT values is similar for both SIMBIOS and AERONET algorithms. However, the SIMBIOS protocol must be stricter in removing variable aerosol conditions due to its specific goal to provide *in situ* data for calibration and validation of satellite retrievals.

6.6 CHOICE OF SPECTRAL BANDS USED IN AOT SCREENING

The initial scheme for elimination of cloudy and erroneous AOT measurements was applied with CIMEL sun and sky radiometer data (Wang et al., 2000). This strategy was based on statistical estimates of AOT variations throughout a day and only used one spectral band (870 nm) of the CIMEL radiometer to analyze those variations. The assumption was that the 870 nm band sufficiently defined clouds and possible erroneous measurements.

When choosing spectral bands for AOT screening, several possibilities need to be considered:

- the band calibration and AOT processing;
- the magnitude of the AOT value; and
- the spectral signature of erroneous, cloud-contaminated, and variable atmosphere AOT observations.

Despite clearly defined protocols (Fargion and Mueller, 2000), sun and sky radiometers with badly calibrated bands are in use and mistakes can be made in converting raw instrument measurements to geophysical AOT values. If only one or two bands are effected, it may be still useful to process AOT observations for removal of cloudy and erroneous data. It is beneficial to make available as many AOT measurements as possible to the temporal screening algorithm to enable a better judgment of daily aerosol distributions. If the problem occurs within the single band which is being used for AOT screening, then useful measurements may need to be rejected and the scheme may lose valuable information. Therefore, may be better not to dedicate a single and specified band for AOT screening purposes.

In general, the spectral distribution of non-absorbing AOT values monotonically increases from the near-infrared towards the visible range of the spectrum. Therefore, AOT measurements are lowest in magnitude around 870 nm compared to the other spectral ranges within the ocean color domain. Consequently, temporal AOT variations detected in the near-infrared are significantly accentuated in the visible. Also, some atmospheric conditions may appear clear and stable in the near-infrared while the visible spectrum may indicate the underlying atmospheric variability.

It may therefore be appropriate to use more than one spectral band to screen AOT observations for cloud-contamination and erroneous data. The 870 nm band alone may be insufficient in some cases to reliably remove clouds and erroneous measurements from diurnal AOT observations. The AOT screening strategies introduced in the current chapter impose their temporal stability criteria on both the single band around 870 nm, depending on the sun or sky radiometer, and the following fusion of bands:

- for the CIMEL, at least two bands must pass the screening criteria; and
- for all other instruments, more than half of the bands must pass the screening criteria.

All cloud-contamination and erroneous measurement screening results given in this chapter are based on the multi-band exclusion criteria.

Many studies and MPL backscatter validation indicate that the removal of cloud-contaminated and erroneous AOT measurements is more stable when more than half of the bands pass the screening criteria for Shadow-band, MicroTops, and SIMBAD instruments. However, despite the lack of MPL backscatter validation data, it appears that CIMEL calibration is very stable and two bands are sufficient to satisfy the exclusion criteria. Compared to AOT screening using only the 870 nm band, the multi-band approach produces less AOT match-up points with satellite data because less AOT observations pass the criteria. However, the AOT match-ups obtained with the multi-band analysis are more accurate in the visible range of the spectrum. This result is given and described in more detail in Chapter 8.

Concluding, it is possible to screen daily AOT measurements for cloud-contamination and erroneous observations using just a single spectral band of the instrument. The 870 nm band is the most recommended. A combination of a few bands can also be used. The application of multi-band screening criteria is stricter and it decreases the number of AOT measurements available for matching against satellite-derived aerosol properties. However, the multi-band approach is less sensitive to instrument calibration errors and mistakes in raw observation processing. This study indicates that the multi-band approach can also contribute to the extraction of spectral signatures of cloud-contaminated and erroneous AOT observations as well as AOT values which are characteristic of variable atmospheres and otherwise cannot be detected with single band analysis. However, these benefits of multi-band screening need to be further investigated.

6.7 SPECTRAL DISTRIBUTION ANALYSIS

Temporal measurement screening removes cloud-contaminated and erroneous AOT measurements from each set of daily AOT sequences. It involves AOT analysis only within a single or few radiometer spectral bands. The more AOT observations that comprise a daily AOT sequel, the more accurate the screening is. Therefore, all valid AOT observations are used in the temporal screening. No spectral distribution analysis of individual measurements has been yet performed and measurements which contain flaws in data in specific bands can be present which indicate badly calibrated or processed band information. Additionally, some *in situ* AOT observations involve continental types, absorbing, or questionable aerosols with large Ångström component values. These aerosols cannot be successfully matched against satellite-derived AOT measures because the ocean color atmospheric correction algorithms only include aerosol models with a low Ångström component, up to 1.5 in value. Therefore, the aim of the current stage in the *in situ* AOT processing for match-ups with satellite aerosol properties involves spectral examination of individual AOT measurements which pass the temporal screening test.

The spectral distribution analysis of AOT measurements encompasses studies of the Ångström component for successive sun or sky radiometer bands within the ocean color spectrum. Only those AOT observations are investigated which passed the temporal screening test and thus represent correct and cloud-free aerosol measurements. Although some temporal screening algorithms, such as the wavelet transform, are most effective with the entire set of all daily AOT observations, it is now efficient to limit the amount of AOT data to those which come from a certain period around the time of the satellite over-flight. This is because the final daily *in situ* AOT point to

be compared against the satellite-derived AOT value is calculated by averaging AOT measurements. These are the measurements which pass all the tests and are captured within a short time span surrounding the satellite observation of their geographical location. This short time span is chosen as ±1 hour in the current application.

For each AOT observation, a generalized Ångström component value is first obtained. The generalized Ångström coefficient is computed by finding a slope for a linear fit of the natural logarithm of AOT values at consecutive spectral bands to the natural logarithm of the corresponding bandwidths expressed in micrometers. The Ångström value is only calculated within the sun and sky radiometer <440 nm, 870 nm> spectral range. The linear fit method establishes the overall trend in the spectral distribution of the AOT observation in subsequent bands. The minimum value of the generalized Ångström component is limited to -0.05 for well calibrated and processed oceanic or coastal AOT measurements. Secondly, a condition is introduced which places a maximum value limit on the Ångström component. This condition regards specific Ångström coefficients which are computed for each spectral band within the <440 nm, 870 nm) domain relative to the 865nm band according to Equation 6.3. The maximum Ångström condition limits the value of the component to 2.5 for each radiometer band within the domain. It has been found that this maximum Ångström condition calculated for specific spectral bands is sufficient for bounding the AOT spectral distribution and no additional maximum value restriction needs to be placed on the generalized Ångström component. The maximum limit on the specific Ångström coefficients eliminates AOT observations with questionable spectral distributions which may originate from bad radiometer calibration, errors in raw measurement processing, and undesirable atmospheric conditions. Limiting the spread of generalized and band-specific Ångström component values enables rejection of *in situ* AOT observations characterized by questionable spectral distributions. These dubious distributions may indicate problems with calibration of individual spectral bands or their correction to geophysical values. These distributions can also be caused by aerosol types or other atmospheric conditions usually not accounted for in the processing of ocean color imagery. AOT measures derived in course of atmospheric correction of satellite data over oceans are bound by the aerosol models used in the processing. The models describe rather idealized aerosol types understood to exist over the oceans. Consequently, limiting *in situ* AOT measurements to only those which exhibit the desirable spectral characteristics ensures more confident comparisons of radiometer AOT values with satellite-obtained aerosol properties. These comparisons can then be used to draw conclusions about satellite sensor calibration and the accuracy of aerosol model propagation from the near-infrared towards the visible spectra. However, a less spectrally restricted collection of AOT radiometer measurements may be necessary to establish suitability of the set of aerosol models applied in the atmospheric correction of ocean color data. This is because aerosol types over the oceans can be more variable than the predictions from the idealized aerosol models. A statistical ability to fit all valid atmospheric conditions is required to accurately perform the atmospheric correction of ocean color imagery.

6.8 ANALYSIS OF TEMPORAL AND SPATIAL AEROSOL VARIABILITIES

So far, all daily valid AOT measurements have been temporally screened to remove cloud-contaminated and erroneous observations. The remaining AOT measures have been limited to those captured around the time of the satellite over-flight. They have also been spectrally analyzed to eliminate badly calibrated and processed observations as well as questionable aerosol representations unsuitable for matching against satellite-derived aerosol properties. The successful AOT measurements which pass these tests are further investigated. Sun and sky radiometers which collect AOT information can be mounted on a permanent station in a coastal region or on an island (e.g. AERONET/SIMBIOS CIMEL sun photometers) or used from a moving ship platform (e.g. Shadow-band, MicroTops, and SIMBAD radiometers). For a radiometer operated from a moving platform, the instrument's varying spatial coverages are considered. This is because AOT observations from different geographical locations need to be associated with different spatial windows extracted from satellite imagery. Discretezation of radiometer spatial coverage is established relative to the ground resolution of the ocean color sensor, size of image window extracts, and estimation of spatial variability of the atmosphere. To produce the results of this study, the atmosphere is considered approximately uniform along a 15km long ship track and the radiometer measurements obtained within ±1 hour

of the satellite over-flight are clustered into sets of 15km spatial coverage. However, the algorithm implementation is general enough to introduce the spatial extent of along-track atmospheric uniformity as a variable to the AOT processing procedure.

The described strategy separates sets of AOT measurements which are associated with discrete spatial coverages for sun and sky radiometers operated from a moving platform. For stationary instruments, a single AOT set is considered with a constant spatial coverage which encompasses all observations obtained within a short time span surrounding the satellite over-flight. Presently, this time span is ±1 hour. To be able to confidently match the extracted sets of AOT measurements against satellite-derived AOT values, atmospheric conditions around the time of the satellite over-flight above the radiometer must be stable. Therefore, within each AOT set, temporal uniformity of aerosol properties is investigated. The condition for aerosol invariability corresponds to the statistical AOT screening requirement for $\sigma \leq 0.1$ and $\frac{\sigma}{\tau} \leq 0.2$ as described in section 6.4. This additional atmospheric uniformity test is needed because the previous temporal and spectral measurement analyses, although they remove cloudy, flawed, and unsuitable AOT observations, may still pass clear and valid AOT data which are characteristic of quickly changeable aerosol distributions. The whole set of AOT measurements is rejected if the atmosphere is found unstable. In conclusion, this stage of the AOT measurement processing removes AOT data sets which represent aerosol conditions temporally varying around the time of the satellite over-flight. Discrete spatial coverages of the atmosphere are considered for radiometer observations performed from a moving platform. For stationary instruments, aerosol stability is tested within their constant geographical locations.

6.9 *IN SITU* AOT POINTS

If there are any AOT observations left after this final stage of *in situ* AOT processing, they should be valid, cloud-free, well calibrated and corrected, come from the range of aerosol distributions widely common in atmospheric correction of ocean color imagery, and be representative of spatially and temporally stable atmospheric conditions. If there are two or less AOT measurements left for each temporal and spatial set, this AOT set is rejected. If more than two AOT observations within each set pass all the tests, they all contribute to the final AOT data point. This single AOT point of *in situ* information is consequently matched against an individually processed satellite-derived AOT data point obtained for the corresponding time and geographical location. To obtain an *in situ* AOT point, AOT measurements are averaged for all spectral bands. Also, the mean capture time and geographical location are computed for the *in situ* point. Averaging the sets of AOT measurements completes the processing of *in situ* AOT observations and provides reliable sun and sky radiometer information for comparisons with aerosol properties which have been theoretically deduced from satellite imagery. The distribution of *in situ* AOT measurements can only be analyzed temporally and, for instruments based on a moving platform, within one spatial dimension. The distribution of satellite-derived AOT values can on the other hand be only studied spatially because of the large gaps between ocean color sensor revisit times over the same geographical location. These gaps prohibit detailed monitoring of temporal aerosol changes. Consequently, many of the obtained *in situ* AOT points may not match with their corresponding satellite-derived aerosol observations because the atmosphere may not appear as clear and stable spatially as it appears temporally. Also, appropriate satellite coverages may be missing. Nevertheless, the described processing of *in situ* AOT measurements creates a uniform and reliable processing scheme for observations from all sun and sky radiometers and the final AOT points can be confidently matched against satellite-derived aerosol properties.

6.10 CONCLUSIONS

The objective of the satellite sensor calibration and atmospheric algorithm validation requires the highest confidence in the *in situ* and satellite AOT data sets used in the comparisons. There are many uncertainties involved in assessing AOT measures from ground radiometers, aerosol data processing, and in comparing AOT values against satellite-derived observations. The SIMBIOS Project defined uniform and comprehensive strategies for radiometer protocols and AOT data processing for the match-ups. These strategies enable the minimization of AOT comparison uncertainties and make use of the large volumes and diversity of the collected *in situ* AOT information.

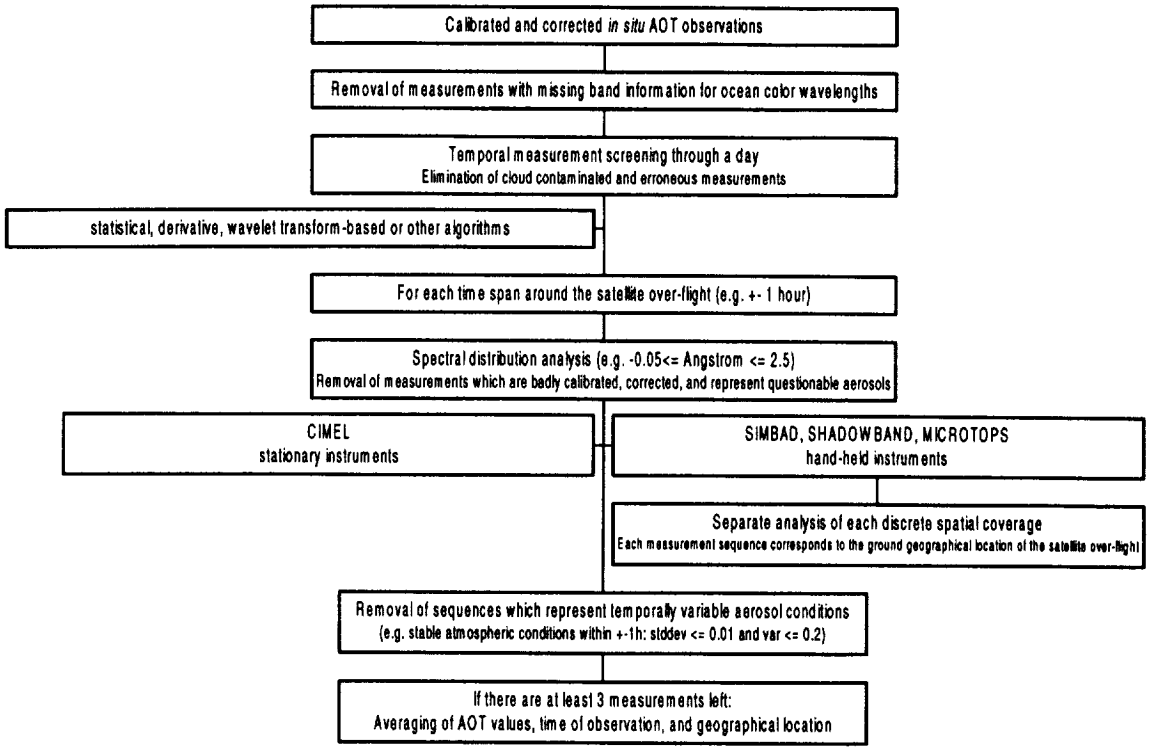

Figure 6.1. Sequence of *in situ* AOT screening operations.

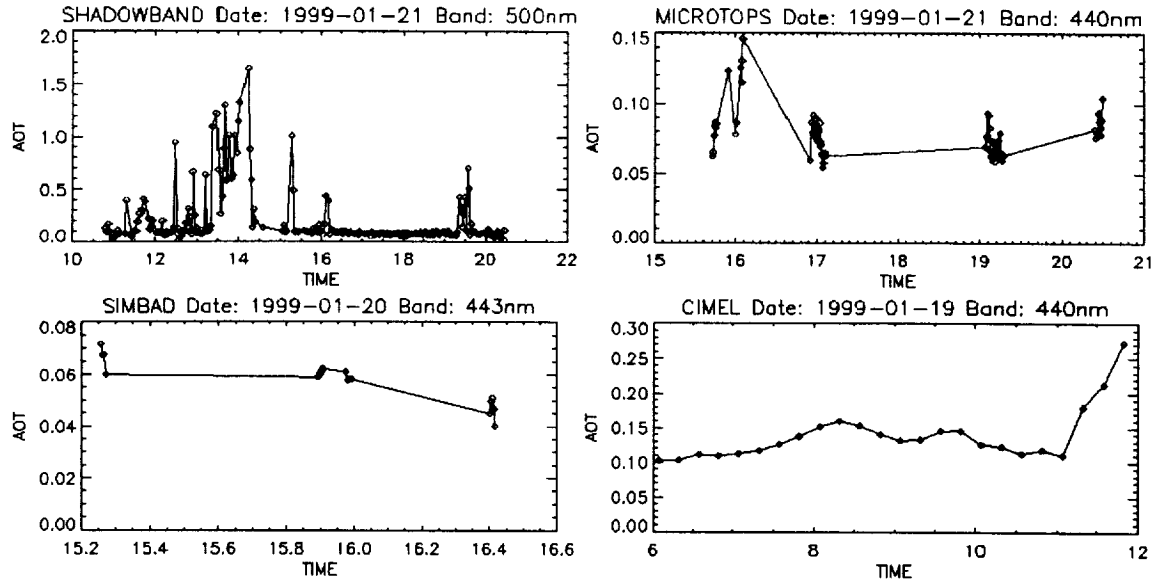

Figure 6.2. Daily sequences of AOT measurements for four sun and sky radiometers.

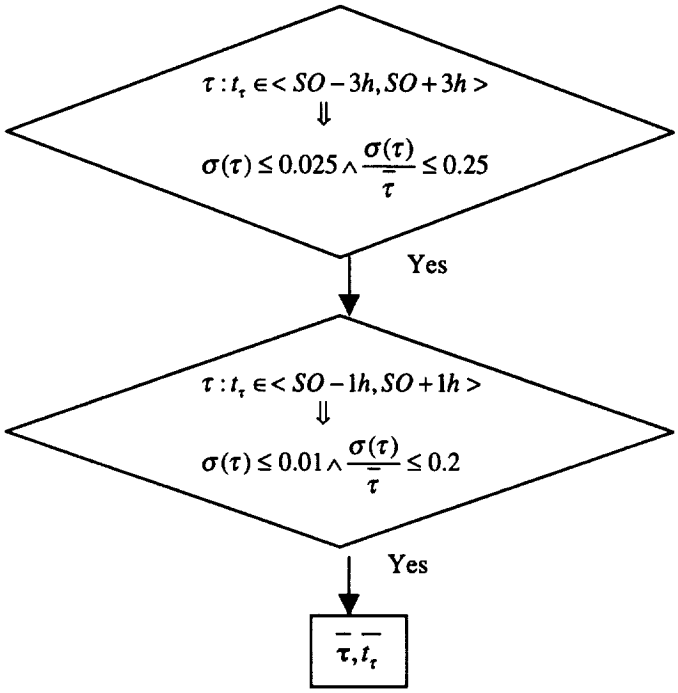

Figure 6.3. Statistical screening of daily AOT measurements.

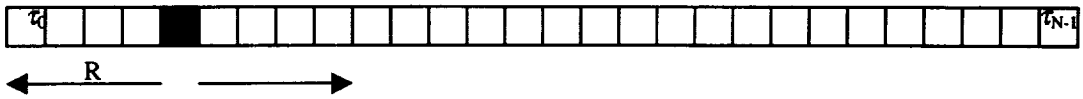

Figure 6.4. Screening of AOT daily observations with a sliding filer method.

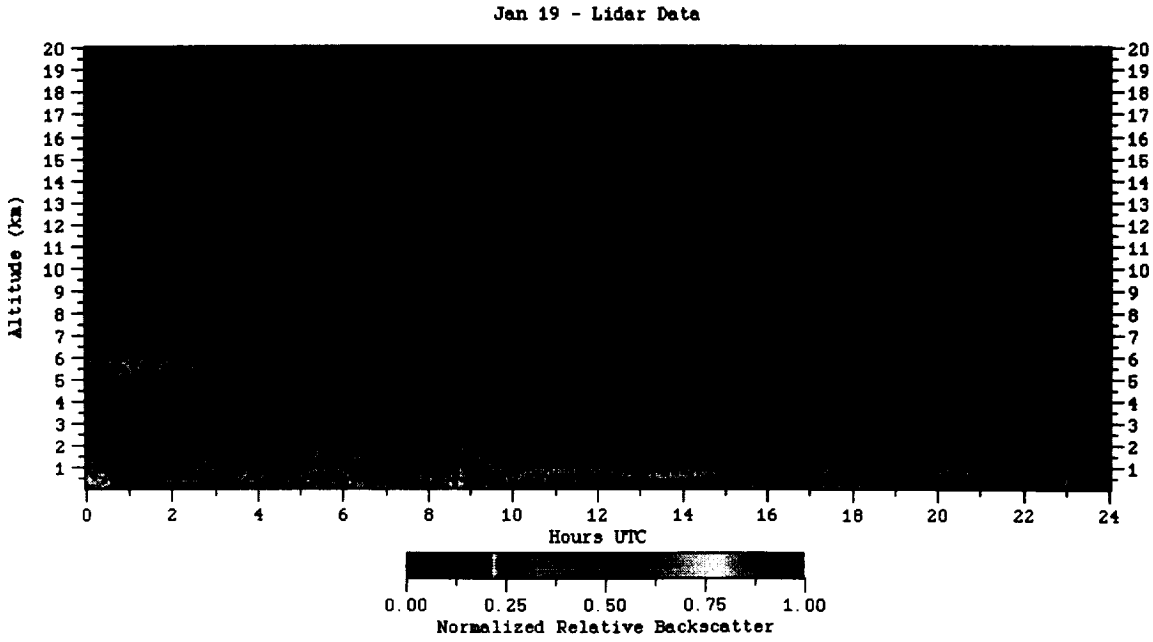

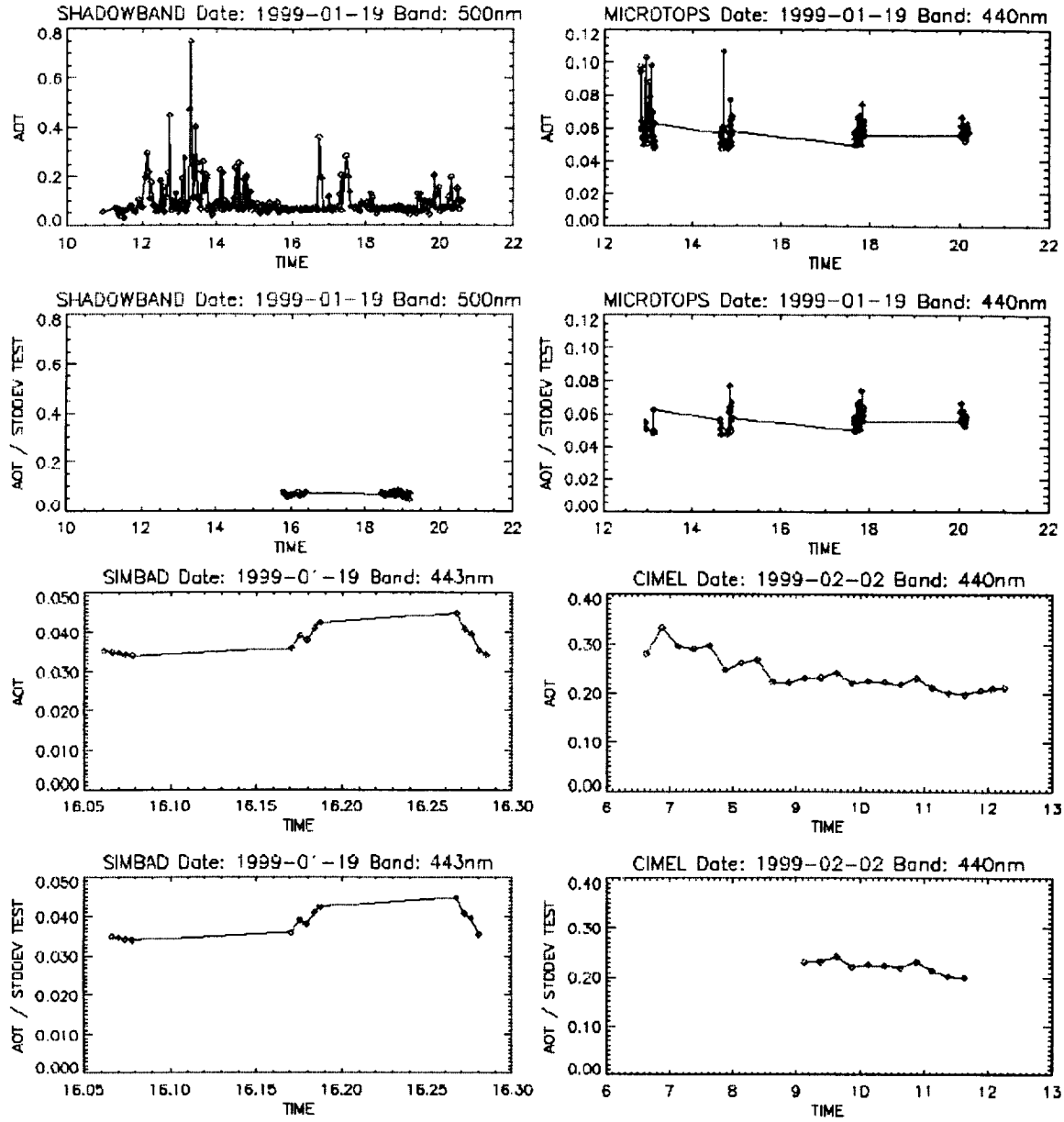

Figure 6.5. MPL data, original radiometer AOT observations, and corresponding statistically screened AOT measurements using the sliding filter method.

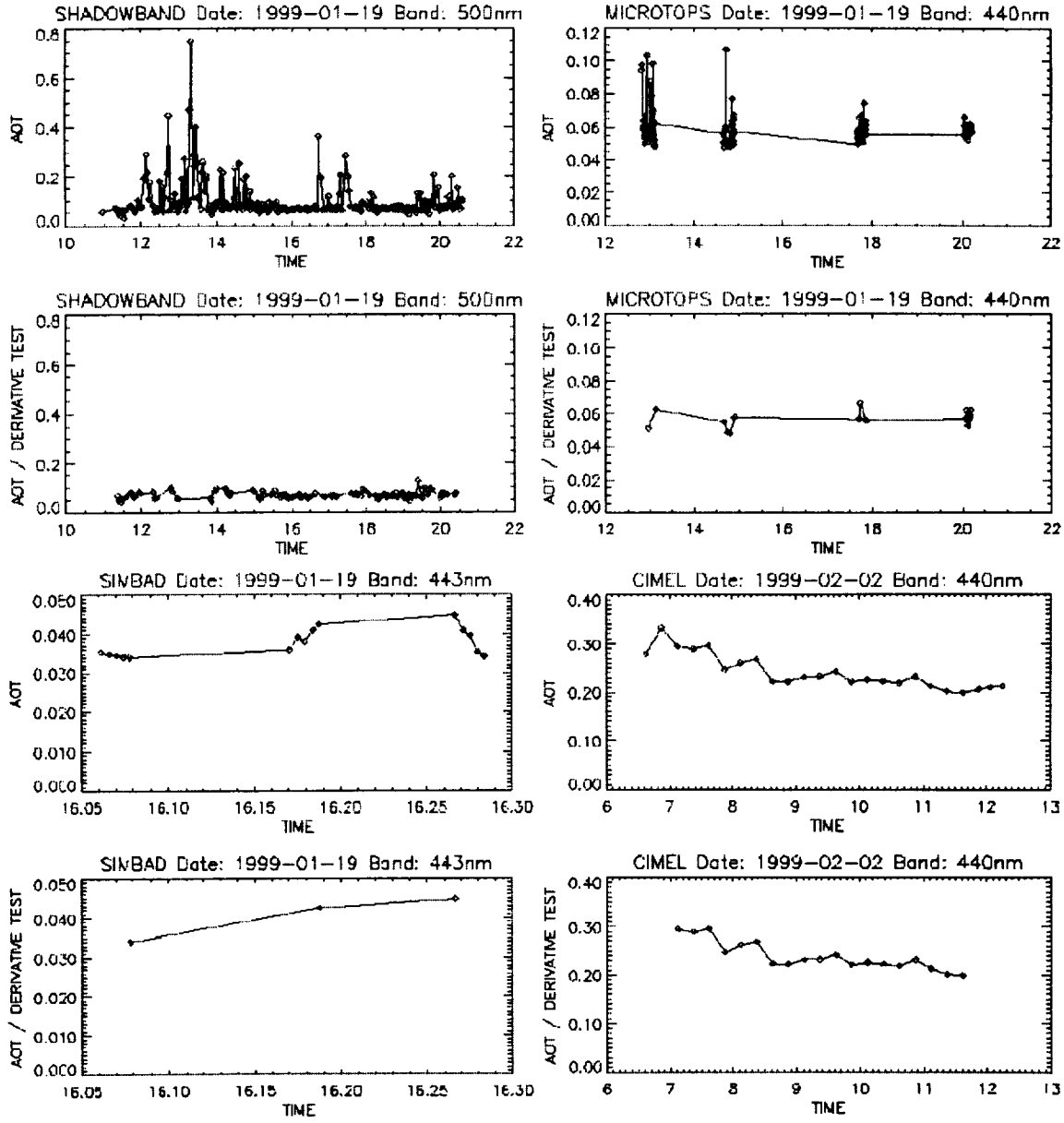

Figure 6.6 Original radiometer AOT observations and corresponding AOT measurements screened using the derivative algorithm with a common threshold value for all the instruments.

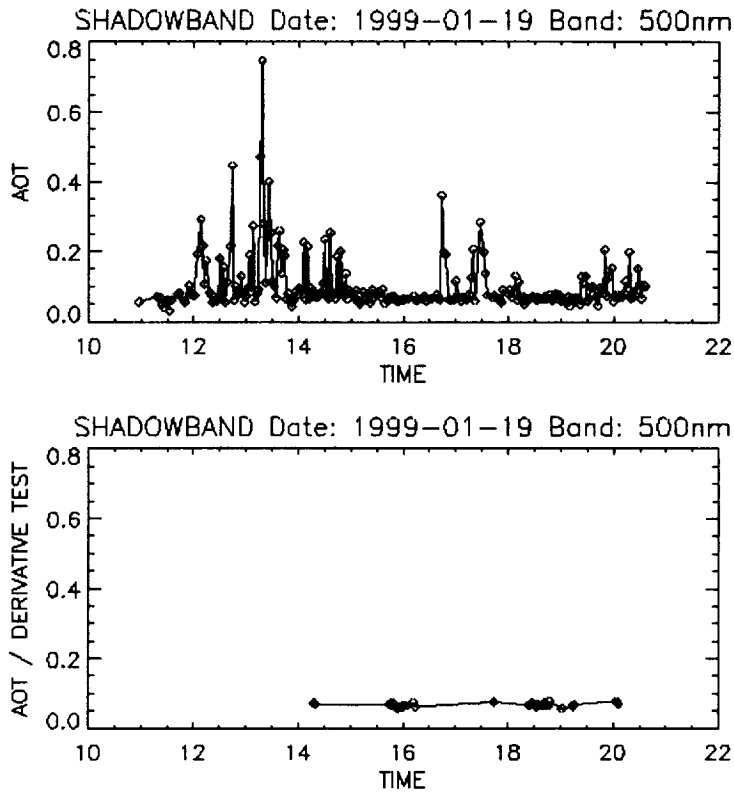

Figure 6.7 Original Shadow-band AOT observations and corresponding AOT measurements screened using the derivative algorithm within a sliding filter.

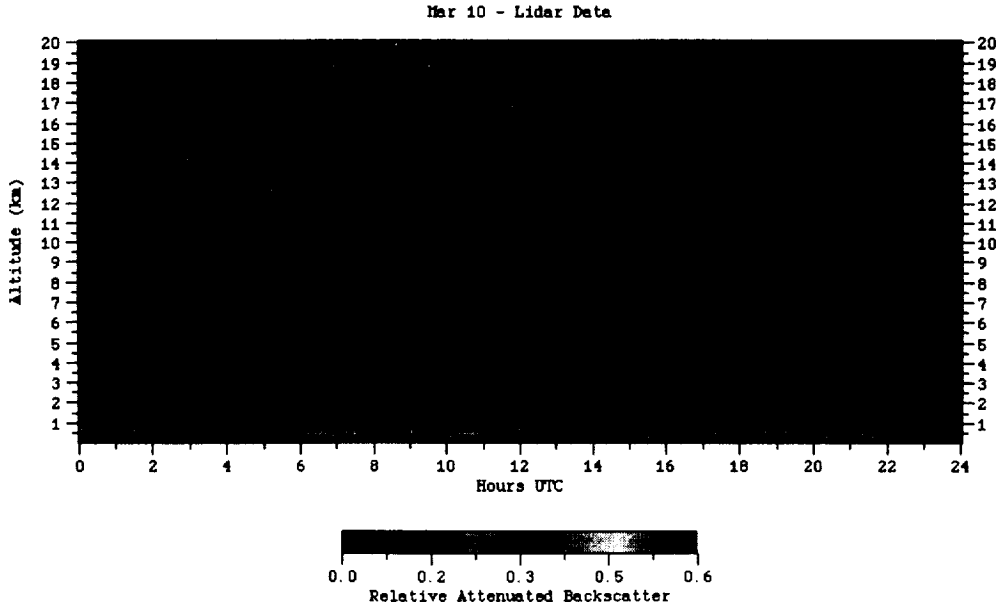

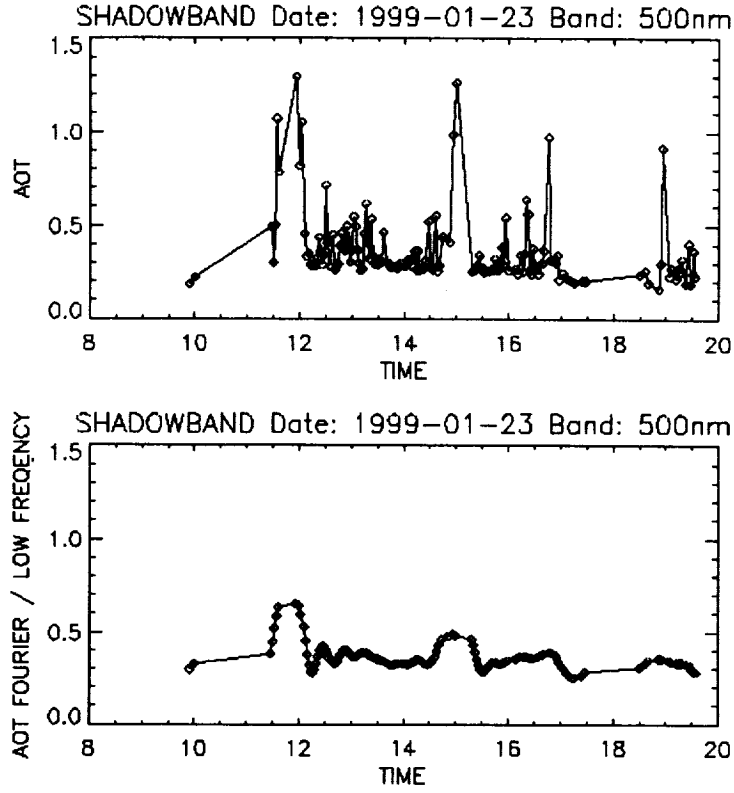

Figure 6.8 Original Shadow-band AOT observations and the corresponding result of inverse Fourier transform having 90% of high frequencies eliminated.

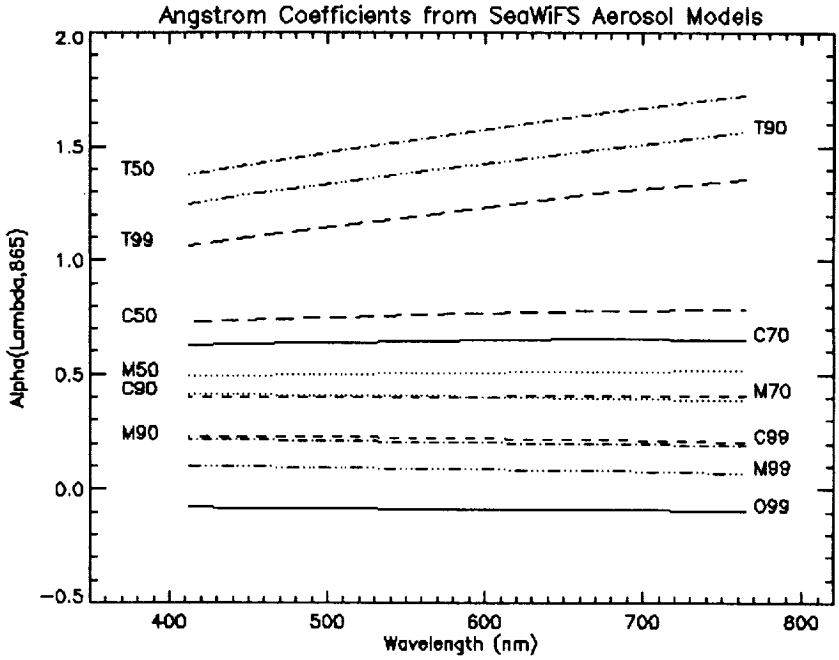

Figure 6.9. Ångström components for the 12 aerosol models used in the atmospheric correction of SeaWiFS imagery.

$$\tau \xrightarrow{DWT} (H^M\tau, GH^{M-1}\tau, \ldots, GH^2\tau, GH\tau, G\tau)$$

$M = \log_2 N$

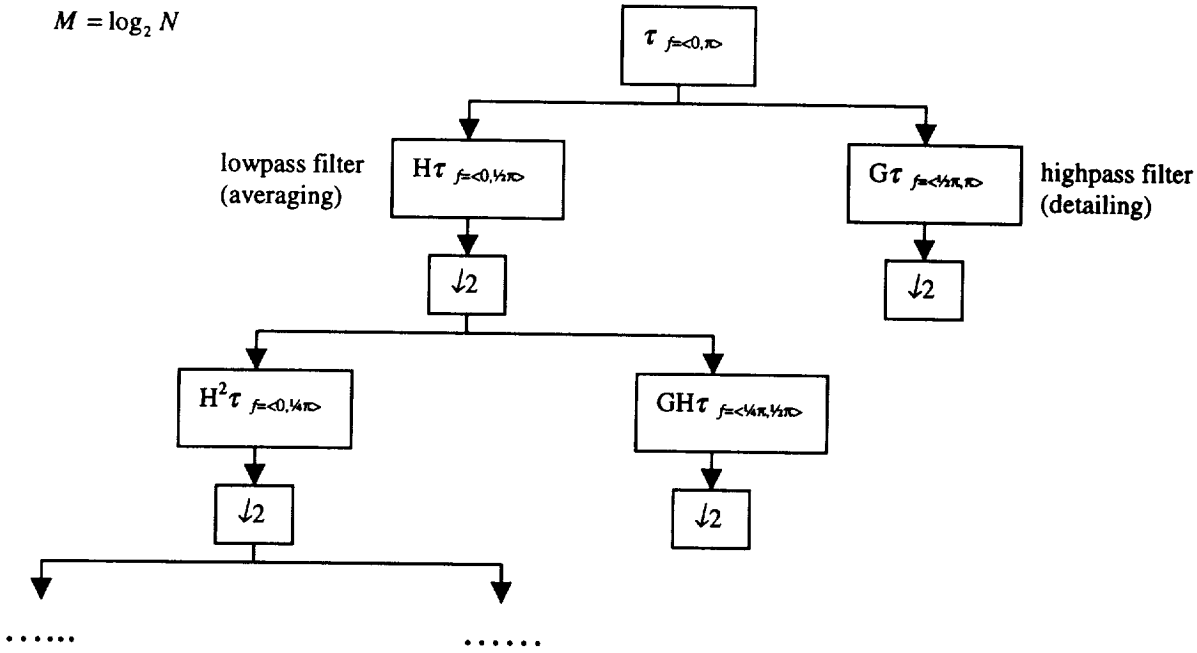

Figure 6.10. Subband coding implementation of the discrete wavelet transform.

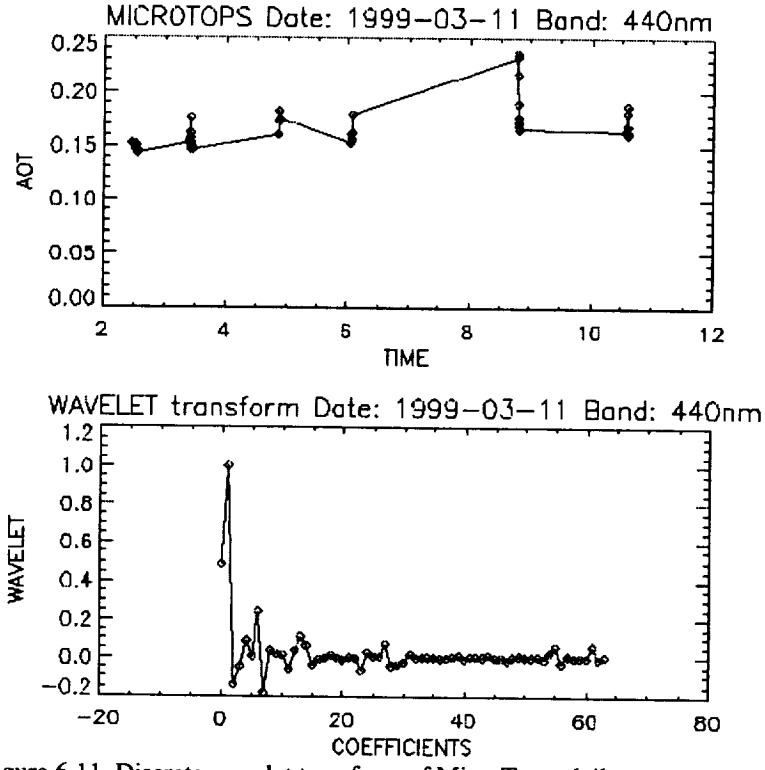

Figure 6.11. Discrete wavelet transform of MicroTops daily measurements.

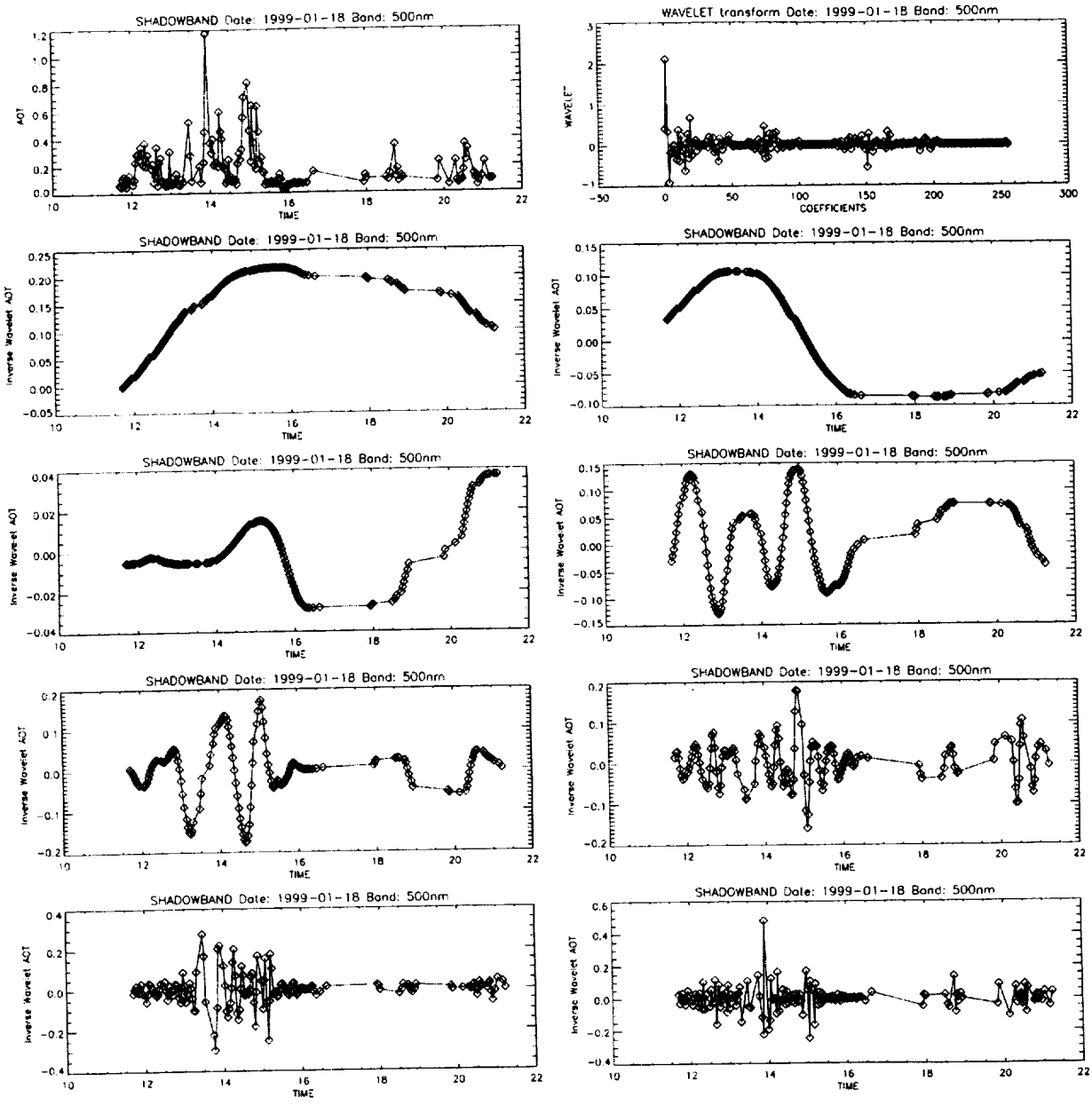

Figure 6.12. Original set of daily AOT measurements from the Shadow-band radiometer, discrete wavelet transform of the AOT signal, and inverse wavelet transforms of the signal for the consecutive frequency components from the lowest up to the highest.

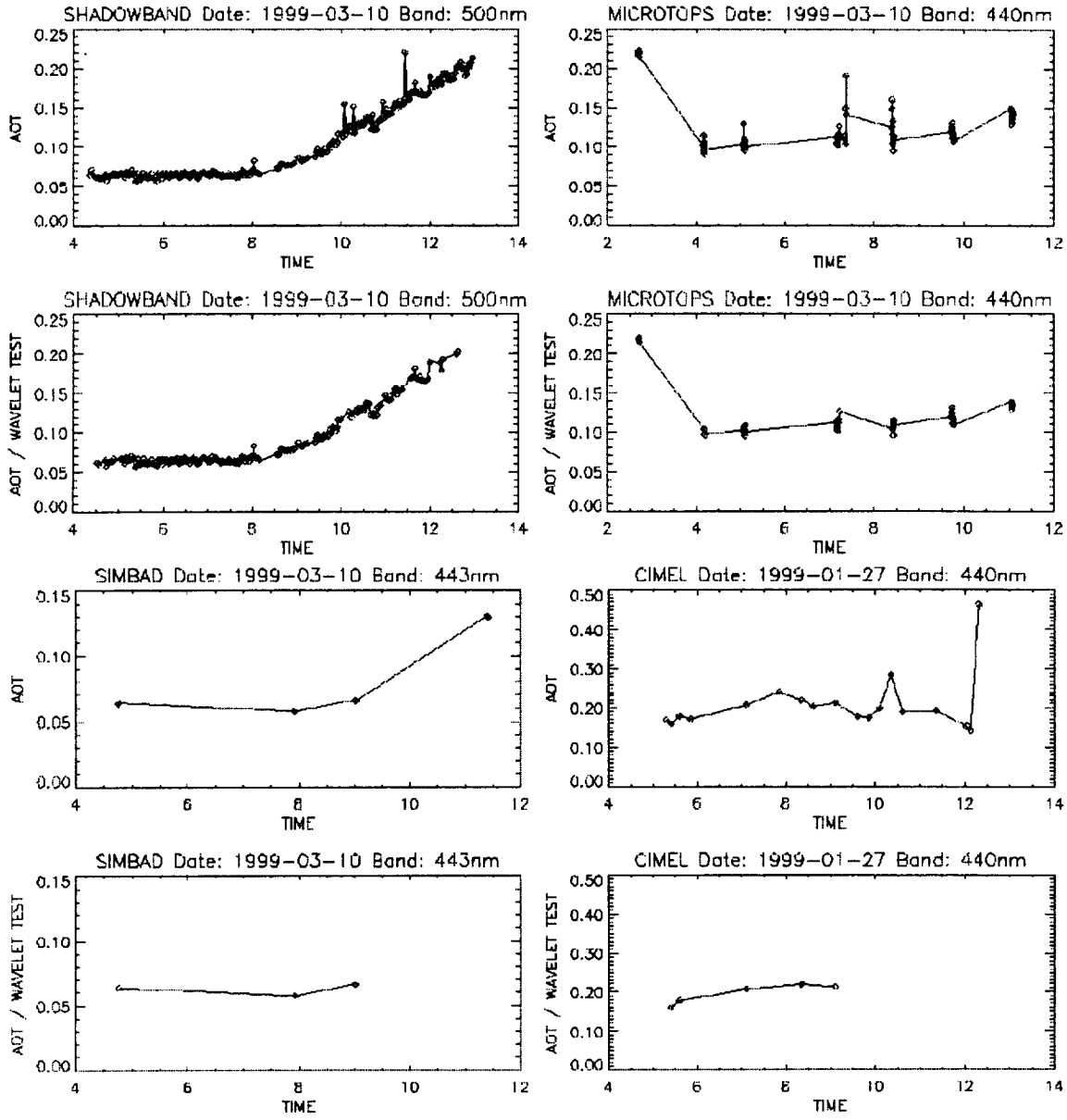

Figure 6.13. MPL backscatter, original radiometer AOT observations, and corresponding AOT measurements screened using the wavelet algorithm.

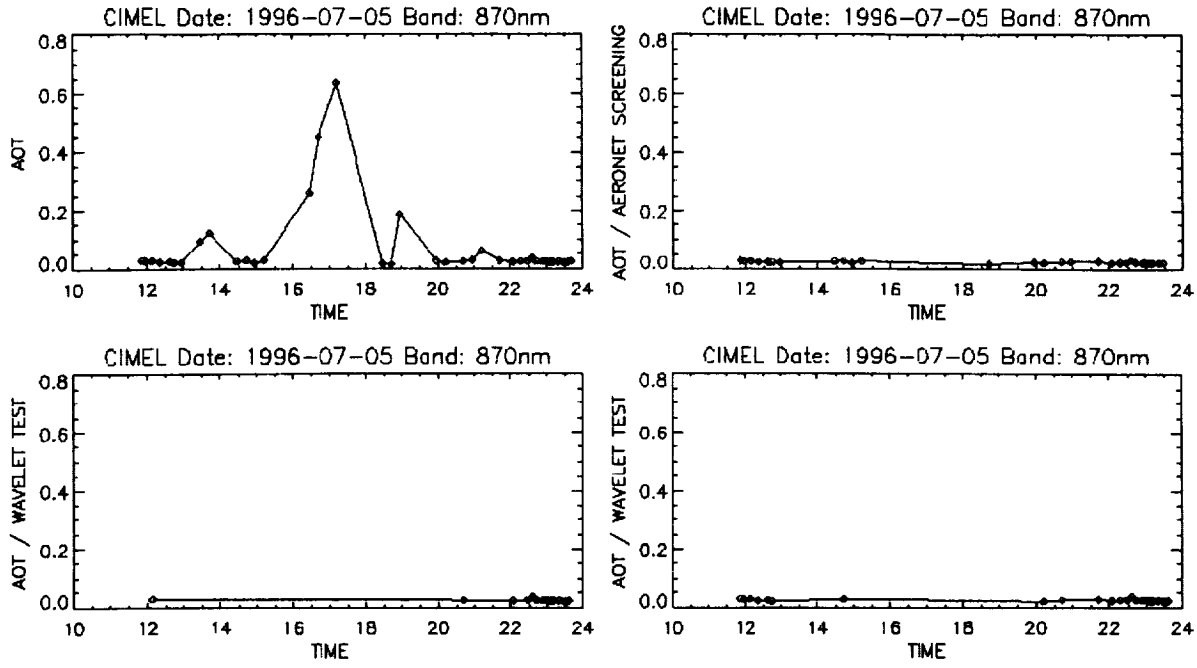

Figure 6.14. Original set of daily AOT measurements from the CIMEL radiometer at Goddard Space Flight Center and the results of the AERONET quality assurance of these observations, strict borderline-based wavelet screening, and relaxed borderline wavelet screening.

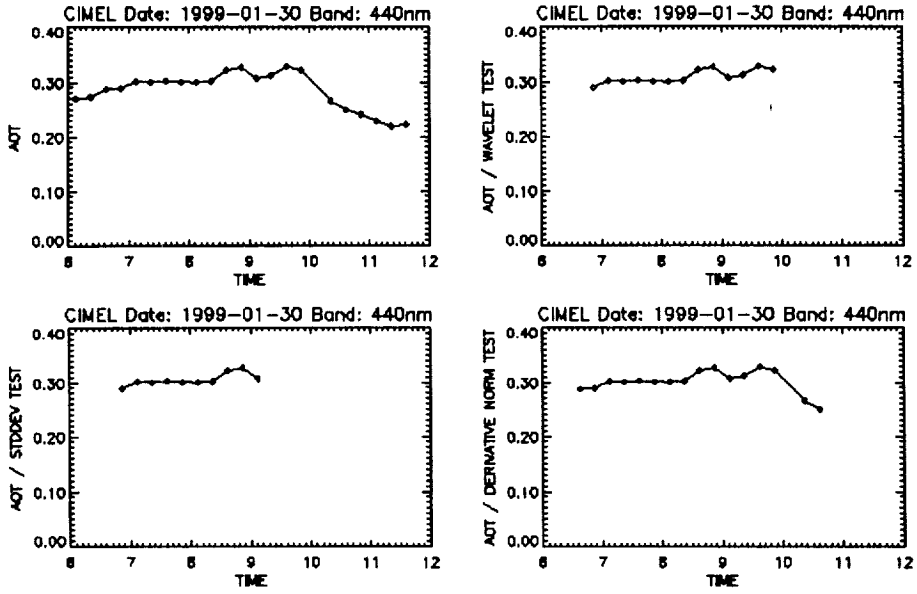

Figure 6.15. Original set of daily AOT measurements from the CIMEL radiometer at the AERONET/SIMBIOS site at Bahrain and the results of wavelet, statistical, and derivative-based screening of these observations.

REFERENCES

Ainsworth, E. J., S. W. Bailey, R. A. Barnes, R. E. Eplee, Jr., F. S. Patt, B. A. Franz, C. Hsu, C. Pietras, W. D. Robinson, M. Schmidt, M. Wang, P. J. Werdell, and C. R. McClain, 2000: Three years of experience with SeaWiFS calibration, Pacific Ocean Remote Sensing Conference (PORSEC), 5-8 December, Goa, India.

Barnes, R. A., A. W. Holmes, and W. E. Esaias, 1995: Stray light in the SeaWiFS radiometer, NASA Tech. Memo. 104566, Vol. 31, S. B. Hooker, E. R. Firestone, and J. G. Acker, Eds, NASA Goddard Space Flight Center, Greenbelt, Maryland.

Combes, J.M., Grossmann, A., Tchamitchian, Ph., 1989, Wavelets. Time-Frequency Methods and Phase Space, Springer-Verlag.

Fargion, G. S., and J. L. Mueller, Eds., 2000: Ocean optics protocols for satellite ocean color sensor validation, Revision 2, NASA Tech. Memo. 209966, NASA Goddard Space Flight Center, Greenbelt, Maryland.

Gordon, H. R., and M. Wang, 1994: Retrieval of water-leaving radiance and aerosol optical thickness over the oceans with SeaWiFS: A preliminary algorithm, Appt. Opt., 33, 443-452.

Gregg, W. W., F. S. Patt, and R. H. Woodward, 1994: The simulated SeaWiFS data set, Version 2, NASA Tech. Memo. 104566, Vol. 15, S. B. Hooker and E. R. Firestone, Eds, NASA Goddard Space Flight Center, Greenbelt, Maryland.

Masters, T., 1995, Numerical Recipes in C++, Academic Press.

Paltridge, G. W., and C. M. R. Platt, 1976: Radiative processes in meteorology and climatology, in Developments in Atmospheric Science, Elsevier, New York.

Shettle, E. P., and R. W. Fenn, 1979: Models for the aerosols of the lower atmosphere and the effects of humidity variations on their optical properties, AFGL Technical Report, AFGL-TR-79-0214, Air Force Geophysics Lab., Hanscomb AFB, Mass.

Smirnov, A., B. N. Holben, T. F. Eck, O. Dubovik, and I. Slutsker, 2000: Cloud-screening and quality control algorithms for the AERONET database, Remote Sens. Environ., 73, 337-349.

Wang, M., Bailey, S., Pietras, C., McClain, C.R. and Riley, T., 2000, SeaWiFS Aerosol Optical Thickness Matchup Analysis, in McClain, C. R., E. J. Ainsworth, R. A. Barnes, R. E. Eplee, Jr., F. S. Patt, W. D. Robinson, M. Wang, and S. W. Bailey, SeaWiFS Postlaunch Calibration and Validation analyses, Part 1, *NASA Tech. Memo.* 2000-206892, Vol. 10., S.B. Hooker and E.R. Firestone, Eds, NASA Goddard Space Flight Center, Greenbelt, Maryland, 2000.

Chapter 7

Satellite Aerosol Optical Thickness Match-Up Procedures

Sean Bailey[1] and Menghua Wang[2]
[1]*Future Tech Corporation, Greenbelt, Maryland*
[2]*University of Maryland Baltimore County*

7.1 INTRODUCTION

The validation of ocean color sensors requires the use of *in situ* (field collected) data sets. The SIMBIOS and SeaWiFS Projects have sponsored numerous principal investigators (PIs) to collect *in situ* optical and pigment data for the purpose of comparing values to those derived from OCTS, POLDER, MOS, SeaWiFS and future instruments in the SIMBIOS Porgram. The match-up design described here uses field data stored in the SeaWiFS Bio-optical Archive and Storage System (SeaBASS), match-up analysis software, and a plotting and statistics package to validate SeaWiFS derived products.

A key method for validating satellite data is to compare those values with coincident measurements taken *in situ*. NASA has sponsored field research activities to build a database of optical, pigment, and related *in situ* data for use in validating the derived products (McClain et al. 1992, 1998). These data, which are stored in the SeaWiFS Bio-optical Archive and Storage System (SeaBASS), have been made available to those assisting in the SeaWiFS algorithm development and validation effort, particularly the SIMBIOS Science Team and the Moderate Resolution Imaging Spectroradiometer (MODIS) Oceans Team. This chapter discusses the match-up procedures for the validation process.

7.2 METHODS

These procedures are in place for the SeaWiFS instrument and will be used for other missions supported by the SIMBIOS Project.

In Situ Match-Up Data Files

In situ data are compared to satellite image files by matching the two data sources in time and space. Each *in situ* data set is first summarized in a single ASCII file, known as a "match-up" file. The match-up file adheres to the SeaBASS data format described above. The data included in the match-up file are aerosol optical thickness, location, and measurement times. For all incoming data, proper descriptive documentation and, possibly, interactions with the data provider, are required to assure the usefulness of the *in situ* data for matchups (Fargion and Mueller, 2000).

Match-Up Procedure

For the SeaWiFS and SIMBIOS Projects, the match-up procedure includes using both UNIX shell scripts (CSH) and Interactive Data Language (IDL). These are used to compare individual SeaWiFS Hierarchical Data Format (HDF) files to *in situ* data records of individual measurements, i.e., stations. To generate the initial list of SeaWiFS files for consideration, the SeaWiFS Project's HDF file database is queried for files that spatially and temporally match records in the *in situ* data source. The pixel and line number of the SeaWiFS file that matches the *in situ* location is determined. A region encompassing 101 by 101 pixels centered on the matched pixel is extracted from each of the resulting initial level-1A (L1A) files (GA; LAC; and high resolution picture transmission, HRPT). These extracted data files are saved to a new file for local disk storage.

For all valid L1A matches, a level-2 (L2) product is generated from the extract file for further analysis. A comprehensive suite of SeaWiFS L2 products are generated, including all $\tau_a(\lambda)$ and ancillary data (ozone, windspeed, and atmopheric pressure). In the generation of the L2 products, the Siegel near infrared correction is applied, as well as the sun glint and out-of-band corrections. As with the extracted L1A files, the L2 files are saved to local disk storage. For each successful L2 file generated, a record including the path to the L2 file, the matched pixel and line number, and associated latitude and longitude are written to a file. This list

file and the *in situ* match-up file are used as input to the IDL program where the match-up exclusion criteria are applied and the matchup plots and statistics are generated.

Match-Up Exclusion Criteria

Only a small percentage of the candidate SeaWiFS files become final valid matches. A number of exclusion criteria have been formulated to provide an objective set of points for SeaWiFS validation that removes invalid or redundant data from consideration. The approach presented here is a result of numerous iterations. Nevertheless, future modifications to the existing set of exclusion logic is likely as a better understanding of both the SeaWiFS and *in situ* data is attained.

The first exclusion criterion applied is a time difference between the *in situ* record and the satellite overpass. A time window of ±180 min from the satellite overpass is because this window is the time period of reasonable illumination in most situations and, presumably, constant atmospheric conditions.

In the current match-up set, the majority of candidate SeaWiFS files, i.e., those that coincide with *in situ* stations, are eliminated from consideration as a result of the SeaWiFS image pixels being "flagged" (excluded) usually because of clouds and stray light, although other factors are often present. Pixels are excluded if any of the following flags are applied: atmospheric correction failure, land, sun glint, total radiance above the knee value, high satellite zenith angle, stray light, clouds or ice, and low L_{WN} (555).

If a match-up passes the temporal exclusion criterion, the valid SeaWiFS pixels are averaged for a region encompassing the matched pixel and simple statistics are recorded. The match-up approach uses a 21x21 pixel "box" for LAC resolution data and a 5x5 pixel box for GAC data. Since GAC resolution is a subsampling of LAC resolution by a factor of 4, these two boxes are nearly equivalent in areal extent.

Once the match-up code has reported all unflagged matches, the routine reviews the records for further refinement. Calculations currently used for the exclusion of points and the matchup values include:

1. 1.Minimum number of valid pixels: At least fifty percent of the non-land pixels in the box considered from the SeaWiFS image must be valid (unflagged) to avoid contaminated data.
2. SeaWiFS file reduction: If there are GAC, onboard LAC, and HRPT matches corresponding to the same *in situ* point, the order of preference is onboard LAC, HRPT, and GAC. When multiple files of the same preferred type match a single *in situ* record, the closest temporal match is selected. This selection is necessary when multiple HRPT stations or multiple GAC swaths cover the *in situ* point. Permanent real-time HRPT stations are given precedence over other HRPT sources.
3. Multiple *in situ* measurements per SeaWiFS file: Along-track measurements are included in the *in situ* match-up files where adjoining measurements are greater then 12 km apart.
4. Large coefficient of variation elimination: Satellite matchups with extreme variation between pixels in the SeaWiFS "box" (coefficient of variation, or the standard deviation divided by the mean value, > 0.2) are excluded. These typically represent frontal regions or other anomalies (e.g., cloud edges) in the SeaWiFS imagery, which make the match-up validity questionable. Presently, this test is applied to $\tau_a(865)$.

Once all the exclusion criteria are applied, statistics are generated for each comparison. These are written to an ASCII file. The final matched data set is saved as an IDL saveset" (Table 1) for future reference and analysis.

REFERENCES

Fargion, G. S., and J. L. Mueller, Ocean Optics Protocols for Satellite Ocean Color Sensor Validation, Revision 2, NASA TM 2000-20996, NASA Goddard Space Flight Center, Greenbelt, Maryland, 184 pp.

Hooker, S. B., C. R. McClain, J. K. Firestone, T. L. Westphal, E. Yeh, and Y. Ge, 1994: The SeaWiFS bio-optical archive and storage system (SeaBASS), Part 1, NASA Tech. Memo. 104566, Vol. 20, S. B. Hooker and E. R. Firestone, Eds., 27 pp.

McClain, C. R., W. E. Esaias, W. Barnes, B. Guenther, D. Endres, S. B. Hooker, B. G. Mitchell, and R. Barnes, 1992: SeaWiFS Calibration and Validation Plan, NASA Tech. Memo. 104566, Vol. 3, S. B. Hooker and E. R. Firestone, Eds., NASA Goddard Space Flight Center, Greenbelt, Maryland, 43 pp.

McClain, C. R., M. Darzi, R. A. Barnes, R. E. Eplee, J. K. Firestone, F. S. Patt, W. D. Robinson, B. D. Schieber, R. H. Woodward, and E. Yeh, 1996: SeaWiFS Calibration and Validation Quality Control Procedures, NASA Tech. Memo. 104566, Volume 38, S. Hooker and E. Firestone. Eds., NASA Goddard Space Flight Center, Greenbelt, Maryland, 64 pp.

McClain, C. R., M. L. Cleave, G. C. Feldman, W. W. Gregg, S. B. Hooker, and N. Kuring, 1998: Science quality SeaWiFS data for global biosphere research, Sea Technology, 39: 10-16.

McClain, C. R., and G. Fargion, 1999: SIMBIOS Project 1998 Annual Report, NASA Tech. Memo. 1999-208645, NASA Goddard Space Flight Center, Greenbelt, Maryland, 105 pp.

TABLE 7.1: Fields stored in match-up results summary file.

Name	Description
CRUISEID	-Cruise identifier
ENV_YEAR	-Year of *in situ* measurement
ENV_MONTH	-Month of *in situ* measurement
ENV_DAY	-Day of *in situ* measurement
ENV_HOUR	-Hour of *in situ* measurement
ENV_MINUTE	-Minute of *in situ* measurement
ENV_SECOND	-Second of *in situ* measurement
ENV_LAT	-Latitude of *in situ* measurement
ENV_LON	-Longitude of *in situ* measurement
ENV_LW(λ)	-*In situ* Lw at wavelength (λ)
ENV_ES(λ)	-*In situ* Es at wavelength (λ)
ENV_KD490	-*In situ* Kd490
ENV_CHL	-*In situ* chlorophyll concentration
TDIFF	-Time difference between *in situ* measurement and satellite overpass
SAT_FILE	-Satellite extract filename
SAT_COUNTS	-Number of valid pixels in 3x3 box surrounding *in situ* lat/lon
SAT_SOLZ	-Solar zenith angle at satellite overpass
SAT_SOLA	-Solar azimuth angle at satellite overpass
SAT_SENZ	-Satellite zenith angle at satellite overpass
SAT_SENA	-Satellite azimuth angle at satellite overpass
SAT_LW_(λ)	-Satellite Lw at wavelength (λ)
SAT_ES_(λ)	-Satellite Es at wavelength (λ)
SAT_NLW_(λ)	-Satellite Lwn at wavelength (λ)
SAT_TAUA_(λ)	-Satellite aerosol optical thickness at wavelength (λ)
SAT_ANGSTROM_555	-Satellite angstrom exponent between 865-555 nm
SAT_EPSILON	-Satellite epsilon value
SAT_OZONE	-Ancillary Ozone value
SAT_WINDSPEED	-Ancillary windspeed
SAT_PRESSURE	-Ancillary atmospheric pressure
SAT_CHL_OC2	-Satellite-derived chlorophyll using OC2v2 (operational algoithm at the time of this writing)
SAT_K_490	-Satellite derived Kd490
SAT_(λ)_STATS	-Simple statistics on satellite measurements (min, max, stdev)
ENV_ES(λ)_CALC	-Calculated *in situ* Es using Gordon clear sky model

Chapter 8

Analyses of Match-Up Results

Ewa J. Ainsworth[1], Christophe Pietras[1] and Sean Bailey[2]
[1]*SAIC General Sciences Corporation, Beltsville, Maryland*
[2]*Future Tech Corporation, Greenbelt, Maryland*

8.1 INTRODUCTION

Match-ups between AOT points obtained from *in situ* observations and satellite-derived AOT levels are analyzed to:

- validate *in situ* AOT screening strategies;
- verify calibration of satellite sensor near-infrared bands; and
- establish the effectiveness of the applied suit of aerosol models.

The results of the match-ups are assessed using statistical estimates. However, the conclusive result appraisal is more flexible because of the uncertainties involved in comparing the two types of data and because of the uncertainties inherent in the measurements themselves. The uncertainties in comparing satellite- and *in situ*-derived AOT information were described in detail in Chapter 6. The accuracy of different *in situ* AOT screening strategies can only be determined approximately from the match-ups because both compared AOT measures are not absolute and are under scrutiny. A general statistical trend in the satellite band calibration is evaluated. Finally, the aerosol model suitability is estimated from the comparison of spectral distributions of AOT levels for satellite-derived and *in situ* measurements.

Match-ups presented in this chapter have been obtained for the SeaWiFS-derived aerosol properties and AOT levels calculated from AERONET and SIMBIOS sun and sky radiometer data. The match-up results are not conclusive. Research into vicarious calibration of the SeaWiFS instrument using *in situ* AOT observations and validation of the atmospheric correction algorithm is continuing.

The purpose of this chapter is to use the preliminary results to describe a variety of match-up analysis techniques which have been developed and implemented during the current study and show some graphical examples of these techniques. These analyses can be performed on any matched satellite and *in situ* AOT data points. They can thus apply to different ocean color sensors and sun and sky radiometers. The match-up analysis algorithms have been implemented in IDL.

8.2 ACCURACY OF THE MATCH-UPS

The figures displayed in this chapter give match-up results and additional information on the match-up statistics. There are four sets of information included:

- maximum error in matching satellite and *in situ*-obtained AOT points (MaxDiff);
- percentage of match-up points over the y = x line (Up);
- slope of the linear fit between two sets of AOT points which is approximated using χ^2 error statistics (Slope); and
- inaccuracy of AOT match-ups (Error).

Estimation of inaccuracies in match-ups between satellite-derived AOT values and *in situ* measurements is difficult. The inaccuracy assessment needs to take into consideration the intrinsic uncertainty of the instrument, the satellite and the sun or sky radiometer; varying magnitudes in AOT values; and the statistical validity of the AOT match-up set.

The uncertainties associated with AOT measurements are different for different instruments. The uncertainty of CIMEL sun photometer measurements is estimated at ±0.015 for AOT values (Chapter 3). Current calculations roughly assume that the acceptable measurement error for both satellite and sun/sky radiometer AOT levels is ±0.02. Therefore, the total error in comparisons can be up to ±0.04 in AOT fraction. Consequently, if AOT match-up points for the satellite and *in situ* instruments differ by 0.04 or less, the points are considered identical. Also, a 0.04 constant is subtracted from differences

between AOT observations which are larger than 0.04.

For low AOT values, small magnitude errors create a large percentage of the actual AOT measure. The AOT magnitude problem has not been eliminated from the current results despite the AOT normalization. Consequently, current descriptions of error statistics depend on magnitudes of AOT values within the match-up set. Because the spectral distribution of non-absorbing AOT values monotonically decreases from short wavelength visible bands towards near-infrared bands, near-infrared bands have lower AOT values than visible bands. Consequently, the error statistics for different bands is not fully uniform and reliable. This especially occurs when there are low AOT values in band 870nm. Finally, the larger the sets of AOT match-ups, the more reliable the statistics.

8.3 VALIDATION OF *IN SITU* AOT SCREENING STRATEGIES

Chapter 7 reviewed *in situ* AOT processing algorithms which included temporal screening methods designed to eliminate cloudy and erroneous measurements. In Figure 8.1, match-up results are compared for two of the screening strategies. The figure shows SeaWiFS-derived AOT levels matched against *in situ* AOT points which have been screened using the statistical and wavelet-based approaches. The comparison is made for AOT measurements captured at the Bahrain AERONET/SIMBIOS site by a CIMEL sun photometer. The screening methods applied only a single spectral band, the 870nm band. The comparison is made for the SeaWiFS bands which are the closest to the CIMEL bands.

The comparison in Figure 8.1 illustrates that both statistical and wavelet approaches to screening cloud-contaminated and erroneous measurements obtain roughly equivalent comparison results for AOT measurements derived from the CIMEL sun photometer. The wavelet method rejected some observations characterized by high levels of AOT which were accepted by the statistical approach.

Aerosol observations obtained from the CIMEL instrument are uniformly spread throughout a day and occur within proportional time intervals. Usually, there are just above 12 measurements captured within ± 3 hours surrounding the satellite over-flight. For daily *in situ* AOT observations evenly distributed in time, all three screening strategies (statistical and derivative-based estimates of daily AOT variations as well as the wavelet algorithm) recommended in Chapter 6 Section 6.4 appear to give comparable match-up results. However, all three approaches are not universal for different automatic and hand-held sun and sky radiometers and a variety of *in situ* AOT data sets obtained by different investigators. The wavelet screening is the only algorithm applicable across all the instruments and *in situ* data sets.

The accuracy of the screening strategies for cloudy and erroneous observation removal cannot be firmly verified from the match-up results. This is because the comparisons are performed against SeaWiFS-obtained AOT levels and ocean color algorithms which are themselves being investigated. There are no reliable validation data for the match-ups. The accuracy of the screening strategies can be directly verified in two ways:

- By comparisons against Micropulse Lidar (MPL) backscatter data described in Chapter 6. MPL backscatter information has not been available for the AERONET/SIMBIOS CIMEL sun photometers.
- By comparisons of screened *in situ* AOT measurements obtained simultaneously from different instruments. These comparisons will be described later in the current chapter.

The accuracy of AOT match-ups has also been analyzed in terms of the number of sun and sky radiometer spectral bands used in the screening of cloud-contaminated and erroneous measurements. The issues concerned with the choice of spectral bands used in the AOT screening are described in section 6.6 of this document. The match-ups with SeaWiFS for *in situ* CIMEL AOT observations screened using the wavelet approach are displayed in Figure 8.2. The top set of two graphs gives the result for the screening version which used only the 870nm band. The bottom set of two graphs displays the consequences of applying multiple spectral bands in the screening. In the second case, at least two bands are used to eliminate cloudy and erroneous AOT measurements from CIMEL observations.

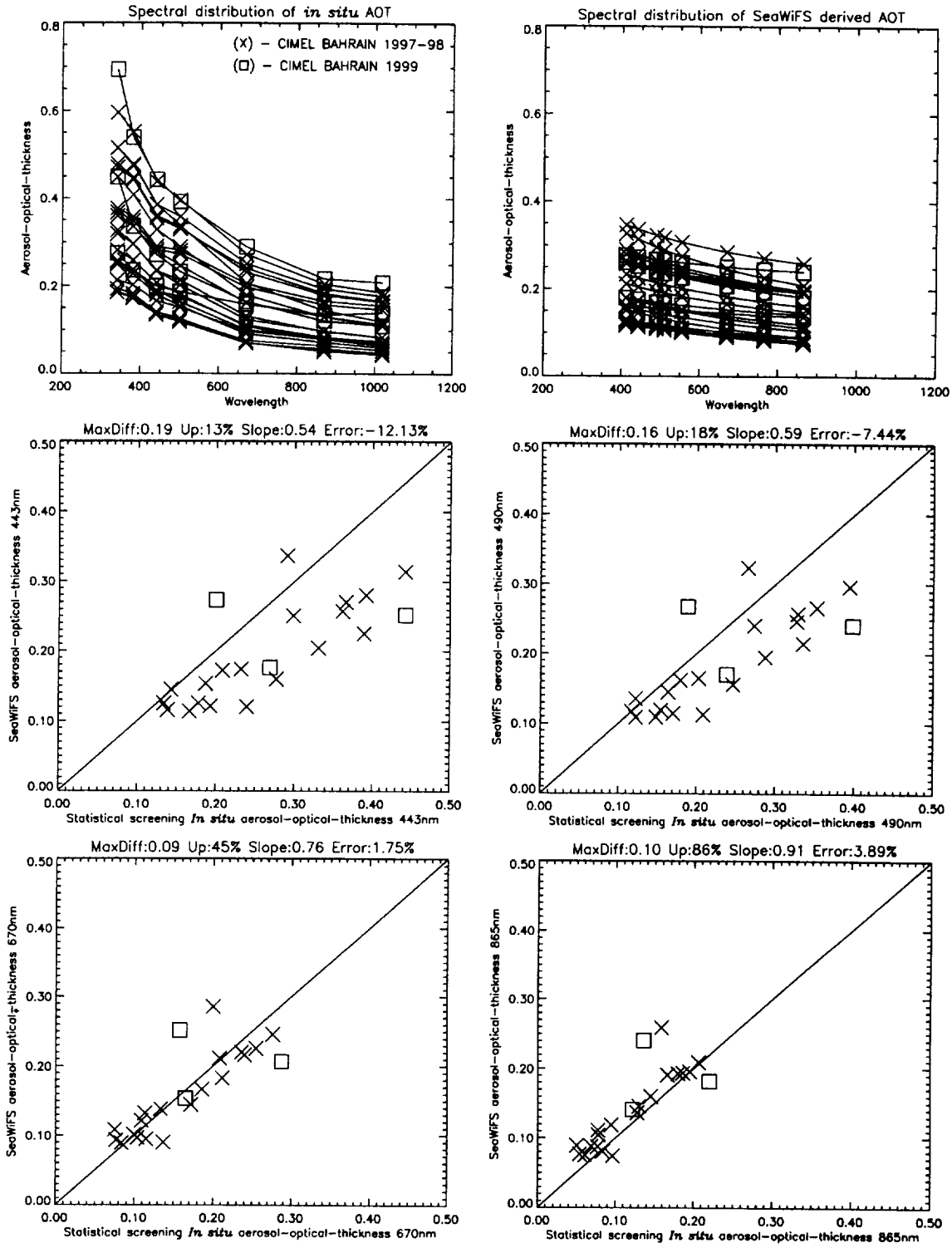

Figure 8.1a Match-up results between SeaWiFS-obtained AOT values and AOT measurements captured in Bahrain by a CIMEL sun photometer. The *in situ* CIMEL observations were screened using the statistical based approach and a single spectral band centered at 870nm.

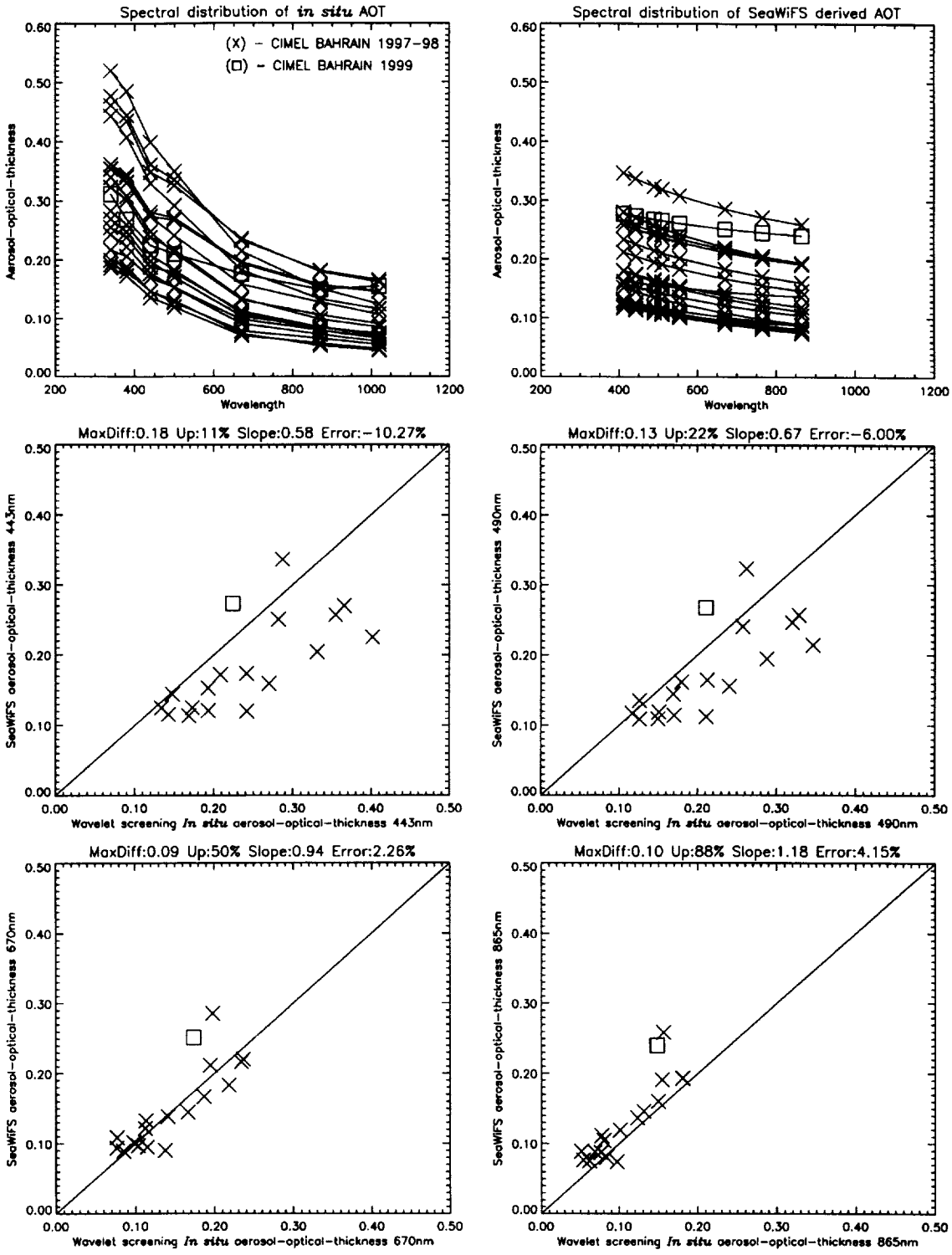

Figure 8.2b Match-up results between SeaWiFS-obtained AOT values and AOT measurements captured in Bahrain by a CIMEL sun photometer. The *in situ* CIMEL observations were screened using the wavelet based approach and a single spectral band centered at 870nm.

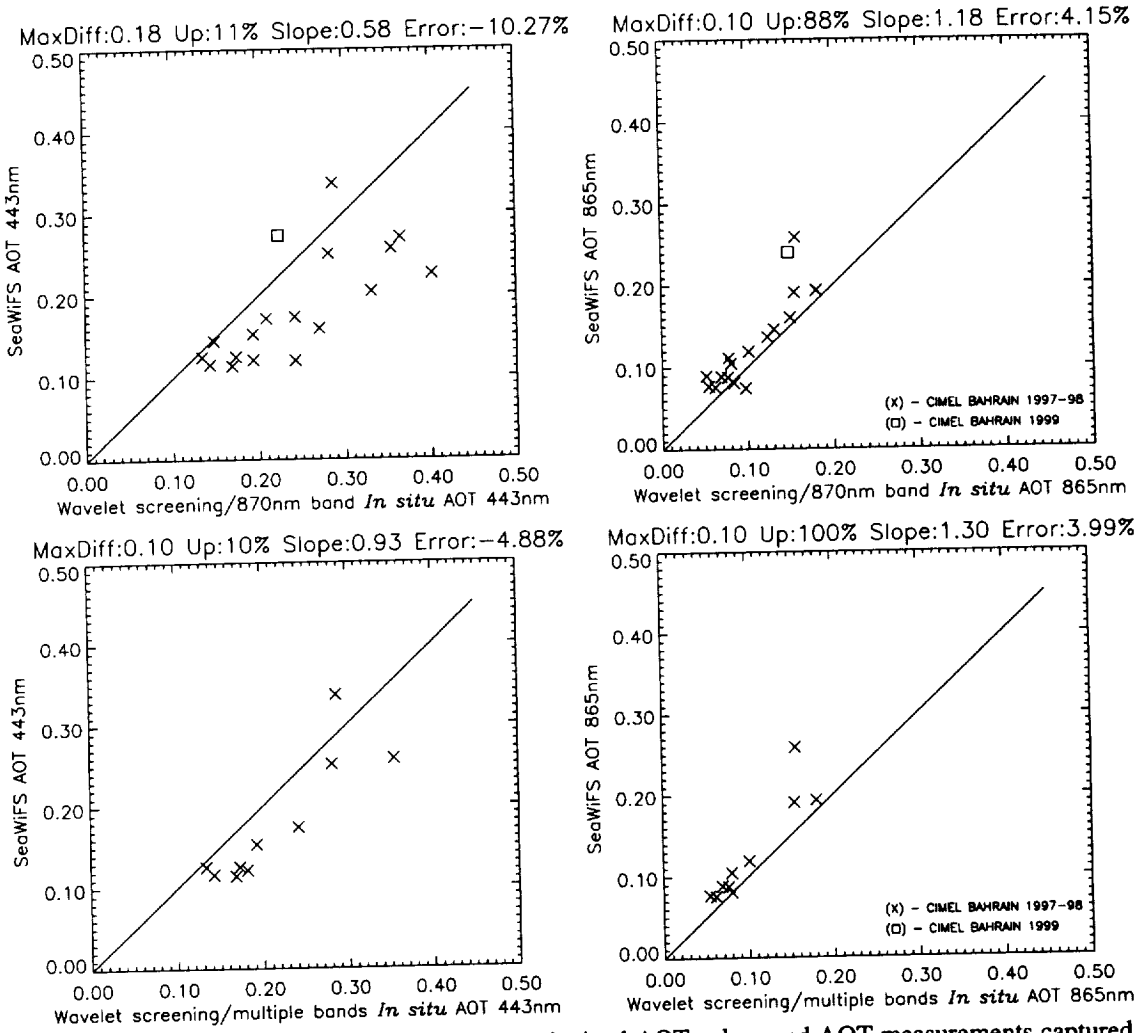

Figure 8.2. Match-up results between SeaWiFS-obtained AOT values and AOT measurements captured in Bahrain by a CIMEL sun photometer. The measurements were screened by the wavelet-based algorithm using a single 870nm spectral band (top two graphs) and the multi-band approach (bottom two graphs).

Figure 8.2 shows that multi-band screening eliminates many *in situ* AOT points from the match-up set because they do not pass the multi-band criteria for cloud-free and valid observations. The comparison in the 865nm band suggests that many valuable *in situ* AOT points may have been removed. However, the results in the 443nm band illustrate that most of those *in situ* AOT points are rejected which do not extrapolate well towards the visible spectra using the applied set of aerosol models. It therefore indicates that some properties of cloudy and erroneous aerosol measurements are better differentiated using the visible range of the spectrum. Near-infrared AOT measurements alone may be insufficient to temporally screen sun and sky radiometer data and the combination of near-infrared and visible bands may be ideal. Because AOT spectral distributions usually decrease monotonically from the visible towards the near-infrared spectrum, larger AOT magnitudes in the visible range can also help to detect subtleties in AOT temporal variations.

More research is needed into the spectral expression of features associated with cloud-contaminated and erroneous AOT measurements. This initial study indicates that the application of multi-band AOT temporal screening can remove *in situ* AOT observations which are suspected of being cloudy or invalid. AOT measurements screened using the multi-band method can then produce more reliable results in comparisons with satellite-obtained AOT values. These improved match-up results can be obtained without upgrading the applied set of aerosol models.

8.4 MATCH-UP RESULTS

Figure 8.3 illustrates the results of comparisons between SeaWiFS-obtained AOT values and *in situ* AOT points derived from CIMEL measurements. Four CIMEL sites are included in the match-ups. Because of the difficulties in accessing a database of level 1 SeaWiFS imagery, the match-ups are only shown for CIMEL observations which are screened using the statistical algorithm (without the sliding filter utility described in Chapter 6) and the single 870nm spectral band. *In situ* AOT results are converted into SeaWiFS spectral bands and only those bands are displayed which are the closest to the original CIMEL bands.

Figure 8.3 shows that the AOT match-ups compare relatively well for SeaWiFS and *in situ* points in the near-infrared 865nm band. There is, however, a systematic overestimation by SeaWiFS in 865nm band match-ups of around 0.023 in the AOT value. SeaWiFS overestimates AOT measures relative to CIMEL observations in 85% of near-infrared cases. The 8.4% error in the near-infrared band match-ups is elevated due to outliers and low AOT levels which cause the error to be high compared to the magnitude of the AOT values themselves. The slope of the linear fit between the pairs of SeaWiFS and *in situ* measurements closely approaches 1 for the 865nm band match-ups. As the wavelength decreases towards the visible spectrum, the lower the slope value for the match-ups and the more the SeaWiFS algorithm underestimates AOT measures relative to CIMEL observations. For the visible 443nm band, the SeaWiFS processing underestimates 77% of AOT match-up points and the significant spread of the points results in a low slope of 0.61 for the linear fit between the satellite and *in situ* data sets.

Starting from relatively accurate AOT match-ups in the high wavelength near-infrared bands, the discrepancy in the match-ups increases with decreasing wavelengths. Figure 8.4 presents spectral distributions of daily AOT CIMEL measurements obtained at the AERONET/SIMBIOS sites in Bahrain and San Nicolas. The figure also shows these days' distributions of *in situ* and corresponding SeaWiFS-derived AOT match-up points. The AOT spectral distribution shown for Bahrain represents the most common case in which SeaWiFS slightly overestimates the AOT compared to CIMEL measurements in the 865nm band and significantly underestimates the AOT in lower wavelength visible bands. The San Nicolas example shows SeaWiFS overestimation of AOT levels in most of the spectral bands when compared to the sun photometer observations. In general, SeaWiFS AOT spectral distributions appear to be defined by much flatter curves than *in situ* AOT measures. This strongly contributes to the inaccuracies in AOT match-ups.

8.5 ANALYSES OF SENSOR NEAR-INFRARED BANDS

Aerosol model selection accuracy and AOT value estimation performed by the atmospheric correction algorithm depend on the relative and absolute calibrations of the near-infrared bands. For the SeaWiFS algorithm, aerosol models are established through ratios of single scattering aerosol reflectance in the 765nm and 865nm bands (Eplee et al., 2000). The relationship between near-infrared band calibrations has been here investigated in more detail.

For the AOT match-up points from Figure 8.3, an Ångström coefficient has been calculated for the 765nm band. The coefficient is obtained relative to the 865nm band following Equation 6.3 which was defined in Chapter 6. CIMEL AOT values are interpolated to the SeaWiFS bands using a linear fit in the logarithmic space within the entire CIMEL ocean color spectral range. The Ångström match-ups are displayed in Figure 8.5. The figure shows that Ångström levels are significantly underestimated in the 765nm band by the SeaWiFS algorithm when compared to *in situ* data. Only 12% of the Ångström coefficients for SeaWiFS-defined AOT values are higher than the Ångström components obtained from *in situ* observations. The spread of Ångström levels for CIMEL measurements is larger, (0.0, 2.0), than for SeaWiFS-derived AOT values, (0.0, 1.0). Consequently, the linear fit between the two sets of Ångström match-up points has a significantly flattened slope and a bias. The Ångström match-ups indicate inaccuracies in the calibration of the SeaWiFS near-infrared bands.

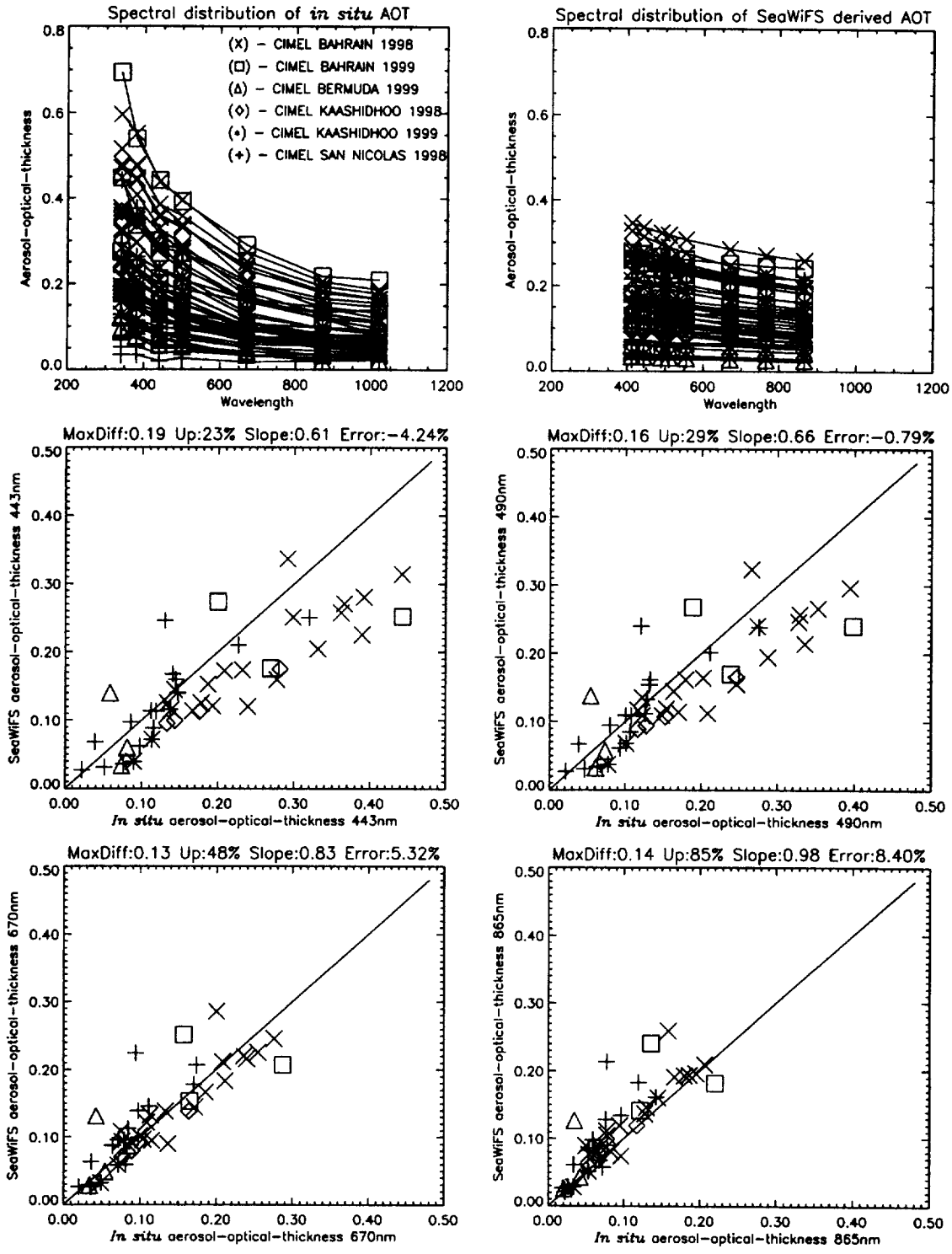

Figure 8.3. Match-up results between SeaWiFS-obtained AOT values and AOT measurements captured by different CIMEL sun photometers. The CIMEL observations were screened by the statistical algorithm using a single spectral band centered at 870nm.

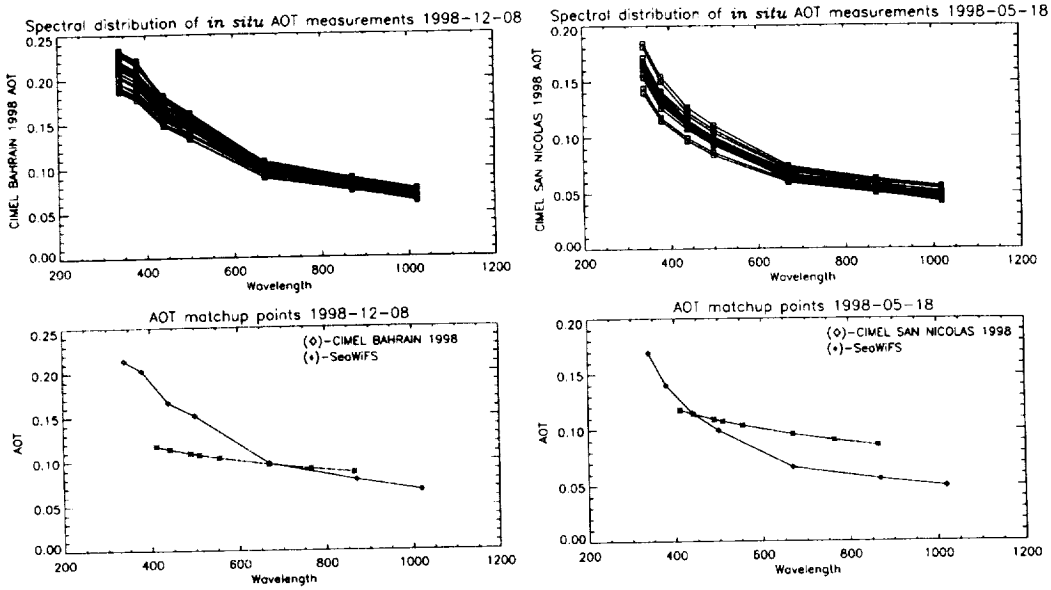

Figure 8.4. Spectral distribution of *in situ* AOT daily measurements (top graphs) and distributions of corresponding *in situ* and SeaWiFS-derived AOT match-up points.

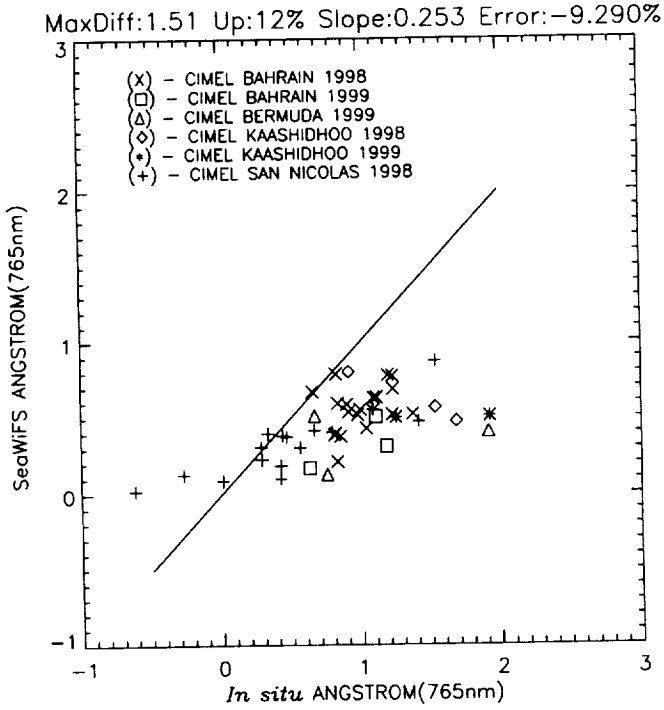

Figure 8.5. Ångström coefficient match-ups for SeaWiFS-obtained and *in situ* AOT values captured by different CIMEL sun photometers and screened using the statistical algorithm and a single spectral band centered at 870nm.

The Ångström match-ups show that there are some AOT SeaWiFS and *in situ* points which are very close for both types of observations. These AOT points have been extracted from the match-up set. They are employed to evaluate the accuracy of the extrapolation of the aerosol path radiance towards the visible spectra using existing aerosol models. The actual condition for the selection of AOT match-up points is that their Ångström coefficient in the 765nm band should not differ by more than 0.2 in the Ångström value for SeaWiFS- and *in situ*-derived AOT levels. Match-ups in six SeaWiFS visible bands for these particular AOT points are presented in Figure 8.6. Although there is a small number of similar Ångström AOT match-up points, the figure illustrates that for these AOT points the match-up accuracy is high, even in the low wavelength visible bands.

Figure 8.6 clarifies that, even for close Ångström AOT match-up points, the underestimation by the SeaWiFS algorithm of AOT levels in the low wavelength visible spectra is still observable. In the blue bands, only two AOT match-ups from a single CIMEL site at San Nicolas are higher for SeaWiFS than for *in situ* data. These two match-up points do not provide a statistically reliable alternative to the remaining match-ups. It can be speculated that flat spectral distributions of the existing aerosol models prohibit precise extrapolation of the aerosol path radiance to the visible spectra.

8.6 CROSS-INSTRUMENT VALIDATION OF *IN SITU* AOT POINTS.

As the AOT match-ups are associated with large degrees of uncertainty (major match-up uncertainty issues are discussed in Chapter 6), a validation of *in situ* AOT points against measurements obtained from two or more radiometers can give a more reliable basis for the comparisons. During cruise experiments there may be a number of sun photometers and sky radiometers performing simultaneous AOT observations. Concurrent AOT points obtained by screening AOT observations for the match-ups can be validated against one another. If these *in situ* AOT points agree approximately, the results of the match-ups with satellite-derived AOT levels can provide a more confident basis for satellite sensor calibration and algorithm validation.

Figure 8.7 displays four screened *in situ* AOT points which are obtained from MICROTOPS II and SIMBAD sun photometer measurements. The measurements were performed during AEROSOLS'99 and INDOEX cruises on four different days. The maximum difference between the AOT observation time by both instruments was thirty minutes. The maximum spatial difference between the geographical locations where both sets of AOT measurements were obtained was 15km. The MICROTOPS II and SIMBAD observations which went into these AOT points were screened with the wavelet-based algorithm to remove cloud-contaminated and erroneous measurements. The multi-band version of the screening was applied.

It can be seen that the AOT distributions for *in situ* points coming from both sun photometers agree relatively closely for all ocean color bands common between the instruments. Therefore, these points create a solid basis for match-ups with satellite-derived AOT measures. Due to the current problems with accessing the database of SeaWiFS level 1 imagery, only two of the cross-instrument validated *in situ* AOT points were matched with satellite-derived AOT estimates. The match-up results for the two points are illustrated in Figure 8.8. These results are not suitable to draw statistically viable conclusions about the accuracy of the satellite sensor calibration and the atmospheric correction algorithm. However, the match-ups demonstrate the soundness of the cross-instrument validation method for *in situ* AOT points. They demonstrate with high certainty that the existing satellite calibration and atmospheric correction can provide exceptionally accurate estimates of AOT values in all ocean color bands in certain favorable conditions. In this case, *in situ* AOT points have relatively flat spectral distributions which are easily approximated by the SeaWiFS aerosol models.

The screening algorithm applied to produce the *in situ* AOT points, the multi-band version of the wavelet technique, contributed to this flawless result. The multi-band wavelet screening proved to be very strict in eliminating cloudy and erroneous AOT measurements and left few points for match-ups with satellite-derived AOT values. It also showed the most reliable and comprehensive. The wavelet algorithm was successfully validated for different sun and sky radiometer data against MPL backscatter information (Chapter 6) and provided more accurate match-up results with SeaWiFS.

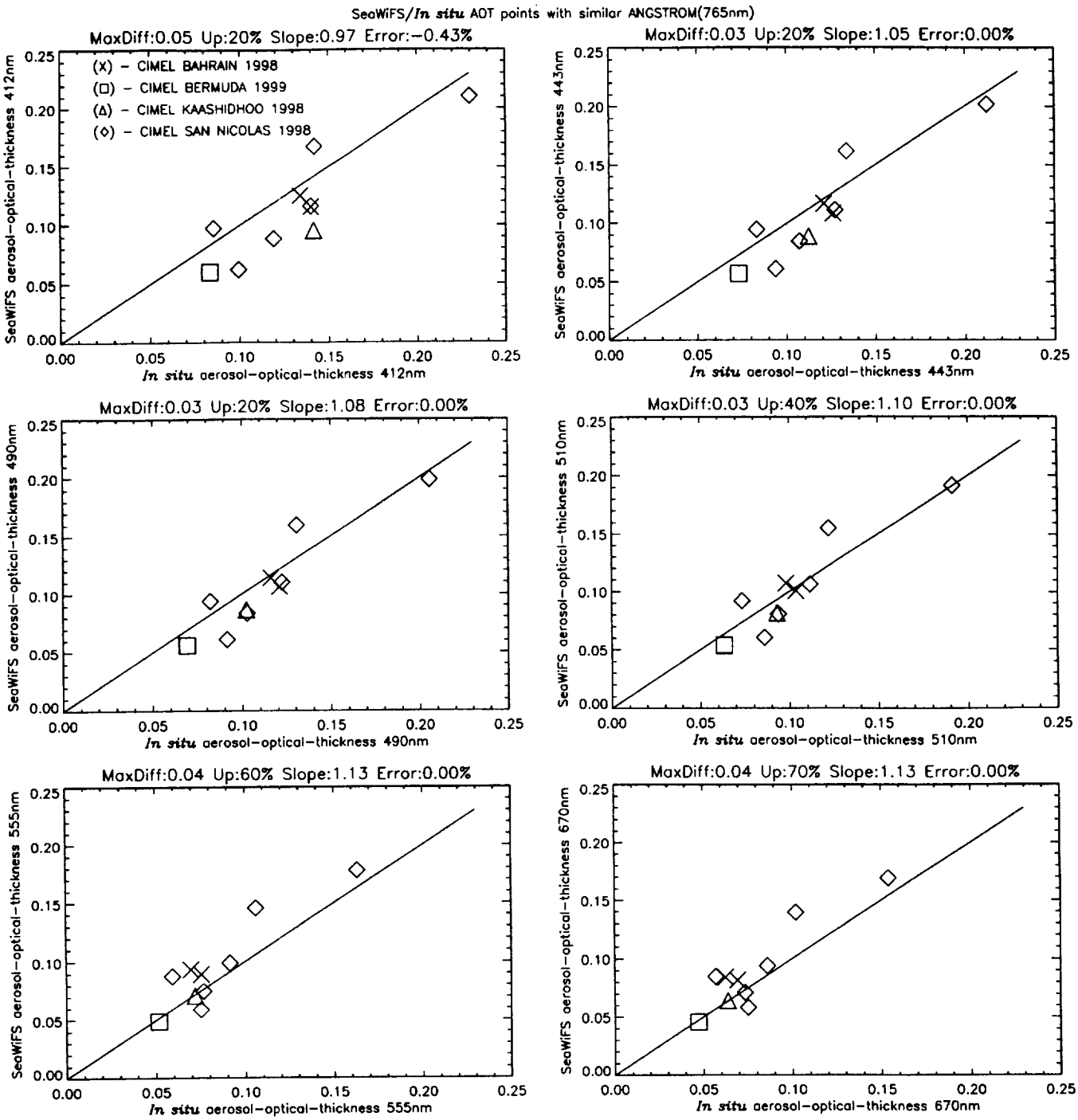

Figure 8.6. Match-up results for AOT points characterized by a similar value of the Ångström coefficient at 765nm for SeaWiFS-obtained and *in situ* measurements. The *in situ* AOT observations were captured by different CIMEL sun photometers and screened using the statistical algorithm and a single spectral band centered at 870nm.

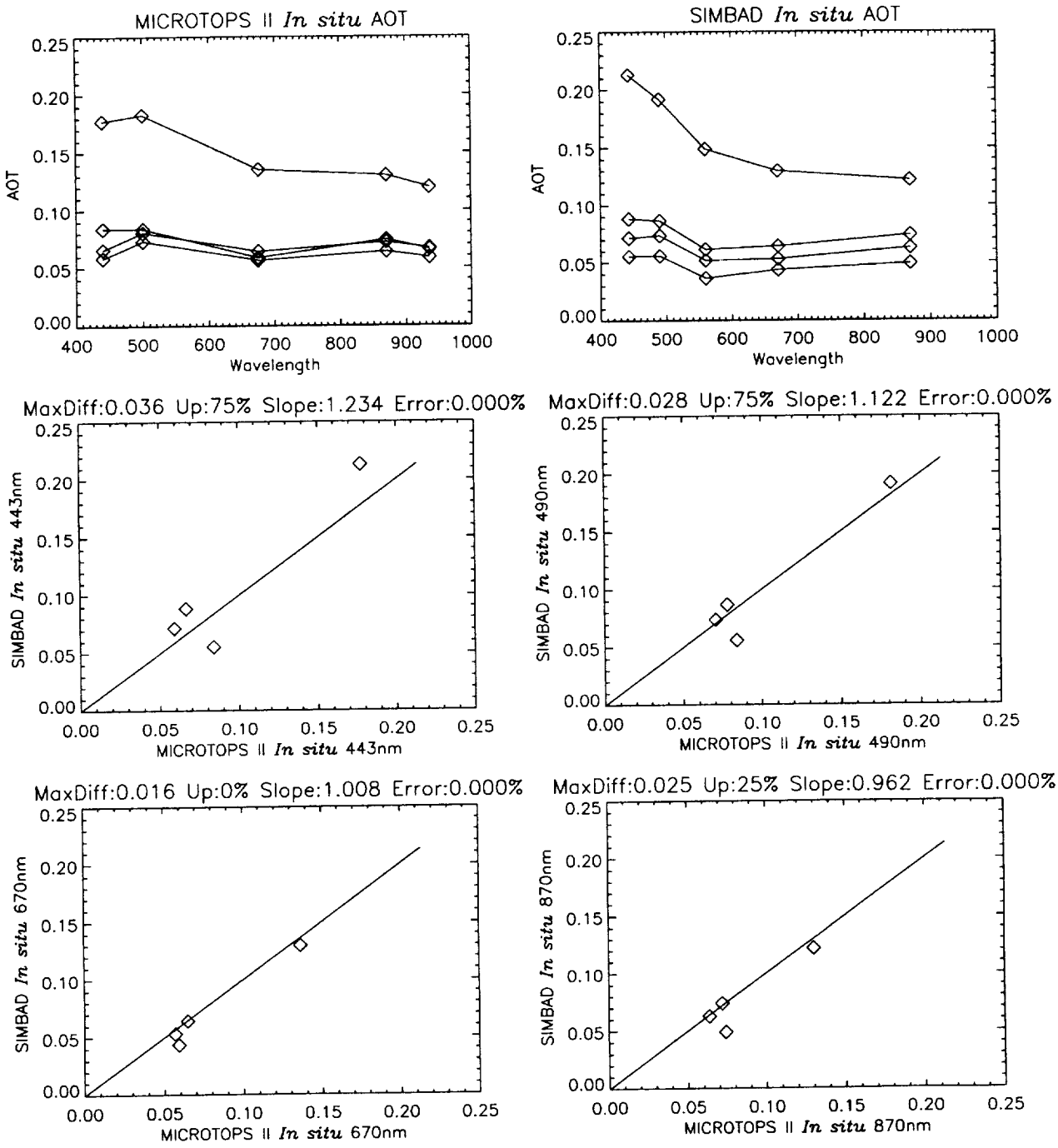

Figure 8.7. Validation of MICROTOPS II and SIMBAD AOT points for the measurements obtained within a maximum of thirty minutes and 15km apart for both sun photometers. Both sets of the AOT observations were screened using the multi-band version of the wavelet-based algorithm.

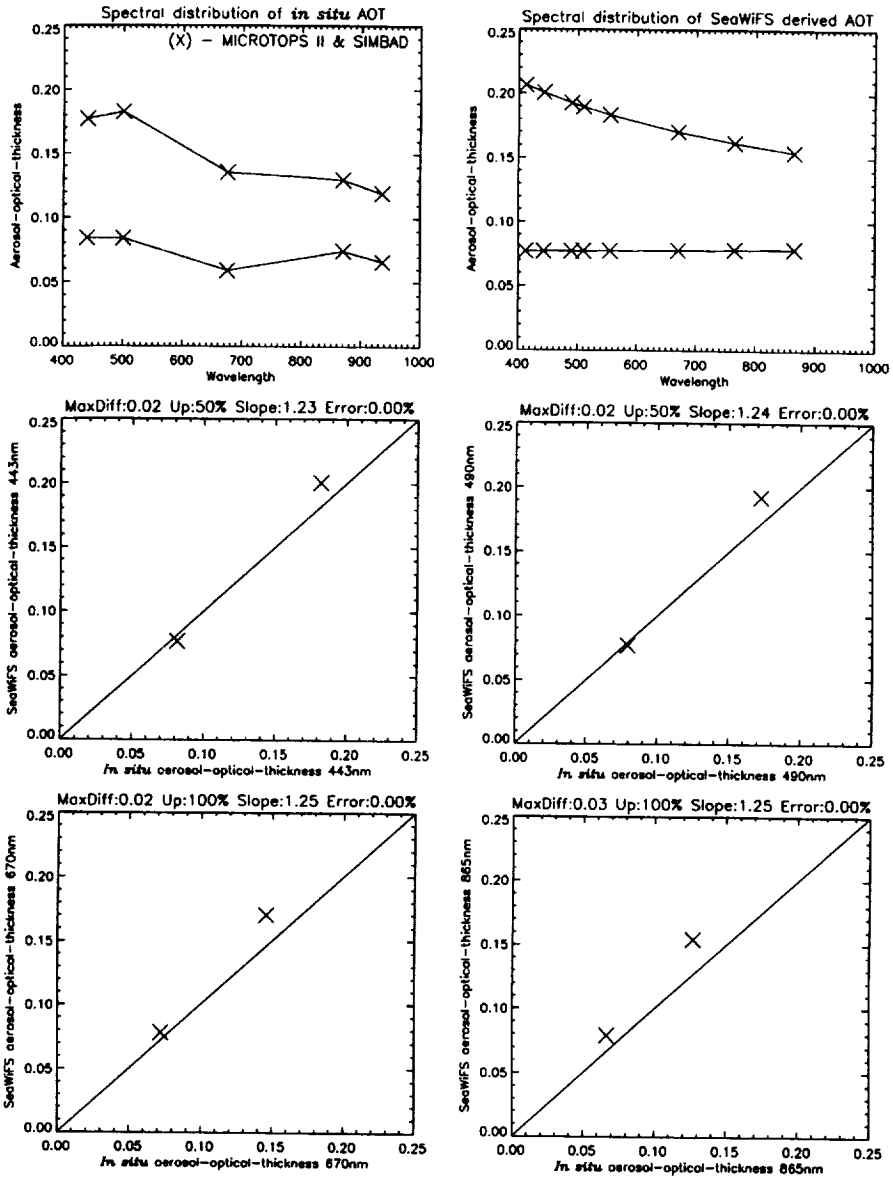

Figure 8.8. Match-up results between SeaWiFS-obtained AOT values and *in situ* AOT points cross-validated between MICROTOPS II and SIMBAD sun photometers. The MICROTOPS II and SIMBAD observations were screened using the multi-band version of the wavelet-based algorithm.

8.7 ADDITIONAL ANALYSES OF MATCH-UP RESULTS

AOT match-up results between satellite-derived and *in situ* observations can be further investigated in a variety of ways. A useful study is to find out whether the AOT comparisons are unbalanced by several aberrant factors which can contribute to uncertainties in comparisons of the two types of data and inaccuracies in the atmospheric correction algorithm. These factors include higher wind speeds and atmospheric variabilities over the match-up geographical locations at the time of satellite imagecapture, higher sun zenith angles or sensor viewing angles, and larger time discrepancies between measurements performed by ground and satellite instruments. Figure 8.9 displays the match-up results from Figure 8.3 in the 865nm band and the correlations between the match-up errors in this band and the following:

- time difference;
- standard deviation of the $\varepsilon(765, 865)$ parameter (ratio of the single scattering aerosol reflectance at the two bands) calculated within

SeaWiFS HRPT or LAC windows of 21x21 pixels centered at the CIMEL geographical locations;
- standard deviation of AOT values obtained within the SeaWiFS windows;
- solar zenith angle; and
- sensor zenith angle.

The figure shows that there are not any noticeable correlations between match-up inaccuracies and these factors.

AOT match-up time series can help discover seasonal trends in AOT distributions and possible miscalibrations of temporarily stationed sun photometers or sky radiometers. Figure 8.10 presents match-up time series for the CIMEL instruments operational in San Nicolas. For this case, unfortunately, a small number of match-up points prohibits any viable analyses. However, better statistics are expected with future match-up results.

In case of suspicious match-up points, the spectral and temporal distribution of sun and sky radiometer daily measurements which comprise the *in situ* match-up point can be displayed and analyzed. Figure 8.11 shows distributions of SIMBAD sun photometer measurements obtained during the INDOEX cruise.

8.8 CONCLUSIONS

This chapter has introduced a number of techniques used to analyze match-ups between satellite-derived and *in situ* AOT levels. The results of AOT match-ups were investigated and recommendations were made for cases where AOT measurements were screened using statistical and wavelet-based algorithms as well as single band (870 nm) and multi-band approaches. The match-ups were compared directly enabling the estimates of the absolute calibration of the satellite sensor's 865nm near-infrared band. Also, the accuracy of the relative near-infrared band calibration was studied using the Ångström coefficient value of the 765nm band. The fitness of the aerosol models for extrapolation of the aerosol path radiance from the near-infrared to visible spectra was investigated for close Ångström satellite and *in situ* match-up cases. More reliable match-up results were obtained using cross-instrument-validated *in situ* AOT points. Finally, several additional match-up analysis methods were outlined.

The SeaWiFS AOT match-up results with *in situ* radiometer observations and Ångström coefficient studies indicate that:

- There are inaccuracies in relative and absolute calibrations of the SeaWiFS near-infrared bands; and
- SeaWiFS aerosol models have flat spectral distributions which are insufficient to correctly extrapolate a large part of extracted near-infrared AOT measures towards the visible spectra.

Nevertheless, further studies are needed to draw more decisive conclusions about sensor and atmospheric correction accuracies. The following investigations are suggested:

- Application of the wavelet-based AOT screening technique to remove cloud-contaminated and erroneous measurements.
- Application of the multi-band version of the screening algorithm to assure the removal of all questionable AOT measurements.
- Application of all available *in situ* AOT data sets derived from a variety of sun and sky radiometers and geographical locations which include coastal sites as well as open ocean.
- Further analysis of match-ups for cross-instrument validated *in situ* AOT points.
- Application of an alternative "absolute" vicarious calibration of the SeaWiFS instrument using *in situ* measurements of water-leaving radiances as well as AOT values (the first results of this technique are described in Chapter 9 of this publication).

REFERENCES

Eplee, R. E. Jr., C. R. McClain, 2000: MOBY Data Analysis for the Vicarious Calibration of SeaWiFS Bands 1-6, NASA Tech. Memo. 2000-206892, In McClain, C. R., E. J. Ainsworth, R. A. Barnes, R. E. Eplee, Jr., F. S. Patt, W. D. Robinson, M. Wang, and S. W. Bailey, SeaWiFS Postlaunch Calibration and Validation Analyses, Part 1, S. B. Hooker and E. R. Firestone, Eds, NASA Goddard Space Flight Center, Greenbelt, Maryland.

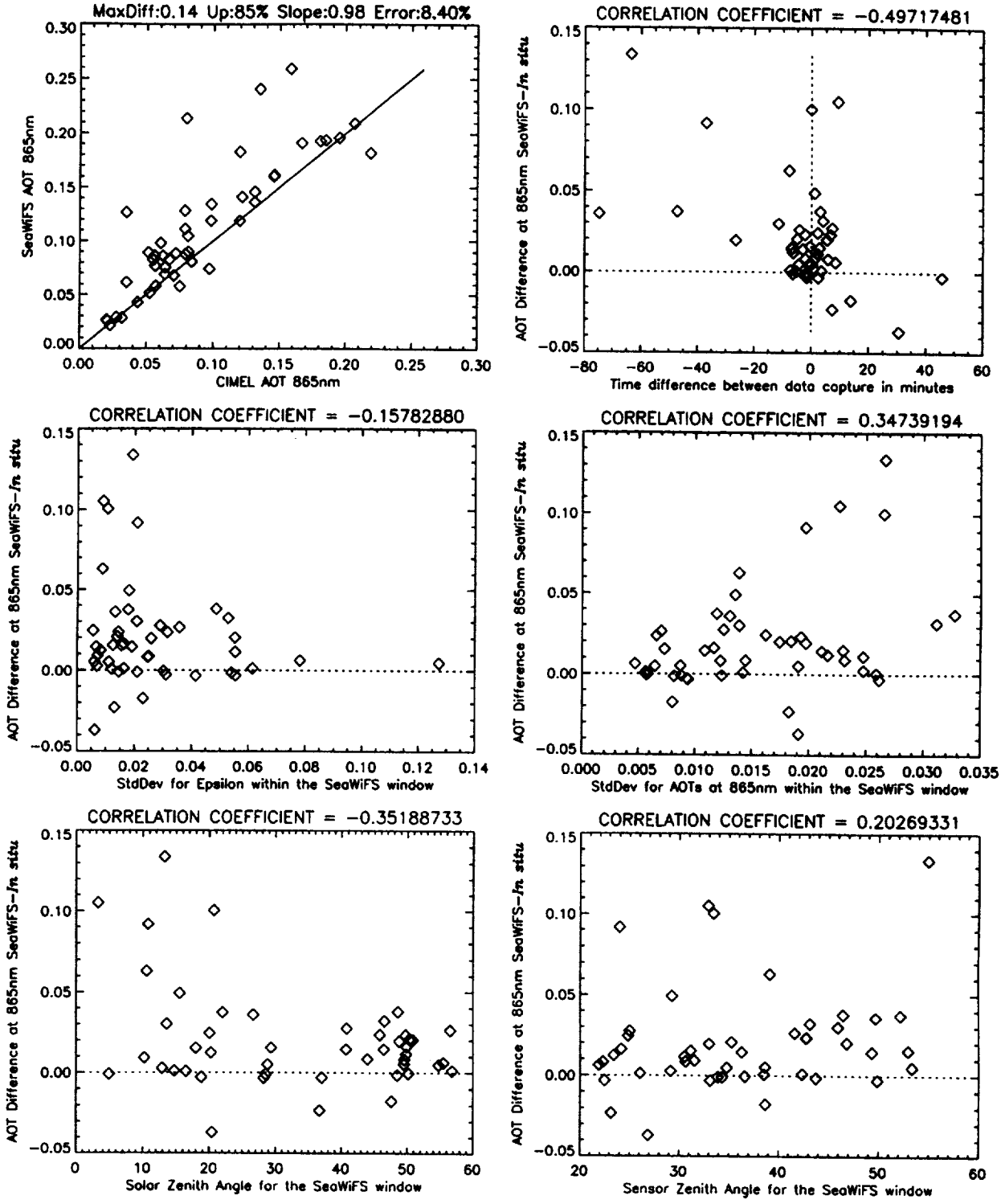

Figure 8.9. Correlations between match-up errors and SeaWiFS imaging and processing characteristics for *in situ* AOT observations captured by different CIMEL sun photometers and screened using the statistical algorithm and a single spectral band centered at 870nm.

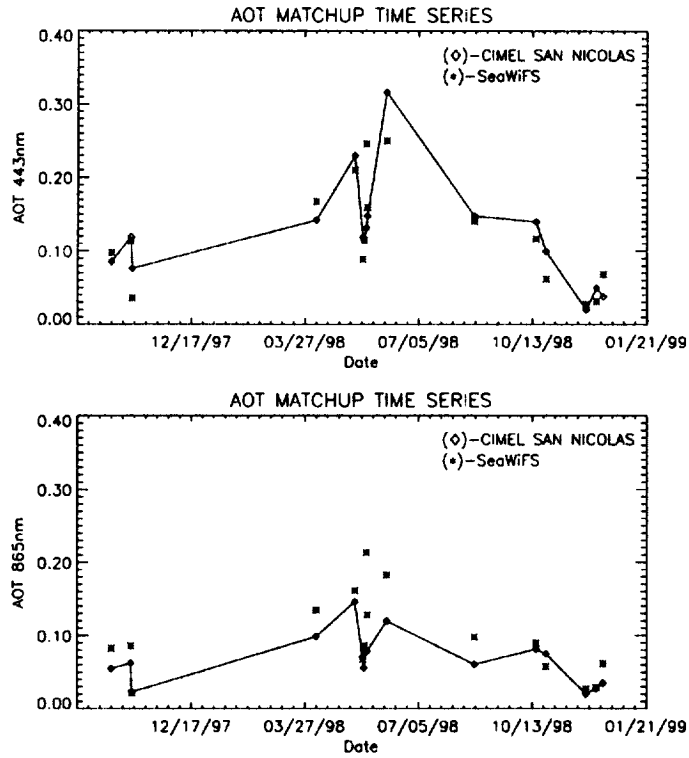

Figure 8.10 Time series of AOT match-up points for CIMEL instruments operational in San Nicolas. CIMEL AOT observations were screened using the statistical algorithm and a single spectral band centered at 870nm.

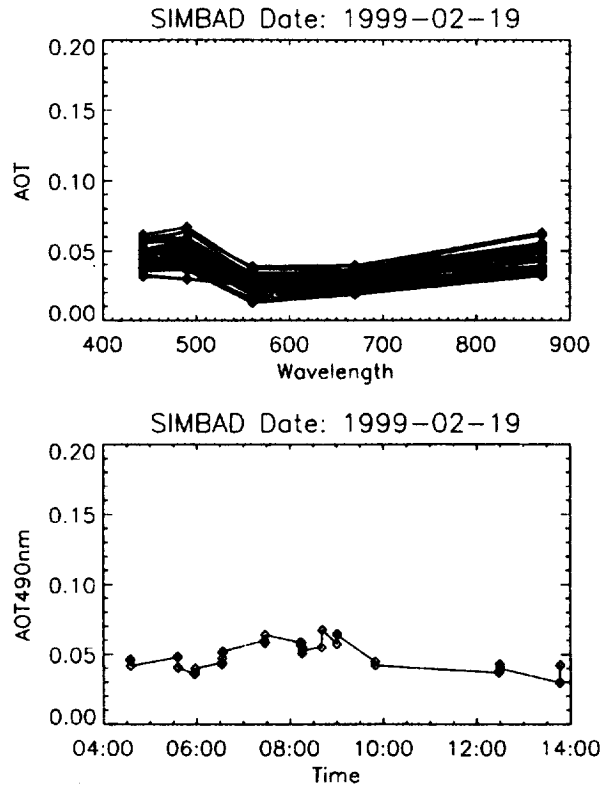

Figure 8.11 Spectral and temporal distributions of daily SIMBAD measurements captured during the INDOEX cruise.

Chapter 9

SeaWiFS Vicarious Calibration: An Alternative Approach Utilizing Simultaneous *In Situ* Observations of Oceanic and Atmospheric Optical Properties.

Bryan A. Franz[1], Ewa J. Ainsworth[1] and Sean Baily[2]
[1]*SAIC General Sciences Corporation, Beltsville, Maryland*
[2]*Futuretech Corporation, Greenbelt, Maryland*

9.1 INTRODUCTION

We will first describe an approach for estimating the top-of-atmosphere (TOA) reflectance using simultaneous measurements of *in situ* water-leaving radiance and aerosol optical thickness at the SeaWiFS wavelengths. This approach can be used to predict the radiance that should be observed in each of the eight SeaWiFS bands, thereby providing a mechanism for direct calibration of the sensor. We apply this technique to the vicarious calibration of SeaWiFS and contrast the results with those obtained for the operational SeaWiFS calibration, through comparison with independent *in situ* measurements of water-leaving radiances and aerosol optical thickness.

9.2 ALGORITHM DESCRIPTION

We begin with the definition of the reflectance, $\rho = \pi L / \mu_0 F_0$, where L is the radiance in a given solar and viewing geometry, F_0 is the extraterrestrial solar irradiance, and μ_0 is the cosine of the solar zenith angle. The total reflectance measured at the top of the ocean-atmosphere system, $\rho_t(\lambda)$, can be written as in Equation 9.1.

In the equation, $\rho_r(\lambda)$ is the reflectance resulting from multiple scattering by air molecules in the absence of aerosols, $\rho_a(\lambda)$ is the reflectance resulting from multiple scattering by aerosols in the absence of air molecules, $\rho_{ra}(\lambda)$ is the multiple interaction term between molecules and aerosols (Deschamps et al., 1983), $\rho_g(\lambda)$ is the direct reflectance of solar rays from the sea surface to the sensor (Sun glint or glitter), $\rho_f(\lambda)$ is the reflectance at the sea surface that arises from sunlight and skylight reflecting from whitecaps on the surface (Gordon and Wang, 1994a), and $\rho_w(\lambda)$ is the water-leaving reflectance, which is the desired quantity in ocean color remote sensing. The $t(\lambda)$ term is the atmospheric diffuse transmittance (Wang, 1999) that accounts for the effects of propagating a diffuse light source from the sea surface to the TOA. Similarly, $T(\lambda)$ is the direct transmittance which accounts for the effects of propagating a beam of light from the sea surface to the TOA. The $t_g(\lambda)$ term represents the gaseous transmittance, which accounts for absorption due to ozone, oxygen, and water vapor.

The calibration process involves computing the TOA reflectance from known and measured components of Equation 9.1, and comparing the predicted value with the observed value from SeaWiFS to derive a calibration gain and possibly an offset. In practice, the molecular scattering signal is well understood and can be accurately computed (Gordon et al., 1988). The white cap signal is generally small, and it can be predicted using statistical relationships and ancillary wind speed data (Gordon and Wang, 1994a). Furthermore, the residual uncertainties can be minimized by using observations with low surface wind speeds. The Sun glint term can be predicted from solar and viewing geometry and ancillary wind field data (Cox and Munk, 1954), but in practice it is easily avoided by limiting observations to geometries which do not allow for direct reflectance of the solar rays into the sensor. Avoiding Sun glint also alleviates the need to know the direct transmittance. The gaseous transmittance can be predicted from ancillary data on ozone and water vapor concentrations, solar and viewing geometries, and the spectral band passes of the sensor (Gordon and Wang, 1994b; Ding and Gordon, 1995; Gordon, 1995).

$$\rho_t(\lambda) = [\rho_r(\lambda) + \rho_a(\lambda) + \rho_{ra}(\lambda) + T(\lambda)\rho_g(\lambda) + t(\lambda)\rho_f(\lambda) + t(\lambda)\rho_w(\lambda)]t_g(\lambda), \quad (9.1)$$

This leaves the water-leaving reflectances, aerosol and Rayleigh-aerosol terms, and the diffuse transmittance to be derived from *in situ* measurements or additional assumptions.

In practice, the water-leaving reflectance values at a given location can be derived from *in situ* optical measurements of the upwelling radiance. The remaining terms in Equation 9.1 require some knowledge or assumptions about the aerosol type and concentration. This includes the diffuse transmittance term, which is dominated by molecular scattering effects but is weakly influenced by the aerosols (Wang, 1999).

The standard approach used by the SeaWiFS project to account for the influence of aerosols in the vicarious calibration (Barnes et al., 2000; Robinson and Wang, 2000; Eplee and McClain, 2000) has been to make two assumptions: 1) that the gain at 865nm is known and fixed at the pre-launch value, and 2) that the aerosol type near the calibration site is characterized by an average maritime model (Robinson and Wang, 2000). The first assumption essentially fixes the aerosol concentration, while the latter assumption determines the relative calibration between the 765 and 865nm channels and the extrapolation of aerosol reflectance to the visible bands. This has been the calibration technique employed for all SeaWiFS processing to date.

The focus of the present work is to develop a technique which eliminates or reduces the aerosol assumptions by making use of aerosol optical thickness measurements which have been collected in conjunction with *in situ* water-leaving radiances. What we require is a method to relate measurements of aerosol optical thickness to total multiple-scattering aerosol reflectance, including the effect of Rayleigh-aerosol interaction. In the single-scattering approximation, the aerosol reflectance, $\rho_{as}(\lambda)$, can be computed as

$$\rho_{as}(\lambda) = \frac{\omega_0(\lambda)\tau_a(\lambda)P_a(\lambda,\Theta)}{4\mu_0\mu} \quad (9.2)$$

where the subscript s denotes single-scattering. In Equation 9.2, $\omega_0(\lambda)$ is the single-scattering aerosol albedo, $\tau_a(\lambda)$ is the aerosol optical depth, $P_a(\lambda,\Theta)$ is the scattering phase function for a scattering angle of Θ, and μ_0 and μ are the cosines of the solar and view zenith angles, respectively. The aerosol optical thickness at each wavelength can be obtained from available *in situ* measurements, but the single scattering albedo and scattering phase function require knowledge of the aerosol type.

A simple approach to characterize the aerosol type is to define the Ångström coefficient, $\alpha(\lambda_1,\lambda_2)$, as

$$\frac{\tau_a(\lambda_1)}{\tau_a(\lambda_2)} = \left(\frac{\lambda_1}{\lambda_2}\right)^{-\alpha} \quad (9.3)$$

Using this characterization, we can compare the measured Ångström coefficient to the Ångström coefficients associated with a set of aerosol models, and from the models with similar Ångström coefficient we can retrieve the single-scattering albedo and scattering phase function. In general, the measured Ångström coefficient will fall between two of the models, so we compute Equation 9.2 for each model (call them $\rho_{as1}(\lambda)$ and $\rho_{as2}(\lambda)$) and we define a mixing ratio, R, to interpolate between the two models. Before we interpolate, however, we take advantage of the model relationships developed by Gordon and Wang (Gordon and Wang, 1994b) to translate the single-scattering aerosol reflectances for model i to multiple-scattering aerosol reflectance with Rayleigh-aerosol interaction, $[\rho_a(\lambda)+\rho_{ar}(\lambda)]_i$. Thus, we can now compute the total aerosol reflectance as in Equation 9.4.

$$\rho_a(\lambda) + \rho_{ar}(\lambda) = R[\rho_a(\lambda) + \rho_{ar}(\lambda)]_1 + (1-R)[\rho_a(\lambda) + \rho_{ar}(\lambda)]_2 \quad (9.4)$$

In a similar way, we can compute the Rayleigh-aerosol diffuse transmittance for each aerosol model (Wang, 1999) and interpolate to retrieve the total diffuse transmittance.

9.3 APPLICATION TO SeaWiFS CALIBRATION

The primary calibration site for the SeaWiFS project is the MOBY buoy (Clark et al., 1997) located off the coast of Lanai, Hawaii. Since 1996, the MOBY buoy has been continuously collecting upwelling radiance measurements at fine spectral resolution through the visible wavelength regime. MOBY measurements are collected for each satellite overpass, and processed to provide water-leaving radiances at each of the SeaWiFS visible band passes (412 – 670 nm). The water-leaving radiances in the two SeaWiFS near infrared (NIR)

bands can be assumed to be negligible, or estimated from a case 1 model (Siegel et al., 2000).

In 1998, the SIMBIOS Project began operating a CIMEL sun photometer at Lanai as part of the Aerosol Robotic Network, AERONET (Holben et al., 1998; Holben et al., 2000; Wang et al., 2000). CIMEL AOT points are first extracted using the wavelet-based multi-band screening approach (see Chapter 6). CIMEL sun photometer measures aerosol optical thickness at seven wavelengths (340, 380, 440, 500, 670, 870, and 1020 nm). For these data to be useful as inputs for the calibration technique described herein, an estimate of the optical thickness at each of the SeaWiFS bands must be determined. To do this we apply a simple linear fit to $\log(\tau_a)$ vs $\log(\lambda)$. Using this fit, we interpolate the $\tau_a(\lambda)$ to the SeaWiFS nominal wavelengths. If the residuals from this linear fit are more than five percent of the measured value, the record is rejected.

We have identified 38 SeaWiFS scenes over MOBY for which there exist contemporaneous aerosol measurements at Lanai, and which pass the standard SeaWiFS exclusion criteria for vicarious calibration (Eplee and McClain, 2000). Additionally, measurement were excluded if the *in situ* measured τ_a (865) was less than 0.02 or the wind speed was greater than 5 m/s. The threshold on τ_a (865) was set to account for the uncertainty in the calibration of the CIMEL aerosol optical thickness retrievals. The AERONET group reports an uncertainty of +/- 0.01 in $\tau_a(\lambda)$ (Holben et al., 1998). The wind speed threshold was set to reduce uncertainties in the atmospheric correction algorithm, as the Rayleigh and whitecap radiances are both wind speed dependent. This left only 5 calibration points. Using the inversion technique described above on these 5 points, we have computed a set of vicarious gains for all eight SeaWiFS bands. These alternative gains are listed with the operational gains for SeaWiFS reprocessing #3 in Table 9.1.

9.4 RESULTS AND DISCUSSION

As reproduced from Bailey et al. (Bailey et al., 2000), the SeaWiFS bio-optical match-up results of Figure 1 were processed using the operational gains. A comparison of the coefficients in Table 9.1 would suggest that the assumption of unity for the gain in band 8 is an overestimate on the order of 5%. Overall the results of the match-ups with the alternative gains, as presented in Figure 9.2, show that bio-optical comparisons between *in situ* measurements and SeaWiFS derived values are not greatly affected by this change of calibration. Comparisons of the statistics by band are found in Table 9.2. From the comparison of the alternative gains to the operational gains, we find a slight improvement in bands 4 and 5 and a slight degradation in the bio-optical match-up results for band 1.

The results of AOT match-ups between *in situ* and SeaWiFS measurements indicate that the alternative vicarious gain coefficients can cause improvements in the outcome of SeaWiFS atmospheric correction in terms of AOT levels. This is because the alternative calibration method eliminates *a priori* assumptions on band 8 calibration and aerosol type over MOBY, which strongly influence aerosol determination in the SeaWiFS processing. Figure 9.3 shows the comparison of match-ups obtained using the operational gains, top two graphs, and the alternative gains, bottom two graphs. *In situ* AOT points were extracted using the statistical screening on the single CIMEL 870nm band (see Chapter 6). Only the results in the 443nm and 865nm bands are displayed.

For the operational gains, the slope of a linear fit between both types of AOT observations is close to 1 in the 865nm band and the intercept indicates a small shift of 0.02 in the AOT value. The application of alternative gains causes the slope of the linear fit in the 865nm band to decrease, however, the intercept is the same and the overall inaccuracy of match-ups is reduced. For the alternative gains, the large majority of AOT points are closely clustered along the y=x line and there are only a few outliers which adversely influence the statistics.

The alternative SeaWiFS calibration method uses existing aerosol models to provide the estimate of the multi-scattering aerosol reflectance with Rayleigh-aerosol interaction. These aerosol models have been noticed before to exhibit AOT spectral distributions which are flatter than the AOT distributions obtained from *in situ* measurements (Chapter 7). Therefore, *in situ* AOT values are generally underestimated by the SeaWiFS algorithm in the shorter visible wavelengths. This underestimation is decreased but is still significant when the alternative calibration gains are applied in the SeaWiFS processing, as shown for the band at 443nm in Figure 9.3. In this band, the inaccuracy of the match-ups is decreased somewhat with the application of the alternative gain set, and the slope of the linear fit between *in situ* and SeaWiFS AOT measurements is only slightly improved.

Figure 9.4 illustrates Ångström coefficient match-ups computed for the 765nm band relative to

the 865nm band, which are the bands used to select an aerosol model in the SeaWiFS processing. The alternative calibration approach forced a number of SeaWiFS AOT measurements to produce Ångström coefficients that more closely approximate the coefficients of *in situ* observations. The inaccuracy of Ångström coefficients computed with the alternative calibration is half of the inaccuracy produced with the operational gains. However, this improvement was not sufficient to produce substantially better AOT match-ups in the visible bands.

The improved AOT match-up results indicate that there are inaccuracies in the relative and absolute calibrations of the SeaWiFS near-infrared bands. However, the spectral shape of existing aerosol models may cause more problems in estimating atmospheric contribution to the signal at the top-of-the-atmosphere than do these calibration errors. It has been noted that SeaWiFS aerosol models commonly have flatter spectral distributions than those obtained from *in situ* AOT measurements. Because of this, the aerosol path radiance models produce underestimated AOT values when extrapolated from the near-infrared spectra to the SeaWiFS visible bands. Before final conclusions can be drawn, however, additional studies should be performed using a larger set of *in situ* data to confirm these results. These studies may include the use of global aerosol measurements to determine the NIR calibration of SeaWiFS, independent of the MOBY observations. Some enhanced screening of the aerosol measurements may also be necessary, as discussed in Chapter 7 of this document.

9.5 CONCLUSIONS

We have described a procedure to predict TOA reflectance, and hence calibration gains, from well-known atmospheric components and simultaneous measurements of water-leaving radiance and aerosol optical thickness. Relative to the standard SeaWiFS calibration technique, this procedure eliminates the requirements for *a priori* knowledge of the calibration at 865nm, and it does not require an assumption of aerosol type. Instead, we have used the measured aerosol optical thickness to define the aerosol concentration, and we have used the measured Ångström coefficient to characterize the aerosol type.

The major limitation of this approach is that we still must use aerosol models to relate the measured aerosol optical thicknesses to aerosol reflectances, and models may not be accurate or uniquely defined with respect to Ångström coefficient. Model uncertainties can be minimized, however, by selecting sites where historical evidence would suggest that the aerosols are generally homogenous and well characterized by existing models.

The major advantage of incorporating aerosol optical thickness measurements into the calibration process is that we can now derive an independent estimate of the calibration at 765 and 865nm. The results of our preliminary analysis compare well with a growing body of evidence that the SeaWiFS 865nm channel overestimates the TOA radiance by 4 to 10% (Barnes et al., 2000). The gains retrieved using this alternative method produce minor changes in the SeaWiFS retrieved water-leaving radiances, but a marked improvement in the SeaWiFS retrieved aerosol optical thickness and Ångström exponent.

REFERENCES

Bailey S. W., C. R. McClain, P. Jeremy Werdell, and Brian D. Schieber, 2000: Normalized Water-Leaving Radiance and Chlorophyll a Match-up Analyses. In: McClain, C. R., R. A. Barnes, R. E. Eplee, Jr., B. A. Franz, N. C. Hsu, F. S. Patt, C. M. Pietras, W. D. Robinson, B. D. Schieber, G. M. Schmidt, M. Wang, S. W. Bailey, and P. J. Werdell, SeaWiFS Postlaunch Calibration and Validation Analyses, Part 2. NASA Tech. Memo. 2000-206892, Vol. 10, S. B. Hooker and E. R. Firestone, Eds., NASA Space Flight Center, Greenbelt, Maryland, 45- 52.

Barnes, R.A., R. E. Eplee Jr., W. D. Robinson, G. M. Schmidt, F. S. Patt, S. W. Bailey, M. Wang, and C. R. McClain, 2000: The calibration of SeaWiFS on orbit, Proc. SPIE, 31 July – 4 August.

Barnes R. A., R. E. Eplee, W. D. Robinson, G. M. Schmidt, F. S. Patt, S. W. Bailey, M. Wang, C. R. McClain, 2000: The calibration of SeaWiFS, Proc. 2000 Conf. on Characterization and Radiometric Calibration for Remote Sensing, Logan, Utah, September 19-21.

Clark D. K., H. R. Gordon, K. K. Voss, Y. Ge, W. Brokenow, and C. Trees, 1997: Validation of atmospheric correction over oceans, J. Geophys. Res., vol. 102, 17209-17217.

Cox C. and W. Munk, 1954: Measurements of roughness of the sea surface from photographs of the Sun's glitter, J, Opt. Soc. Am., 44, 838-850.

Deschamps, P. Y., M. Herman, and D. Tanre, 1983: Modeling of the atmospheric effects and its application to the remote sensing of ocean color, Appl. Opt., vol. 22, 3751-3758.

Ding K. and H. R. Gordon, 1995: Analysis of the influence of O_2 A-band absorption on atmospheric correction of ocean-color imagery, Appl. Opt., vol. 34, 2068-2080.

Eplee, R. E. Jr., C. R. McClain, 2000: MOBY Data Analysis for the Vicarious Calibration of SeaWiFS Bands 1-6, NASA Tech. Memo. 2000-206892, In McClain, C. R., E. J. Ainsworth, R. A. Barnes, R. E. Eplee, Jr., F. S. Patt, W. D. Robinson, M. Wang, and S. W. Bailey, SeaWiFS Postlaunch Calibration and Validation Analyses, Part 1, S. B. Hooker and E. R. Firestone, Eds, NASA Goddard Space Flight Center, Greenbelt, Maryland.

Gordon, H. R., 1995: Remote sensing of ocean color: a methodology for dealing with broad spectral bands and significant out-of-band response, Appl. Opt., vol. 34, 8363-8374.

Gordon, H. R., J, W. Brown, R. H. Evans, 1988: Exact Rayleigh scattering calculations for use with Nimbus 7 Coastal Zone Color Scanner, Appl. Opt., vol. 27, 862-871.

Gordon H. R. and M. Wang, 1994a: Influence of oceanic whitecaps on atmospheric correction of ocean-color sensor, Appl. Opt., vol. 33, 7754-7763.

Gordon H. R. and M. Wang, 1994b: Retrieval of water-leaving radiance and aerosol optical thickness over the oceans with SeaWiFS: a preliminary algorithm, Appl. Opt., vol. 33, 443-452.

Holben, B. N., T. F. Eck, I. Slutsker, D. Tanre, J. P. Buis, A. Setzer, E. Vermote, J. A. Reagan, Y. Kaufman, T. Nakajima, F. Lavenu, I. Jankowiak, and A. Smirnov 1998: AERONET - A federated instrument network and data archive for aerosol characterization, Rem. Sens. Environ., 66, 1-16.

Holben, B. N., D. Tanre, A. Smirnov, T. F. Eck, I. Slutsker, N. Abuhassan, W. W. Newcomb, J. Schafer, B. Chatenet, F. Lavenue, Y. J. Kaufman, J. Vande Castle, A. Setzer, B. Markham, D. Clark, R. Frouin, R. Halthore, A. Karnieli, N. T. O'Neill, C. Pietras, R. T. Pinker, K. Voss, G. Zibordi, 2000: An emerging ground-based aerosol climatology: Aerosol Optical Depth from AERONET, J. Geophys. Res., In press.

Robinson W. D. and M. Wang, 2000: Vicarious Calibration of SeaWiFS Band 7, NASA Tech. Memo. 2000-206892, In C. R. McClain, E. J. Ainsworth, R. A. Barnes, R. E. Eplee, Jr., F. S. Patt, W. D. Robinson, M. Wang, and S. W. Bailey, SeaWiFS Postlaunch Calibration and Validation Analyses, Part 1, S. B. Hooker and E. R. Firestone, Eds, NASA Goddard Space Flight Center, Greenbelt, Maryland.

Siegel, D. A., M. Wang, S. Moretorena, and W. Robinson, 2000: Atmospheric correction of satellite ocean color imagery: the black pixel assumption, Appl. Opt., vol. 39 no. 21, 3582-3591.

Wang, M., 1999: Atmospheric correction of ocean color sensors: Computing atmospheric diffuse transmittance, Appl. Opt., vol. 38, 451-455.

Wang, M., S. Bailey, C. Pietras, C. R. McClain, and T. Riley, 2000: SeaWiFS Aerosol Optical Thickness Match-up Analysis, NASA Tech. Memo. 2000-206892, In C. R. McClain, R. A. Barnes, R. E. Eplee, Jr., B. A. Franz, C. H. Hsu, F. S. Patt, C. M. Pietras, W. D. Robinson, B. D. Schieber, G. M. Schmidt, M. Wang, S. W. Bailey, and P. J. Werdell, SeaWiFS Postlaunch Calibration and Validation Analyses, Part 2, S. B. Hooker and E. R. Firestone, Eds, NASA Goddard Space Flight Center, Greenbelt, Maryland.

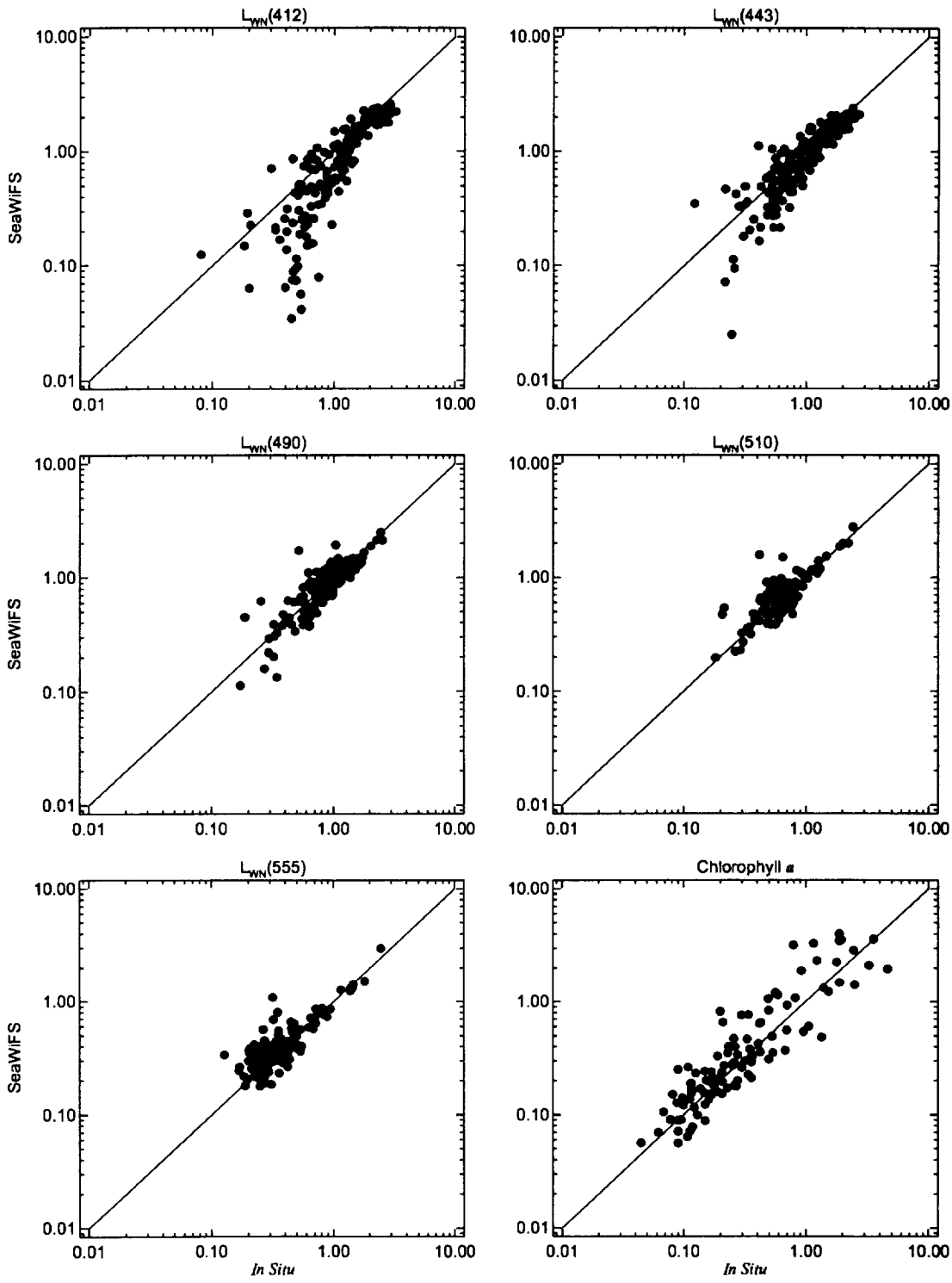

Figure 9.1. *In situ* comparison with SeaWiFS retrieved normalized water-leaving radiances when using operational vicarious gains.

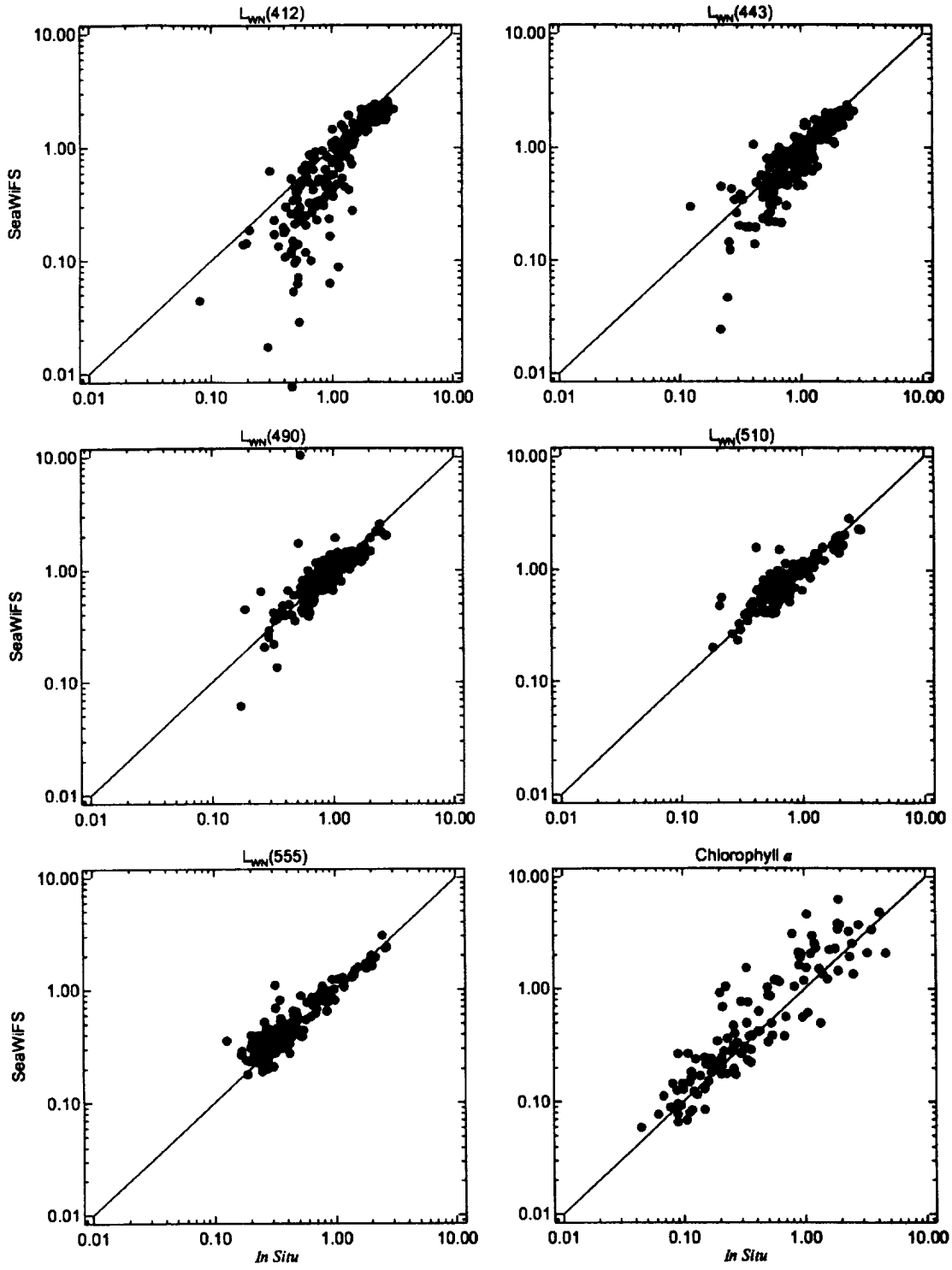

Figure 9.2. *In situ* comparisons to SeaWiFS retrieved water-leaving radiances when using alternative, AOT-based vicarious gains.

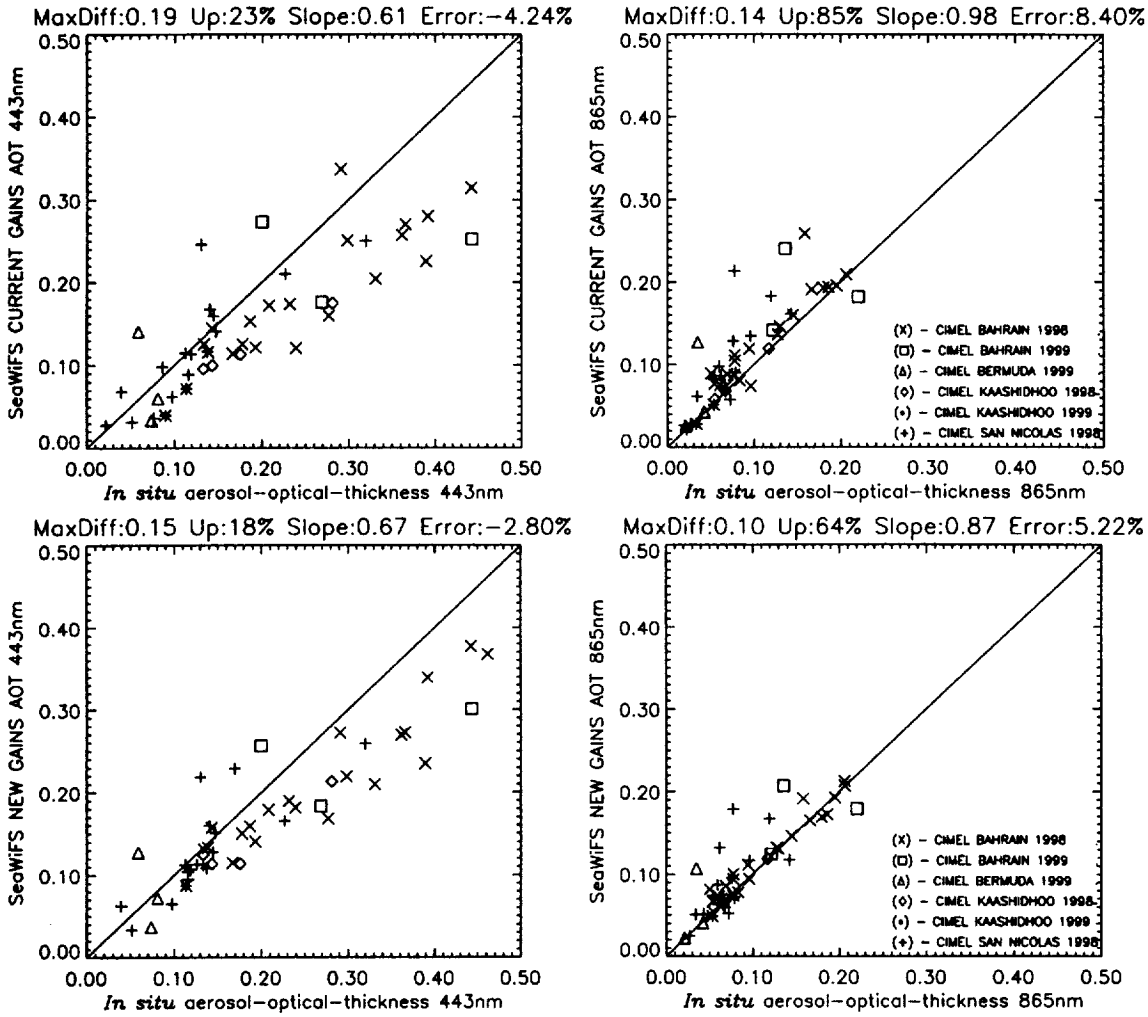

Figure 9.3. Comparison of AOT match-ups in the 443nm and 865nm bands for the operational and alternative set of SeaWiFS calibration gains.

Table 9.1 SeaWiFS vicarious gain coefficients using the inverse technique.

SeaWiFS Band	Band 1	Band 2	Band 3	Band 4	Band 5	Band 6	Band 7	Band 8
Gain Factor	1.005726	0.995034	0.968053	0.989528	0.995204	0.953351	0.923352	0.955989

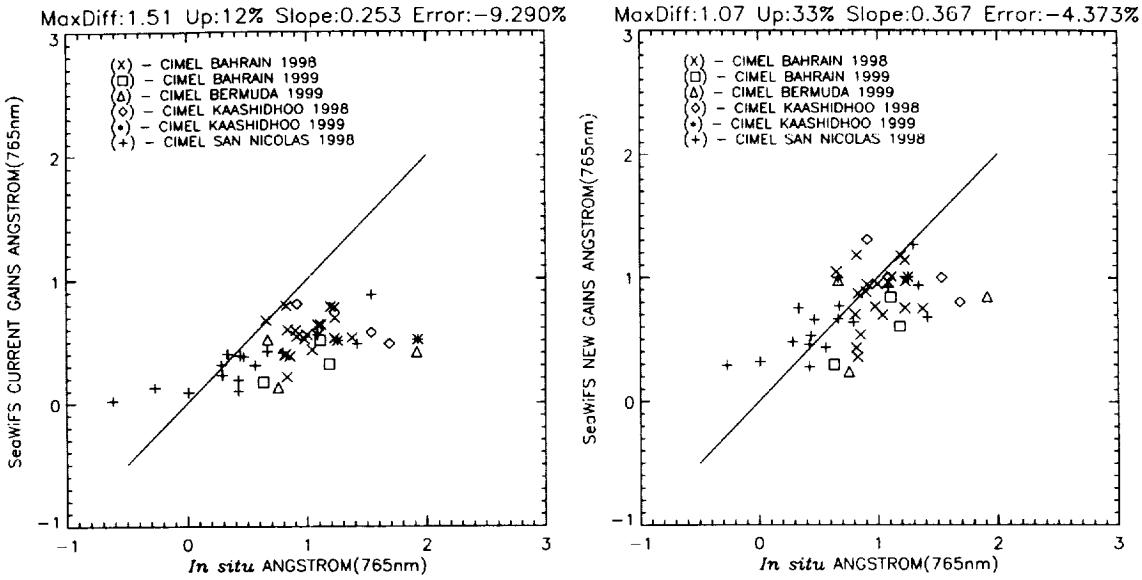

Figure 9.4. Comparison of aerosol Ångström coefficients in the 765nm band relative to the 865nm band for the AOT match-up points and the operational and alternative set of SeaWiFS calibration gains.

Table 9.2 Statistical comparison between operation vicarious gain matchup results and the alternative vicarious gain matchup results.

SeaWiFS Band	SeaWiFS :In situ Ratio	Std. Dev.	R-square	N
All Match-ups				
Alternative Vicarious Calibration Gains				
1	0.7135	0.3085	0.6478	209
2	0.9176	0.3040	0.7618	228
3	1.0203	0.2859	0.7514	233
4	1.0876	0.3140	0.7011	221
5	1.1278	0.3182	0.8387	233
Operational Vicarious Calibration Gains				
1	0.7929	0.3255	0.7175	192
2	0.9621	0.3333	0.7641	202
3	1.0122	0.2970	0.7559	207
4	1.0793	0.3275	0.5975	195
5	1.0993	0.3385	0.6952	207
Case 1 Match-ups				
Alternative Vicarious Calibration				
1	0.8273	0.1997	0.8218	118
2	0.9576	0.2296	0.8313	140
3	1.0140	0.2211	0.7575	157
4	1.0672	0.2338	0.4432	143
5	1.1031	0.2772	0.3822	146
Operational Vicarious Calibration				
1	0.8520	0.2146	0.8132	125
2	0.9628	0.2407	0.8282	145
3	0.9906	0.2171	0.7508	156
4	1.0403	0.2308	0.3392	143
5	1.0560	0.2697	0.3454	150

Appendix A

SeaBASS Data File Format

P. Jeremy Werdell[1], Sean Bailey[1] and Giulietta S. Fargion[3]
[1]*Science System and Applications Inc., Lanham, Maryland*
[2]*Future Tech Corporation, Greenbelt, Maryland*
[3]*SAIC General Sciences Corporation, Beltsville, Maryland*

SeaBASS HEADERS

Each header begins with a '/' and every data file opens with 'begin_header'. The headers are then listed in any order, as long as the list ends with 'end_header'. A value of 'NA' (not available or applicable) is assigned to any header where information cannot be provided. Data files with missing headers will not be accepted for submission to SeaBASS. A description of each follows.

'Data_file_name' simply provides the name of the data file. 'Affiliations', 'investigators', and 'contact' provide information on the contributing researchers. The primary investigator is listed first, followed by any associate investigators. Commas separate multiple entries, and white spaces and apostrophes are not allowed. 'Contact' is the electronic mail address of the contributor. 'Experiment', 'cruise', and 'station' record information on the long-term experiment (if available), the specific cruise, and the station within the cruise. For each of the latter, an entry of 'SIMBIOS' is not permitted. 'Documents' refers to cruise reports, logs, and associated documentation that provide additional information about the experiment or cruise. 'Calibration_files' points to additional file(s) that contain the coefficients and techniques used to calibrate the instruments used in data collection. The files referred to by 'documents' and 'calibration_files' must accompany the data files at the time of submission.

'Data_status' describes the condition of the data file, accepting values of preliminary, update, and final. 'Preliminary' is used when the data are submitted for the first time and the investigator intends to analyze the data further. 'Update' indicates the data are being resubmitted and informs the Project that an additional resubmission will occur in the future. 'Final' is used when the investigator has no intention of revisiting the data set. 'Data_type' describes the general collection method of the data. Accepted values include: 'cast' for vertical profiles (e.g. optical packages, CTD); 'flow_thru for continuous data (e.g. underway flow through systems); 'above_water' for above surface radiometry data (e.g. ASD, SIMBAD); 'sunphoto' for sunphotometry data (e.g. MicroTops, PREDE); 'mooring' for moored data and buoy data; 'drifter' for drifter and drogue data; 'scan' for discrete hyperspectral measurements (e.g., absorption spectra); and 'pigment' for laboratory measured pigment data (fluorometry, spectrophotometry, HPLC).'North_latitude','south_latitude','east_long itue', 'west_longitude', 'start_date', end_date', 'start_time', and 'end_time' provide information on the location, date, and time data were collected. Each entry should be the extreme value for the entire data file. For example, 'north_latitude' refers to the coordinate furthest north data in the file were collected. 'Start_time' and 'end_time' refer to the earliest and latest time-of-day data in the file were collected. The latter do not refer to the time data collection began and data collection ceased, respectively. Latitude and longitude are listed in decimal degrees, with coordinates north of the equator or east of the Prime Meridian set positive and south of the equator or west of the Prime Meridian set negative. Dates have the format 'YYYYMMDD'. Times have the format 'HH:MM:SS' and are listed in Greenwich Mean Time (GMT).

'Cloud_percent', 'wave_height', 'wind_speed', 'secchi_depth'', 'measurement_depth', and 'water_depth' provide ancillary information about the station, when available. 'Wave_height' and 'water_depth' have units of meters and 'wind_speed' has units of meters per second. A value for 'measurement_depth' is included when the file contain data collected at a discrete depth (e.g., bottle samples or buoy/moored radiometers).

'Fields' names each of the columns of *in situ* data presented below the headers. Each entry describes the data in a one column, and every column must have an entry. 'Units' provides the units for each column of data. Every value in 'fields' must also have an equivalent entry in

'units'. 'Missing' refers to a null value used as a placeholder for any missing data point. Each row of data must contain the same number of columns as defined in the 'fields' header. 'Delimiter' indicates how the columns of data are delimited. Accepted delimiters include tabs, spaces, and commas, but only one delimiter is permitted per data file. Finally, if the investigators wish to include additional comments about the data file, they may do in the within the header boundaries. Lines of comments begin with a '!' and may include any and all text characters and white space. Comment comments include addition ancillary information about the data file, sea and sky states, difficulties encountered during data collection, methods of data collection, instruments used, and a description of nonstandard SeaBASS field name included in the data file. A list and description of the SeaBASS metadata headers is available online at http://seabass.gsfc.nasa.gov/seabass_header.html. This list is updated regularly.

FIELD NAMES AND UNITS

In an effort to ensure compatibility within the SeaBASS data archive, and to facilitate the development of the expanded version of the SeaBASS database, a standard set of case-insensitive field names and units has been adopted. While the list of standardized field names is reasonably comprehensive, it cannot account for all the possible data types one might wish to provide to the SeaBASS archive. If a data type to be submitted to SeaBASS does not fall under one of the predefined standard field names, the investigator may still include the data. Note that the standardized set is updated as the need arises (e.g. a data parameter is commonly submitted or queried). Non-standard data will be archived, however, the data values will not be ingested into the online database. The data will be retrievable, but only with the original archived file, not as a separate dataset. A list of the standardized field names and units is available online at http://seabass.gsfc.nasa.gov/cgi-bin/stdfields.cgi. This list is updated regularly (Table 1A).

Table 1A. SeaBASS Standardized Fieldnames and Units as of June 2000. (###.# = wavelength).

Fieldname	Units	Description
a###.#	1/m	Total absorption coefficient
aaer###.#	1/m	Absorption coefficient of atmospheric aerosols
ad###.#	1/m	Absorption coefficient of detrius
adg###.#	1/m	Absorption coefficient of detrital+gelbstoff
ag###.#	1/m	Absorption coefficient of CDOM
altitude	m	Altitude (above sea level)
am	unitless	Airmass (calculable from time/position)
angstrom	unitless	Angstrom exponent
AOT###.#	unitless	Aerosol optical thickness
ap###.#	1/m	Absorption coefficient of particles
aph###.#	1/m	Absorption coefficient of phytoplankton
a*ph###.#	1/m	Chl a-specific aph
At	degreesC	Air temperature
bb###.#	1/m	Backscatter
bincount	none	Number of records averaged into a bin
bp###.#	1/m	Particle scattering coefficient
c###.#	1/m	Beam attenuation coefficient
cloud	%	Percent cloud cover
cond	mmho/cm	Conductivity
depth	m	Depth of measurement
Ed###.#	uW/cm^2/nm	Downwelling irradiance
EdGND	volts	Dark current values for Ed sensor
Epar	uE/cm^2/s	Profiled Photosynthetic Available Radiation
Es###.#	uW/cm^2/nm	Downwelling irradiance above the surface
EsGND	volts	Dark current values for Es sensor

Eu###.#	uW/cm^2/nm	Upwelling irradiance
EuGND	volts	Dark current values for Eu sensor
F0###.#	uW/cm^2/nm	Extraterrestrial Solar irradiance
Kd###.#	1/m	Diffuse attenuation coefficient for downwelling irradiance
Kl###.#	1/m	Diffuse attenuation coefficient for upwelling radiance
Knf###.#	1/m	Diffuse attenuation coefficient for natural fluorescence of chl a
Kpar	1/m	Diffuse attenuation coefficient for PAR
Ku###.#	1/m	Diffuse attenuation coefficient for upwelling irradiance
Lsky###.#	uW/cm^2/nm/sr	Sky radiance
Lt###.#	uW/cm^2/nm/sr	Total water radiance
Lu###.#	uW/cm^2/nm/sr	Upwelling radiance
LuGND	volts	Dark current values for Lu sensor
Lw###.#	uW/cm^2/nm/sr	Water leaving radiance
Lwn###.#	uW/cm^2/nm/sr	Normalized water leaving radiance (Nlw=Lw * Fo/Es)
natf	nE/m^2/sr/s	natural fluorescence of chl a
Oz	dobson	Column Ozone
PAR	uE/cm^2/s	Photosynthetic Available Radiation measured at the sea surface
pitch	degrees	Instrument pitch
PP	mgC/mgchla/hr	Primary Productivity
pressure	dbar	Water Pressure
pressure_atm	mbar	Atmospheric pressure
Q###.#	sr	Eu/Lu (equal to Pi in diffuse water)
quality	none	Data quality flag...arbitrary analyst specific value
R###.#	unitless	Irradiance reflectance (Re=Eu/Ed)
RelAz	degrees	Sensor azimuth angle, relative to the solar plane (for above water radiometers)
Rl###.#	1/sr	Radiance reflectance (Rl=Lu/Ed)
roll	degrees	Instrument roll
Rpi###.#	unitless	Radiance reflectance with PI
Rrs###.#	1/sr	Remote sensing reflectance (Rrs=Lw/Ed)
sal	PSU	Salinity
sample	none	Sample Number
SenZ	degrees	Sensor zenith angle (for above water radiometers)
sigmaT	kg/m3	Density - 1000kg/m3
SN	none	Instrument serial number - should be in documents...
SST	degreesC	Sea Surface Temperature
stimf	volts	Stimulated fluorescence of chl a
SZ	m	Secchi disk depth
SZA	degrees	Solar zenith angle (calculable from time/position)
tilt	degrees	Instrument tilt
trans	%	Precent transmission
SPM	g/L	Total Suspended Particulate Material
volfilt	L	Volume Filtered
wavelength	nm	Wavelength of measurement
windspeed	m/s	Wind Speed
Wt	degreesC	Water temperature
Wvp	mm	Water vapor
Pigments		
Allo	mg/m^3	Alloxanthin
Anth	mg/m^3	HPLC Antheraxanthin
Asta	mg/m^3	HPLC Astaxanthin

At	degreesC	Air temperature
beta-beta-Car	mg/m^3	HPLC Beta,beta-Carotene
beta-eta-Car	mg/m^3	HPLC Beta,eta-Carotene
beta-psi-Car	mg/m^3	HPLC Beta,psi-Carotene
But-fuco	mg/m^3	HPLC 19'-Butaonoyloxyfucoxanthin
Cantha	mg/m^3	HPLC Canthaxanthin
CHL	mg/m^3	Fluoresence/spectrophotometric derived chlorophyll a
Chl_a	mg/m^3	HPLC Chlorophyll a
Chl_b	mg/m^3	HPLC Chlorophyll b
Chl_c	mg/m^3	HPLC Chlorophyll c
Chlide_a	mg/m^3	HPLC Chlorophyllide a
Chlide_b	mg/m^3	HPLC Chlorophyllide b
Croco	mg/m^3	HPLC Crocoxanthin
Diadchr	mg/m^3	HPLC Diadinochrome
Diadino	mg/m^3	HPLC Diadinoxanthin
Diato	mg/m^3	HPLC Diatoxanthin
Dino	mg/m^3	HPLC Dinoxanthin
DV_Chl_a	mg/m^3	HPLC Divinyl Chorophyll a
DV_Chl_b	mg/m^3	HPLC Divinyl Chorophyll b
Echin	mg/m^3	HPLC Echinenone
Et-8-carot	mg/m^3	HPLC Ethyl-apo-8'-carotene
Et-chlide_a	mg/m^3	HPLC Ethyl Chlorophyllide a
Et-chlide_b	mg/m^3	HPLC Ethyl Chlorophyllide b
eta-eta-Car	mg/m^3	HPLC Eta-eta-Carotene
Fuco	mg/m^3	HPLC Fucoxanthin
Hex-fuco	mg/m^3	HPLC 19'-Hexanoyloxyfucoxanthin
Lut	mg/m^3	HPLC Lutein
Lyco	mg/m^3	HPLC Lycopene
Me-chlide_a	mg/m^3	HPLC Methyl Chlorophyllide a
Me-chlide_b	mg/m^3	HPLC Methyl Chlorophyllide b
Mg_DVP	mg/m^3	HPLC Mg 2,4 divinyl pheoporphyrin a5 monomethyl ester
Monado	mg/m^3	HPLC Monadoxanthin
Neo	mg/m^3	HPLC Neoxanthin
P-457	mg/m^3	HPLC P-457
Perid	mg/m^3	HPLC Peridinin
PHAEO	mg/m^3	Pheaopigment
Phide_a	mg/m^3	HPLC Pheophorbide a
Phide_b	mg/m^3	HPLC Pheophorbide b
Phide_c	mg/m^3	HPLC Pheophorbide c
Phythl-chl_c	mg/m^3	HPLC Phytylated Chlorophyll c
Phytin_a	mg/m^3	HPLC Pheophytin a
Phytin_b	mg/m^3	HPLC Pheophytin b
Phytin_c	mg/m^3	HPLC Pheophytin c
Pras	mg/m^3	HPLC Prasinoxanthin
Pyrophytin_a	mg/m^3	HPLC Pyropheophytin a
Pyrophytin_b	mg/m^3	HPLC Pyropheophytin b
Pyrophytin_c	mg/m^3	HPLC Pyropheophytin c
Siphn	mg/m^3	HPLC Siphonein
Siphx	mg/m^3	HPLC Siphonaxanthin
Tpg	mg/m^3	Total (sum of all) pigments
Vauch	mg/m^3	HPLC Vaucheriaxanthin-ester
Viola	mg/m^3	HPLC Violaxanthin

Zea	mg/m^3	HPLC Zeaxanthin
Time, Location		
date	yyyymmdd	Sample date
day	dd	Sample Day
hour	hh	Sample Hour
jd	jjj	Sample Julian Day (Day of Year)
lat	degrees	Sample Latitude
lon	degrees	Sample Longitude
minute	mn	Sample Minute
month	mo	Sample Month
second	ss	Sample Second
station	none	Sample Station
time	hh:mm:ss	Sample time
year	yyyy	Sample Year

GLOSSARY

A/D	Analog-to-Digital
ALSCAT	ALPHA and Scattering Meter (Note: the symbol α corresponds to $c(\lambda)$, the beam attenuation coefficient, in present usage.)
AERONET	Aerosol Robotic Network
AOL	Airborne Oceanographic Lidar
AOT	Aerosol Optical Thickness
ARGOS	Not an acronym: the name given to the data collection and location system on NOAA Operational Satellites
ASCII	American Standard Code for Information Inter- change
AMT	Atlantic Meridional Transect
AMT-3	The Third AMT Cruise
AMT-5	The Fifth AMT Cruise
AMT-6	The Sixth AMT Cruise
AMT-7	The Seventh AMT Cruise
BSI	Biospherical Instruments, Inc.
CCD	Charge Coupled Device
CERT	Calibration Evaluation and Radiometric Testing
CSH	UNIX "C-shell" script programming utility
DAS	Data Acquisition Sequence
DU	Dobson Unit of total ozone
DUT	Device Under Test
DVM	Digital Voltmeter
FEL	Not an acronym; a type of standard lamp for irradiance and radiance calibration
FOV	Field-of-View
FWHM	Full-Width at Half-Maximum
GAC	Global Area Coverage
GASM	General Angle Scattering Meter
GMT	Greenwich Mean Time
GOES	Geostationary Operational Environmental Satellite
GPIB	General Purpose Interface Bus
GPS	Global Positioning System
GSFC	Goddard Space Flight Center
HDF	Hierarchical Data Format
HRPT	High Resolution Picture Transmission
IFOV	Instantaneous field-of-view
IOP	Inherent Optical Properties
IR	Infrared
L1A	Level-1A SeaWiFS data product with navigation information
LAC	Local Area Coverage
MERIS	Marine Environment Research Imaging Spectroradiometer (French)
MPL	Micropulse Lidar
MOBY	Marine Optical Buoy
MODIS	Moderate Resolution Imaging Spectroradiometer
MOS	Moderate Resolution Imaging Spectrometer

NASA	National Aeronautics and Space Administration
NIST	National Institute of Standards and Technology
NOAA	National Oceanic and Atmospheric Administration
OCTS	Ocean Color and Temperature Sensor (Japanese)
PI	Principal Investigator
POLDER	Polarization and Directionality of the Earth Reflectance (French)
QC	Quality Control
SeaBAM	SeaWiFS Bio-optical Algorithm Mini-workshop
SeaBASS	SeaWiFS Bio-optical Archive and Storage System
SeaWiFS	Sea-viewing Wide Field-of-view Sensor
SIMBIOS	Sensor Intercomparison and Merger for Biological and Interdisciplinary Oceanic Studies
SIRREX	SeaWiFS Intercalibration Round-Robin Experiment
SIRREX-7	The Seventh SIRREX
SNR	Signal-to-Noise Ratio
UPS	Un-interruptable Power Supply
UV	Ultraviolet
UVB	Ultraviolet-B

REPORT DOCUMENTATION PAGE

Form Approved
OMB No. 0704-0188

1. AGENCY USE ONLY *(Leave blank)*	2. REPORT DATE	3. REPORT TYPE AND DATES COVERED
	March 2001	Technical Memorandum

4. TITLE AND SUBTITLE
In Situ Aerosol Optical Thickness Collected by the SIMBIOS Program (1997–2000): Protocols, and Data QC and Analysis

5. FUNDING NUMBERS
970

6. AUTHOR(S)
Giulietta S. Fargion, Robert Barnes, and Charles McClain

7. PERFORMING ORGANIZATION NAME(S) AND ADDRESS (ES)
Goddard Space Flight Center
Greenbelt, Maryland 20771

8. PEFORMING ORGANIZATION REPORT NUMBER
2001-01672-0

9. SPONSORING / MONITORING AGENCY NAME(S) AND ADDRESS (ES)
National Aeronautics and Space Administration
Washington, DC 20546-0001

10. SPONSORING / MONITORING AGENCY REPORT NUMBER
TM—2001–209982

11. SUPPLEMENTARY NOTES
G. Fargion and R. Barnes: SAIC General Sciences Corp., Beltsville, Maryland

12a. DISTRIBUTION / AVAILABILITY STATEMENT
Unclassified–Unlimited
Subject Category: 48
Report available from the NASA Center for AeroSpace Information,
7121 Standard Drive, Hanover, MD 21076-1320. (301) 621-0390.

12b. DISTRIBUTION CODE

13. ABSTRACT *(Maximum 200 words)*

The purpose of this technical report is to provide current documentation of the Sensor Intercomparison and Merger for Biological and Interdisciplinary Oceanic Studies (SIMBIOS) Project Office activities on *in situ* aerosol optical thickness (i.e., protocols, and data QC and analysis). This documentation is necessary to ensure that critical information is related to the scientific community and NASA management. This critical information includes the technical difficulties and challenges of validating and combining ocean color data from an array of independent satellite systems to form consistent and accurate global bio-optical time series products. This technical report is not meant as a substitute for scientific literature. Instead, it will provide a ready and responsive vehicle for the multitude of technical reports issued by an operational project.

14. SUBJECT TERMS
SIMBIOS, aerosol optical thickness, ocean color data.

15. NUMBER OF PAGES
103

16. PRICE CODE

17. SECURITY CLASSIFICATION OF REPORT	18. SECURITY CLASSIFICATION OF THIS PAGE	19. SECURITY CLASSIFICATION OF ABSTRACT	20. LIMITATION OF ABSTRACT
Unclassified	Unclassified	Unclassified	UL